# The Gamma Deposition Matrix Method for Coupled Neutron-gamma Reactor Heating Calculations

by

Xinyan Wang

A dissertation submitted in partial fulfillment
of the requirements for the degree of
Doctor of Philosophy
(Nuclear Engineering and Radiological Sciences)
in the University of Michigan
2021

Doctoral Committee:

Professor Thomas J. Downar, Co-Chair
Professor William R. Martin, Co-Chair
Professor Robert Krasny
Dr. Yuxuan Liu
Dr. Shane Stimpson, BWX Technologies, Inc.

Xinyan Wang
wxinyan@umich.edu
ORCID iD: 0000-0001-9129-1023

# Acknowledgements

First, I want to thank my advisor Prof. William Martin. It is my honor to work with him starting 7 years ago when I was still an undergraduate student in the physics department. His sageness, kindness, insightful guidance and endless patience inspired me in all the time of research and writing of this thesis. Besides my advisor, I would like to thank the rest of my thesis committee: Prof. Thomas Downar, Prof. Robert Krasny, Dr. Shane Stimpson and especially Dr. Yuxuan Liu for their perceptive comments and encouragement. I couldn't have reached this far without their help.

I must also acknowledge the CASL program not only for its support of this work but also for bringing me to this community with many exceptional colleagues. I feel I am indebted to my internship mentors, Dr. Ben Collins and Dr. Shane Stimpson, in Oak Ridge National Laboratory for their precious support both during and after the internships until today.

I also would like to thank Prof. Brian Kiedrowski for his timely and accurate answers to my research problems for many times. I still remember once I was struggling with an inconsistent modeling result for almost 2 months until he pointed out what was going wrong.

I want to save the last paragraph to show my gratitude to my family. My parents, always supporting me both emotionally and financially while I am pursuing my academic goals from 6000 miles away. My uncle and aunt in California, taking care of me and nagging me when my parents are in GMT +8 time zone. Thank you for all the loves!

# Table of Contents

# List of Tables

# List of Figures

# Abstract

This thesis concerns the development of an approximate model to predict the energy deposited by gammas following a gamma-release reaction in a light water reactor. This approximate model is an alternative method to the conventional approach of solving the gamma transport equation. Although explicitly solving the gamma transport equation has become possible in recent years thanks to advancements in computing power, it is desirable to come up with a simpler method given the fact that gammas only account for ~10% of energy deposition in LWRs. The new method, called the gamma deposition matrix (GDM) method, calculates gamma energy deposition for coupled $(n,\gamma)$ iterations without performing an explicit gamma transport calculation. Entries of the GDM represent the gamma energy deposited in a given spatial cell due to a gamma source in another (or the same) spatial cell. The GDM can be pre-calculated based on a gamma deposition Green's function, which allows gamma energy deposition to be directly computed from the known gamma source by using the GDM to perform a simple matrix-vector multiplication. A significant advantage of the GDM method is that since gammas mainly interact with electrons, gamma cross sections are independent of temperature and depletion. As a result, the GDM is insensitive to thermal feedback and isotopic changes due to depletion, allowing the initial GDM to be used for all $(n,\gamma)$ iterations throughout a reactor cycle.

Through coupled $(n,\gamma)$ calculations in MPACT, it is shown that the gamma source spectra do not change over coupled $(n,\gamma)$ iterations in an LWR. This observation, combined with the fact that the gamma energy deposition is integrated over all gamma energies, leads to the conclusion that the GDM is not a function of gamma energy, resulting in a substantial reduction in the size of the GDM. However, in principle the spatial dependence of the GDM can be prohibitive because the GDM is non-zero for any combination of source and target cells, leading to a huge GDM for full core calculations. In order to further reduce the size of the GDM, the spatial range of the GDM is reduced by neglecting the energy

deposition outside a given distance from the source cell. This active region is called a subdomain and the GDM entries are only non-zero for those cells in the subdomain surrounding the source cell. This subdomain model reduces the size of the GDM substantially, with a corresponding reduction in GDM computation time and memory. Since gammas that escape from the subdomain without interaction will result in a loss of energy, an energy preservation scheme is developed that ensures conservation of gamma energy. Numerical results calculated using the energy-independent GDM with the subdomain approximation agree well with reference Monte Carlo calculations. The subdomain approximation is proved to be especially beneficial for large cases. For a small modular reactor whole core case with 37 assemblies and 289 pins within each assembly, using the subdomain approximation along with the energy preservation correction reduces the size of the matrix by ~20 while maintaining satisfactory accuracy.

# Chapter 1
# Introduction

Energy deposition in nuclear reactors involve various forms including charged particles, neutron slowing down and capture, and gamma interactions. According to ANSI/ANS-19.3.4 [1], charged particles include fission products, recoil nuclei, alpha and beta particles, protons, electrons and positrons, and they account for the majority of thermal energy in reactors. As these charged particles slow down, they lose energy to the surrounding medium and thereby deposit energy. To calculate this form of energy deposition, the first step is to determine the rates, spatial distribution, magnitude and energy of the charged particles that are produced. Strictly, the next step would be to perform transport calculations for these particles to obtain the magnitude and spatial distribution of energy deposition from the slowing down process. However, charged particles have very short mean free paths in the fuel. Heavy charged fission fragments and alpha particles, for example, have a range on the order of $10^{-3}$ cm in ceramic and heavy metal fuels. Therefore, it is reasonable to assume that energy carried by these particles is deposited locally. Another simplification can be applied to heavy charged particles is that, as the kinetic energy of these fission-produced charged particles is generally independent of the incident neutron energy, only the average kinetic energy of heavy charged particles is needed. As a result, energy deposition by heavy charged particles and alpha particles can be obtained from fission production rates and average kinetic energy of the particles directly. As for beta particles, although typical beta particle ranges are orders of magnitude longer than fission fragment ranges, one can still generally assume deposition of beta particle energy at its point of origin.

The neutron calculation is more complicated mainly because the neutral charge particle has much longer range compared to charged particles. The neutron slowing down process

deposits energy in matter in the form of elastic and inelastic collisions with target nuclei. In these reactions the energy transferred depends on the incident neutron energy as well as the nucleus mass and properties, which means, unlike heavy charged particles, neutron slowing down energy deposition is spectrum dependent and an explicit scheme is required to compute the incoming and outgoing energy of the reactions. The outgoing energy is carried away by outgoing neutrons in elastic collisions and by both outgoing neutrons and outgoing photons in inelastic collisions. As for neutron capture reactions followed by photon emissions, all or some of the outgoing energy is carried away by the emitted photon. For example, $^{10}$B's neutron capture reaction releases a $^{7}$Li, an alpha particle and a photon. Historically, neutron heat deposition is usually approximated to be local because energy transferred by neutron slowing down is only a small part of the total fission energy release, but a transport calculation is necessary to predict a more accurate spatial distribution.

## 1.1. Gamma Energy Release and Deposition in LWRs

Neutron has always been the essential part of nuclear reactor analysis. On the one hand, fission reactions are directly induced by thermal neutrons. On the other hand, as shown in Table 1-1, more than 85% of energy released from U-235 and U-238 is directly related to neutron and induced fission fragments. For ease of calculation, the gamma heating distribution is usually assumed to be the same as gamma release. In other words, gamma energy is assumed to be deposited where it is released and is usually calculated by scaling the fission rates and neutron capture rates.

Table 1-1 Fission energy released from the section of MF1/MT458 in ENDF/B-VII.1

| Energy Mode | | Fraction | U-235 (MeV) | U-238 (MeV) | Range | Time |
|---|---|---|---|---|---|---|
| **Fission Fragment** | | 80% | 169.13 | 169.80 | Local | Instant |
| **Beta decay of FPs** | | 3-4% | 6.50 | 8.48 | Local | Delayed |
| **Fission Gammas** | Prompt | 3-4% | 6.60 | 6.68 | **Global** | Instant |
| | Delayed | 3-4% | 6.33 | 6.68 | | Delayed |
| **Anti-neutrinos** | | 4-5% | 8.75 | 8.25 | Unrecoverable | Delayed |
| **Neutron Capture** | | 3-5% | 6.0-11.0 | | **Global** | Instant/Delayed |
| **Neutron Scattering** | | 2-3% | 4.0-5.0 | | Global | Instant |

However, recently, with the improvements of computational powers as well as the growing needs to analyze advanced reactors, explicitly modeling gamma transport has attracted more attention than ever. Not only because gammas count for a non-trivial 10% of the total energy release, but also because gamma energy is globally deposited and its mean free path is longer than that of thermal neutrons. Longer mean free paths can lead to more uniform energy deposition distribution and reduce power peaking. Quantitatively, the mean free path (MFP) is calculated as

$$\lambda = \frac{1}{\Sigma_{tr}} = \frac{\sum_{g=1}^{G} \phi_g}{\sum_{g=1}^{G} \Sigma_{tr,g} \phi_g} \quad (1.1)$$

in MPACT with HELIOS library using a pin cell problem as shown in Figure 1-1:

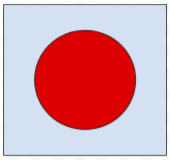

- Pin pinch: 1.26cm
- Fuel: 0.4096cm, 3.1%, 293K
- Moderator: 1.0 g/cc, 293K, 1300pcm

Figure 1-1 Pin Cell Configuration

And the results are presented in Table 1-2. As one can see, the mean free path of gammas is on par with that of fast neutrons and much longer than that of thermal neutrons, which means that gamma deposition is potentially smoother than neutron deposition (and thus fission rates).

Table 1-2 Mean Free Path(cm)

| | 3.1% Fuel | Mod | Averaged MFP |
|---|---|---|---|
| **Neutron** | 2.355 | 1.500 | 1.71 |
| **Neutron(<0.625eV)** | 1.400 | 0.480 | 0.614 |
| **Neutron(>0.625eV)** | 2.70 | 2.89 | 2.83 |
| **Gamma** | 0.8439 | 19.88 | 2.34 |

Further verification is done through MCNP6 modeling. CASL benchmark progression problem 2h [2] is chosen for this verification. The problem is a 17x17 2D assembly with $B_4C$ control rods. The temperature is at 600K, the boron level is 1300 pcm and the fuel concentration is 3.1%. The cross section library used for this calculation is ENDF.VII.1. The results are shown in Figure 1-2. The top entry in each pin cell is the normalized fission

rate and the bottom one is the normalized gamma heat deposition. In most of the pins, gamma heat values are closer to 1 than fission rates, which confirms that gamma deposition is smoother. Such differences in heating distribution pattern can lead to different pin power results compared to fission rates-based pin power calculations and thus affect thermal-hydraulic feedback calculations as well as pin power peaking.

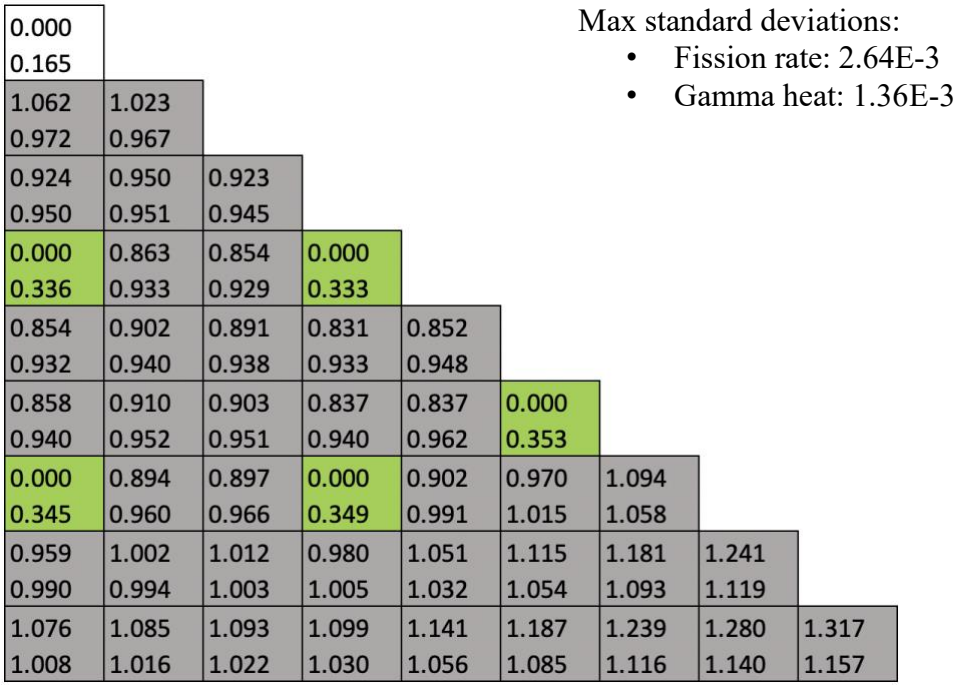


Figure 1-2 Fission Rate and Gamma Heat Distribution of CASL Problem 2h [3]

## 1.2. Current Gamma Heating Methods

Conventionally, given the limitation of computational power and the fact that energy deposition in the form of gamma rays is only about 10% of the total energy deposition in LWRs, gamma heating is usually calculated by approximate methods. The simplest scheme assumes that energy carried by gamma is deposited at the fission site. This is a widely accepted assumption due to its straightforwardness and reasonable accuracy. The default energy deposition model in the CASL (Consortium for Advanced Simulation of Light Water Reactors) 3D hi-fidelity deterministic transport code MPACT [4], for example, deposits all fission energy locally in the fuel rods, including gamma energy. However, this

approximation fails to account for the gamma long mean free path which can yield a smoother distribution pattern compared to depositing the gamma energy locally. To take the global transport nature of gammas into account while still avoiding the costs of gamma transport calculations, some code systems are implemented with simplified gamma smearing models. For example, lattice transport codes such as CASMO-3, developed by Studsvik Scandpower, Inc. (SSP), and Kernel Analyzer by Ray-tracing Method for fuel Assembly (KARMA [5]), a deterministic multigroup code developed by Korea Atomic Energy and Research Institute (KAERI) for pressurized water reactor fuel assembly calculations as well as cross section data generations, a constant gamma smearing factor was used to obtain more realistic pin power distribution by assuming that the gamma energy deposition for each fuel pin was a predetermined constant [6]. Recently, an improved gamma smearing model was developed and implemented into MPACT to better account for the global deposition of gamma energy. The new model redistributes gamma energy deposition in a predefined block of NxN pins centered at the pin where gamma is released [7]. Within the block, gamma deposition is determined by the number of electrons in the target pins.

In the past decade, more and more code systems are implemented with explicit gamma transport capabilities. For instance, in additional to the flat fractional gamma power mode, the KARMA code has two more options available for gamma heat deposition calculation since version 1.2 [8]: (1) through a direct method of characteristics (MOC) transport calculation, (2) through a coarse mesh finite difference (CMFD) diffusion calculation with homogenized pin cells. Besides KARMA, CASMO5 is another lattice physics code for radiation transport calculation and cross section data generation. CASMO5 is able to do CMFD-accelerated MOC calculations for single fuel assembly or multi-assembly problems. After the neutron transport calculation is finished, gamma sources induced by the neutron flux can be calculated for all regions and 18 gamma energy groups, and a characteristics-based gamma transport calculation can be performed for gamma flux and power [9]. The code nTRACER [10], a whole core neutronics code developed at Seoul National University, is capable of doing 3D whole core hi-fidelity radiation transport calculations with the 2D/1D method, where the 2D radial MOC solver and the 1D axial solver based on MOC

or simplified P3 source expansion nodal method ($SP_3$ SENM) are coupled through transverse leakage and accelerated by 3D CMFD [11]. The explicit gamma calculation feature employs MOC as the high-order transport solver and it is accelerated by fixed source CMFD. Currently, the gamma transport solver is one-way coupled with the neutronics solver. The gamma solver starts fixed source iterations after neutron iterations are finished. The fully converged neutron flux serves as source term for the gamma iterations. The PROTEUS code, developed by ANL, is another 3D hi-fidelity full core deterministic code with explicit gamma transport capability available. Unlike nTRACER, PROTEUS's 3D capability is fulfilled by coupling the 2D radial MOC solver with the discontinuous Galerkin finite element method for the axial direction [12]. Gamma transport capability is implemented by SN and MOC transport solvers. Heating by both neutrons and gammas is calculated after the gamma fixed source run for further multiphysics calculations [13].

There are also Monte Carlo codes with gamma transport capabilities. For example, the Serpent code developed at VTT Technical Research Centre of Finland, Ltd in 2004. Coupled neutron-photon transport was recently implemented into Serpent 2 [14] and energy deposition treatment [15] was developed based on the neutron-photon transport routine. As introduced by [14], Serpent calculates photon emissions through neutron-photon coupled calculation mode, writes them in a file as source points, and then performs a gamma transport calculation. The gamma energy deposition makes use of the Kinetic Energy Release in Material (KERMA) coefficient [15]. In addition to Serpent, MCNP has been able to do coupled neutron-gamma calculations since a very early time [16]. MCNP is a general-purpose, continuous-energy general-geometry Monte Carlo N-Particle code developed by Los Alamos National Laboratory (LANL) [17]. It is capable of doing transport calculations for many particle types and has numerous flexible tallies including gamma volume flux, fission energy and heat deposition. In this research project, MCNP is used for the method to account for global gamma deposition as well as generating reference results for the test problems.

## 1.3. Motivation

As mentioned in Section 1.1, it is important to do gamma energy deposition calculations for reactor analysis. Solving gamma transport explicitly can be computationally expensive. For instance, with group-by-group sweeping in multigroup deterministic codes, the time for one gamma group sweep is on par with one neutron group sweep assuming the same mesh is used. The overall effect on performance to do a gamma transport calculation is not severe, since the number of gamma groups is usually fewer than the number of neutron groups. However, given that gamma energy counts for only 10% of the total energy release, it is natural to come up with a method to calculate the heat deposition in a simpler way than solving the gamma transport equation explicitly. As a result, the heat deposition distribution will instead be calculated using a Green's function approach to compute a gamma deposition response matrix that is then used to compute the overall deposition with matrix-vector multiplication, where the vector is the spatial distribution of the $(n, \gamma)$ source from the neutronic calculation. Since gammas interact with electrons rather than the nuclei, gamma microscopic cross sections tend to be independent of temperature. This will be discussed in Section 2.3 in detail. This fact allows the pre-calculation of the gamma deposition matrix (GDM), instead of calculating them on the flight repeatedly in each gamma iteration. By doing this, the expensive gamma sweeping step can be replaced by a much simpler matrix-vector multiplication.

## 1.4. Dissertation Layout

The rest of this thesis starts with a description of the gamma transport equation as well as how an explicit gamma transport capability and gamma heat deposition calculation scheme are implemented in MPACT in Chapter 2. Also, some important gamma physics that helps to optimize the GDM method performance is introduced and verified. The fundamentals of the GDM method and how the matrix is generated are explained in Chapter 3. Chapter 4 discussed how the GDM is reduced by eliminating the energy dependence and approximations which allow this reduction. Chapter 5 discusses how the size of the GDM is further reduced in the spatial variable. Approximations include (1) ignoring the energy

deposition for target cells that are distant from the source cell, as these cells have low values of energy deposition, and (2) averaging energy deposition over cells that are not close to the source, but still have a non-trivia, or middle value, of energy deposition. However, when the low value entries are ignored, conservation of energy is violated, and energy preservation correction strategies are developed to address this issue. The purposes of these simplifications discussed in Chapter 4 and Chapter 5 are to reduce the matrix generation time, matrix multiplication time and memory to store the matrix. In Chapter 6, numerical results with GDM using these different approximations will be presented. In addition, some results using MPACT's explicit gamma transport solver will be presented. Finally, Chapter 7 presents the summary, conclusions and recommendations for future work.

# Chapter 2

# Gamma Transport

## 2.1. Gamma Transport Equation

The Boltzmann gamma transport equation describes interactions of photons including leakage, collision, scattering and production. If production and scattering are assumed to be isotropic, the gamma transport equation becomes equation ( 2.1 ) as shown below:

$$\begin{aligned} \Omega \cdot \nabla\psi^{\gamma}(\boldsymbol{r},\boldsymbol{\Omega},E^{\gamma}) + \Sigma_t^{\gamma}(\boldsymbol{r},E^{\gamma})\psi^{\gamma}(\boldsymbol{r},\boldsymbol{\Omega},E^{\gamma}) &= Q^{scat}(\boldsymbol{r},\boldsymbol{\Omega},E^{\gamma}) + Q^{n\gamma}(\boldsymbol{r},E^{\gamma}) \\ Q^{scat}(\boldsymbol{r},\boldsymbol{\Omega},E^{\gamma}) &= \int_{4\pi}\int_0^{\infty} \Sigma_s^{\gamma}(\boldsymbol{r},\boldsymbol{\Omega}'\cdot\boldsymbol{\Omega},E^{\gamma\prime}\rightarrow E^{\gamma})\psi^{\gamma}(\boldsymbol{r},\boldsymbol{\Omega}',E^{\gamma\prime})dE^{\gamma\prime}\,d\Omega' \\ Q^{n\gamma}(\boldsymbol{r},E^{\gamma}) &= \frac{1}{4\pi}\int_0^{\infty} \Sigma_{n\gamma}(\boldsymbol{r},E^{n}\rightarrow E^{\gamma})\phi^{n}(\boldsymbol{r},E^{n})dE^{n} \end{aligned} \qquad (2.1)$$

this equation is solved numerically for the gamma angular flux $\psi^{\gamma}(\boldsymbol{r},\boldsymbol{\Omega},E^{\gamma})$ as well as the scalar flux $\phi^{\gamma}(\boldsymbol{r},E^{\gamma})$ at position $\boldsymbol{r}$, angle $\boldsymbol{\Omega}$ and gamma energy $E^{\gamma}$ .

Just like the neutron transport equation [18], the first term of the gamma transport equation describes the rate at which gammas are traveling in $d\Omega$ about $\boldsymbol{\Omega}$, $dE^{\gamma}$ about $E^{\gamma}$ and dr about $\boldsymbol{r}$:

$$\Omega \cdot \nabla\psi^{\gamma}(\boldsymbol{r},\boldsymbol{\Omega},E^{\gamma})drd\Omega dE^{\gamma}$$

The second term describes the gamma collision rate with the system in $drd\Omega dE^{\gamma}$ about $(\boldsymbol{r},\boldsymbol{\Omega},E^{\gamma})$ where $\Sigma_t^{\gamma}(\boldsymbol{r},E^{\gamma})$ is the total cross section. Note that for isotropic scattering, $\Sigma_{tr}^{\gamma}(\boldsymbol{r},E^{\gamma})$ is equal to total cross section $\Sigma_t^{\gamma}(\boldsymbol{r},E^{\gamma})$:

$$\Sigma_t^{\gamma}(\boldsymbol{r},E^{\gamma})\psi^{\gamma}(\boldsymbol{r},\boldsymbol{\Omega},E^{\gamma})drd\Omega dE^{\gamma}$$

The scattering source term $Q^{scat}(\boldsymbol{r}, \boldsymbol{\Omega}, E^{\gamma})$ describes gamma scattering process. $\Sigma_s^{\gamma}(\boldsymbol{r}, \boldsymbol{\Omega}' \cdot \boldsymbol{\Omega}, E^{\gamma\prime} \rightarrow E^{\gamma})$ is the gamma scattering cross section from $(\boldsymbol{\Omega}', E^{\gamma\prime})$ to $(\boldsymbol{\Omega}, E^{\gamma})$. The whole term describes the rate gamma scattered into $dE^{\gamma}$ about $E^{\gamma}$ and $d\Omega$ about $\boldsymbol{\Omega}$ at $\boldsymbol{r}$.

The source term is different than for the neutron transport equation. In the gamma transport equation, the source term $Q^{n\gamma}(\boldsymbol{r}, E^{\gamma})$ describes the source of gammas due to neutron capture, the $(n, \gamma)$ source. $\phi^{n}(\boldsymbol{r}, E^{n})$ is the neutron flux at location $\boldsymbol{r}$ and neutron energy $E^{n}$ and $\Sigma_{n\gamma}(\boldsymbol{r}, E^{n} \rightarrow E^{\gamma})$ is the effective $(n, \gamma)$ cross section. Just like the gamma scattering source, the $(n, \gamma)$ source is assumed to be isotropic. $\Sigma_{n\gamma}(\boldsymbol{r}, E^{n} \rightarrow E^{\gamma})$ accounts for the production of prompt gammas, delayed gammas and capture gammas.

## 2.2. Implementation of Gamma Transport Capability in MPACT

Gamma transport capability was necessary because we intended to implement the GDM method into MPACT, and transport calculation is required for the matrix generation step of the GDM method, which will be discussed in Section 3.3. Therefore, the thesis work started with implementing an explicit gamma transport solver in MPACT. We have successfully done the implementation of gamma transport capability by leveraging existing procedures in MPACT including the 2D MOC solver and the 2D/1D solver as well as developing new procedures like n-gamma source calculation scheme and gamma heating procedure, which will all be covered in this section with more details. The results were published in M&C 2019 [19] and PHYSOR 2020 [20]. Also, the results by MPACT with gamma transport could serve as references for results by MPACT with GDM method verification.

As introduced in Section 1.2, MPACT is a deterministic transport code that solves the multigroup transport equation. The multigroup form of gamma transport equation is shown in equation ( 2.2 ):

$$\boldsymbol{\Omega}\cdot\nabla\psi_g^{\gamma}(\boldsymbol{r},\boldsymbol{\Omega})+\Sigma_{tr,g}^{\gamma}(\boldsymbol{r})\psi_g^{\gamma}(\boldsymbol{r},\boldsymbol{\Omega})=Q_g(\boldsymbol{r})$$
$$Q_g(\boldsymbol{r})=Q_g^{scat}(\boldsymbol{r})+Q_g^{n\gamma}(\boldsymbol{r})$$
$$Q_g^{scat}(\boldsymbol{r})=\frac{1}{4\pi}\sum_{g'}^{G}\Sigma_{s,g'\to g}^{\gamma}(\boldsymbol{r})\phi_{g'}^{\gamma}(\boldsymbol{r}) \qquad (2.2)$$
$$Q_{gg}^{n\gamma}(\boldsymbol{r})=\frac{1}{4\pi}\sum_{h}^{H}\Sigma_{n\gamma,h\to g}(\boldsymbol{r})\phi_h^{n}(\boldsymbol{r})$$

where $\psi_g^{\gamma}(\boldsymbol{r},\boldsymbol{\Omega})$ is the angular flux in gamma energy group $g$ and $\phi_h^n(\boldsymbol{r})$ is neutron scalar flux in neutron energy group $h$. $\Sigma_{tr,g}^{\gamma}(\boldsymbol{r})$ is the multigroup gamma transport macroscopic cross section in group $g$, $\Sigma_{s,g'\to g}^{\gamma}(\boldsymbol{r})$ is the multigroup gamma macroscopic scattering cross section from group $g'$ to $g$ and $\Sigma_{n\gamma,h\to g}(\boldsymbol{r})$ is the multigroup $(n,\gamma)$ cross section which describes gamma production in group $g$ induced by incident neutrons in group $h$.

The coupled neutron-gamma iteration scheme in MPACT is shown in Figure 2-1. In each iteration, the neutron transport equation is first solved for $\phi_h^n(\boldsymbol{r})$. Then the gamma source $Q_g^{n\gamma}(\boldsymbol{r})$ is calculated by $(n,\gamma)$ reaction using $\phi_h^n(\boldsymbol{r})$. Next, with source $Q_g^{n\gamma}(\boldsymbol{r})$, the gamma transport equation is solved as a fixed source problem for the gamma flux $\phi_g^{\gamma}(\boldsymbol{r})$. Finally, heat deposition arising from the gamma flux and neutron flux distributions will be calculated. These four steps are iterated until convergence is reached.

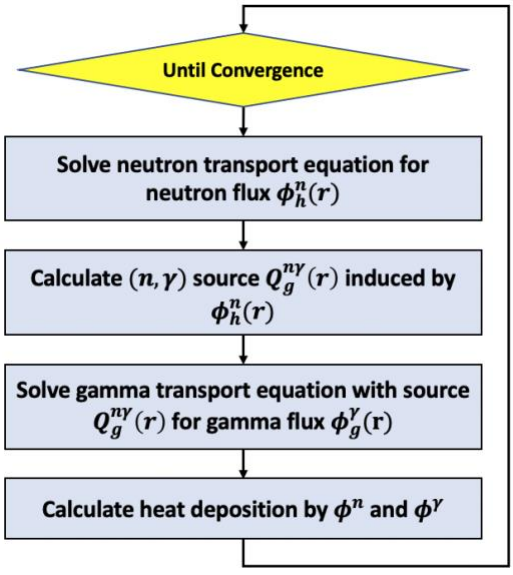


Figure 2-1 Coupled Neutron Gamma Iteration Scheme

The architecture in Figure 2-1 indicates that the number of gamma sweeps is the same as the number of neutron sweeps. Therefore, the gamma flux converges along with the neutron flux, since the gamma source is induced by the neutron flux.

### 2.2.1. Cross Section Library

The ENDF.VI based HELIOS cross section library [21] obtained from the University of Michigan is used for the development of the explicit gamma transport capability in MPACT. The library has 47 neutron groups and 18 gamma groups. The $(n,\gamma)$ data includes the production of prompt, delayed and capture gammas to form a single neutron group to gamma group matrix (47 by 18) per isotope per temperature point. For resonance isotopes in resonance groups and burnable absorbers in all groups, the $(n,\gamma)$ cross sections are given as the ratio of $(n,\gamma)$ cross section to neutron absorption cross section as shown in equation ( 2.3 ):

$$p_{h\to g} = \frac{\sigma_{n\gamma,h\to g}}{\sigma_{a,h}} \qquad (2.3)$$

$(n,\gamma)$ cross section data is given in this form because the absorption cross section $\sigma_{a,h}$ of resonance isotopes and burnable absorbers should be self-shielded by the specific problem. HELIOS assumes that the ratio $p_{h\to g}$ remains constant for the same isotope and temperature, and thus the specific $\sigma_{n\gamma,h\to g}$ should be calculated after self-shielding calculations.

The gamma scattering cross section $\sigma^{\gamma}_{s,g'\to g}$ data in HELIOS consists of a group-to-group matrix 18 by 18 for each isotope. The matrix is formed by combining transport-corrected Compton scattering cross section $\sigma_{c,g'\to g}$ with pair production data $\sigma_{pp,g'}\delta(g,gPair)$. The pair production data has the incident gamma energy bin as the incoming group, and the pair-production energy bin, which is the energy group contains 0.511MeV, as the outgoing group. The pair production data is combined with the Compton scattering data as equation ( 2.4 ):

$$\sigma_{s,g'\to g}^{\gamma} = \sigma_{c,g'\to g} + 2\sigma_{pp,g'}\delta(g, gPair) \quad (2.4)$$

where *c* is Compton, *pp* is pair production, and *gPair* represents the energy group containing pair production induced photon.

The total cross section is defined as equation ( 2.5 ):

$$\begin{aligned}\sigma_{t,g}^{\gamma} &= \sigma_{pe,g} + \sigma_{pp,g} + \sigma_{c,g} = \sigma_{pe,g} - \sigma_{pp,g} + 2\sigma_{pp,g} + \sigma_{c,g} \\ &= \sigma_{pe,g} - \sigma_{pp,g} + 2\sigma_{pp,g}\sum_{g'}^{G}\delta(g', gPair) + \sum_{g'}^{G}\sigma_{c,g\to g'} \\ &= \sigma_{pe,g} - \sigma_{pp,g} + \sum_{g'}^{G}(2\sigma_{pp,g}\delta(g', gPair) + \sigma_{c,g\to g'}) \\ &= \sigma_{pe,g} - \sigma_{pp,g} + \sum_{g'}^{G}\sigma_{s,g\to g'}\end{aligned} \quad (2.5)$$

where "*pe*" stands for photoelectric absorption. It should be emphasized that all the gamma interaction cross sections are temperature-independent.

### 2.2.2. Transport Equation Solvers in MPACT

The first step for gamma transport calculation is to obtain the gamma source in equation ( 2.2 ) after the neutron sweep, shown by the second block of the iteration in ( 2.1 ). Since $(n,\gamma)$ reactions are the primary gamma sources just as fission sources are for neutrons, a new procedure was developed to calculate the neutron-induced gamma source in MPACT [19]. The procedure consists of a matrix-vector multiplication routine, in which the $(n,\gamma)$ cross section data $\sigma_{n\gamma,h\to g}$ mentioned in Section 2.2.1 is the matrix and the groupwise neutron flux is the vector, and the multiplication yields groupwise n-gamma source.

Then with the newly calculated $(n,\gamma)$ source, equation ( 2.2 ) can be solved as a fixed source problem in which the $(n,\gamma)$ source is the source term. The fixed source gamma transport equation is very similar to a fixed source neutron transport equation, as both of these equations have leakage, reaction rate, multigroup scattering and fixed source terms.

Given these similarities, it is possible to solve the gamma transport equation by leveraging the existing transport solvers originally developed for neutron calculations in MPACT. For 2D problems, the 2D method of characteristics (MOC) neutron solvers [22] were leveraged to do 2D gamma transport calculations [19]. Major tasks of the development work included the implementation and utilization of gamma cross section data and generating the $(n,\gamma)$ source for the gamma transport equation.

For 3D problems, the default neutron 3D solver in MPACT is the 2D/1D solver, which is presented in detail by Collins et al [23]. Similar to modifying the 2D MOC solver, the 2D/1D solver originally developed for neutron calculations was leveraged to perform 3D gamma calculations in MPACT [20] because the gamma transport equation is similar to the neutron transport equation. The 2D/1D method decomposes 3D problems into 2D planes in which the transport equation is solved, and the planes are coupled together through a leakage source, and the axial variation in the flux is modeled using a lower-order transport approximation discretized by either a nodal or finite difference method. For the 2D/1D neutron solver in MPACT, the 2D radial problems are solved by the 2D MOC solver, and the 1D axial problem is solved by either the nodal expansion method (NEM) solver, which uses a two-kernel formulation based on the diffusion approximation, or the simplified $P_n$ ($SP_n$) solver, which assumes that the angular flux is represented by a higher order Legendre expansion angularly and wraps a one-node NEM kernel to handle the spatial distribution. The leveraged 2D/1D gamma solver uses the $SP_n$ axial nodal solver. Specifically, the NEM-P3 solver.

### 2.2.3. Energy Deposition Scheme

The gamma heat deposition calculation capability was also implemented in MPACT [20]. The original scheme is presented by Luthi [24]. The total gamma heat deposition $H_\gamma(\boldsymbol{r})$ is calculated as equation ( 2.6 ). Note that this $H$ is different from the number of neutron groups $H$ in equation ( 2.2 ).

$$H_\gamma(\boldsymbol{r}) = \int \phi^\gamma(E^\gamma, \boldsymbol{r}) \cdot \left( \sum_i N_i(\boldsymbol{r}) \sum_x K_{i,x}(E^\gamma, \boldsymbol{r}) \right) dE^\gamma \qquad (2.6)$$

where $N_i(\boldsymbol{r})$ is the number density of isotope i. $K_{i,x}(E^\gamma, \boldsymbol{r})$ is the KERMA (Kinetic Energy Released to Material) factor for isotope *i* and reaction *x* at incident energy $E^\gamma$ and it defined as:

$$\begin{gathered} K_{i,x}(E^\gamma, \boldsymbol{r}) = \left(E^\gamma - \bar{E}_{i,x}\right) \cdot \sigma_{i,x}(E^\gamma, \boldsymbol{r}) \\ \bar{E}_{i,pe} = 0 \\ \bar{E}_{i,cs} = E^\gamma \\ \bar{E}_{i,is}(E^\gamma) = \frac{\int_0^\infty E^{\gamma\prime}\, \sigma_{is}(E^\gamma \rightarrow E^{\gamma\prime}) dE^{\gamma\prime}}{\sigma_{is}(E^\gamma)} \\ \bar{E}_{i,pp} = 1.022007\ MeV \end{gathered} \qquad (2.7)$$

where *pe* stands for photoelectric absorption, *cs* stands for coherent scattering, *is* stands for inelastic scattering (e.g. Compton scattering) and *pp* stands for pair production.

As mentioned in Section 2.2.1, HELIOS combines all the scattering reactions and pair production reactions into a single gamma incoming to gamma outgoing matrix $\sigma_s\left(E^\gamma \rightarrow E^{\gamma\prime}\right)$. Denote this combined general scattering as s, the average outgoing energy $\bar{E}_s$ is given by equation ( 2.8 ):

$$\bar{E}_s(E^\gamma) = \frac{\int_0^\infty E^{\gamma\prime}\, \sigma_s\left(E^\gamma \rightarrow E^{\gamma\prime}\right) dE^{\gamma\prime}}{\sigma_s(E^\gamma)} \qquad (2.8)$$

As a result, there are only two reaction "*x*" in equation ( 2.6 ) when using HELIOS library: *s*, standing for scattering including coherent scattering, inelastic collision and pair production, and *pe*, standing for photoelectric absorption. Equation ( 2.6 ) can then be reorganized as equation ( 2.9 ):

$$H_\gamma(\boldsymbol{r}) = \int \phi^\gamma(E^\gamma, \boldsymbol{r}) \cdot \left( \sum_i N_i(\boldsymbol{r}) \left( K_{i,s}(E^\gamma, \boldsymbol{r}) + K_{i,pe}(E^\gamma, \boldsymbol{r}) \right) \right) dE^\gamma$$

$$= \int \phi^{\gamma}(E^{\gamma}, \boldsymbol{r}) \cdot \left( \sum_i N_i(\boldsymbol{r}) \left( \left( E^{\gamma} - \bar{E}_{i,s} \right) \cdot \sigma_{i,s}(E^{\gamma}, \boldsymbol{r}) + E^{\gamma} \cdot \sigma_{i,pe}(E^{\gamma}, \boldsymbol{r}) \right) \right) dE^{\gamma}$$

$$= \int \phi^{\gamma}(E^{\gamma}, \boldsymbol{r}) \cdot \left( \sum_i N_i(\boldsymbol{r}) \begin{pmatrix} E^{\gamma} \cdot \sigma_{i,s}(E^{\gamma}, \boldsymbol{r}) \\ - \frac{\int_0^{\infty} E^{\gamma\prime}\, \sigma_{i,s}(E^{\gamma} \to E^{\gamma\prime}, \boldsymbol{r}) dE^{\gamma\prime}}{\sigma_{i,s}(E^{\gamma}, \boldsymbol{r})} \sigma_{i,s}(E^{\gamma}, \boldsymbol{r}) \\ + E^{\gamma} \cdot \sigma_{i,pe}(E^{\gamma}, \boldsymbol{r}) \end{pmatrix} \right) dE^{\gamma}$$

$$= \int \phi^{\gamma}(E^{\gamma}, \boldsymbol{r}) \cdot \left( \sum_i \begin{pmatrix} E^{\gamma} \cdot \Sigma_{i,s}(E^{\gamma}, \boldsymbol{r}) \\ - \int_0^{\infty} E^{\gamma\prime}\, \Sigma_{i,s}(E^{\gamma} \to E^{\gamma\prime}, \boldsymbol{r}) dE^{\gamma\prime} \\ + E^{\gamma} \cdot \Sigma_{i,pe}(E^{\gamma}, \boldsymbol{r}) \end{pmatrix} \right) dE^{\gamma}$$

$$= \int \phi^{\gamma}(E^{\gamma}, \boldsymbol{r}) \cdot \begin{pmatrix} \int_0^{\infty} (E^{\gamma} - E^{\gamma\prime})\, \Sigma_s(E^{\gamma} \to E^{\gamma\prime}, \boldsymbol{r}) dE^{\gamma\prime} \\ + E^{\gamma} \cdot \Sigma_{pe}(E^{\gamma}, \boldsymbol{r}) \end{pmatrix} dE^{\gamma} \qquad (2.9)$$

Equation ( 2.9 ) can be converted to multigroup form equation ( 2.10 ):

$$H_{\gamma}(\boldsymbol{r}) = \sum_{g=1}^{G} \phi_g^{\gamma}(\boldsymbol{r}) \cdot \sum_{g'=1}^{G} (\bar{E}_g - \bar{E}_{g'}) \Sigma_{s,g \to g'}(\boldsymbol{r}) + \sum_{g=1}^{G} \bar{E}_g \cdot \phi_g^{\gamma}(\boldsymbol{r}) \cdot \Sigma_{p.e,g}(\boldsymbol{r}) \qquad (2.10)$$

The multigroup terms in equation ( 2.10 ) are defined as

$$\phi_g^{\gamma}(\boldsymbol{r}) = \int_{E_g^{lower}}^{E_g^{upper}} \phi^{\gamma}(E^{\gamma}, \boldsymbol{r}) dE^{\gamma}$$

$$\Sigma_{s,g \to g'}(\boldsymbol{r}) = \frac{\int_{E_{g'}^{lower}}^{E_{g'}^{upper}} \int_{E_g^{lower}}^{E_g^{upper}} \Sigma_s(E^{\gamma} \to E^{\gamma\prime}, \boldsymbol{r}) \phi^{\gamma}(E^{\gamma}, \boldsymbol{r}) dE^{\gamma}\, dE^{\gamma\prime}}{\int_{E_g^{lower}}^{E_g^{upper}} \phi^{\gamma}(E^{\gamma}, \boldsymbol{r}) dE^{\gamma}}$$

$$\Sigma_{pe,g}(\boldsymbol{r}) = \frac{\int_{E_g^{lower}}^{E_g^{upper}} \Sigma_{pe}(E^{\gamma}, \boldsymbol{r}) \phi^{\gamma}(E^{\gamma}, \boldsymbol{r}) dE^{\gamma}}{\int_{E_g^{lower}}^{E_g^{upper}} \phi^{\gamma}(E^{\gamma}, \boldsymbol{r}) dE^{\gamma}}$$

where $E_g^{lower}$ and $E_g^{upper}$ are lower bound and upper bound of group $g$ respectively and $\bar{E}_g$ is the averaged energy of group $g$.

Although implementing the GDM method into MPACT was the initial intent, later it was decided to go with MCNP for the matrix generation as well as the benchmark reference results. However, the gamma transport solvers in MPACT are still used extensively for the development and testing of the GDM method. For example, the n-gamma source calculation procedure coupled with neutron iterations is able to provide authentic gamma source spatial distribution for GDM method tests. It also helped to verify the invariance of gamma source spectra over coupled n-gamma iteration even with burnup calculations on, which is an important observation for GDM performance optimization and will be discussed in detail in Section 4.2.2. Most importantly, developing and testing the MPACT gamma transport capability will make it easier to take the next step to allow the GDM to be computed by MPACT because GDM generation is based on gamma transport calculations. Furthermore, when the GDM method is implemented into MPACT in the future, it would also allow a direct apples to apples comparison of using MPACT with gamma transport and using MPACT with GDM.

## 2.3. Some Important Gamma Transport Physics

The primary gamma reactions include Compton scattering, pair production, and photoelectric absorption, which means photons mainly interact with electrons in the system. As a result, gamma reactions and corresponding cross sections are not very sensitive to environment changes, specifically temperature changes and fuel depletion changes. Such insensitivities can simplify neutron/gamma coupled transport iterations and the new gamma deposition matrix scheme.

Figure 2-2 is the diagram of couple neutron-gamma iterations with feedback calculations on. The overall structure is the same as Figure 2-1, except the extra step to update macro cross sections after heating calculations.

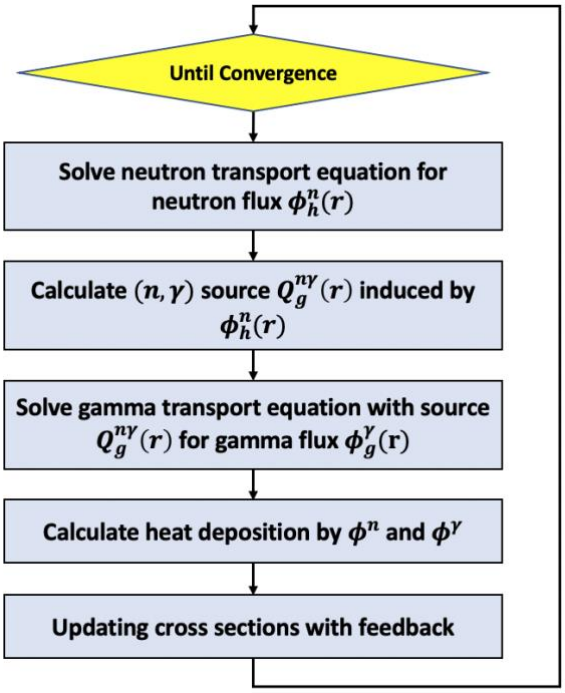


Figure 2-2 Coupled Neutron Gamma Iteration with Feedback

### 2.3.1. Insensitivity to Temperature

As photons mainly interact with electrons, microscopic pure gamma cross sections are not sensitive to temperature. The only effect on gamma transport with temperature changes would be the density of the moderator, but the gamma flux should not be very sensitive to the density of low Z materials.

This hypothesis is verified using MCNP6. A fixed gamma source is placed at the pin of coordinate (6, 5) of CASL problem 2h, and gamma transport calculations were executed at 293K and 600K separately and pin-wise heat deposition was tallied. Moderator density is set to 1.0g/cc at 293K and 0.661g/cc at 600K.

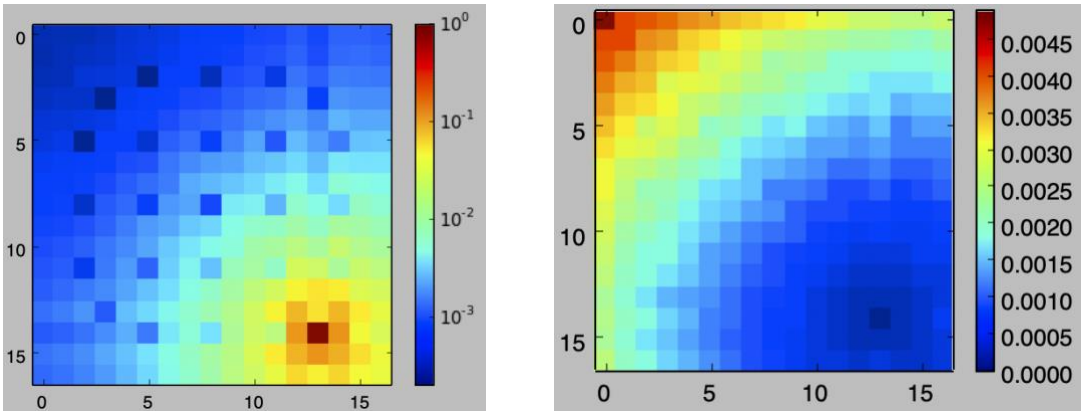


Figure 2-3 2h 293K: Gamma Heat Distribution (Left) and Uncertainty (Right)

The gamma heat distribution of 293K is shown Figure 2-3. The hottest pin is where the source is placed at. Pins far away from the source get much lower heat deposition than those close to the source, and non-fuel pins (the guide tube and $B_4C$ control rods) are cooler than the surrounding fuel pins as expected.

The 293K vs 600K differences are shown in Figure 2-4. The absolute differences are lower than 0.3%, which affirms the hypothesis that different temperatures, including different moderator densities, does not influence gamma deposition distribution significantly. The relative differences are high only in pins with low absolute deposition values. The pin cell with the highest relative error is the central empty guide tube pin. The deposition value in this pin is low, and since moderator is the dominant material in this pin, the change in moderator density can affect the deposition in this pin cell, but generally the absolute difference is negligible.

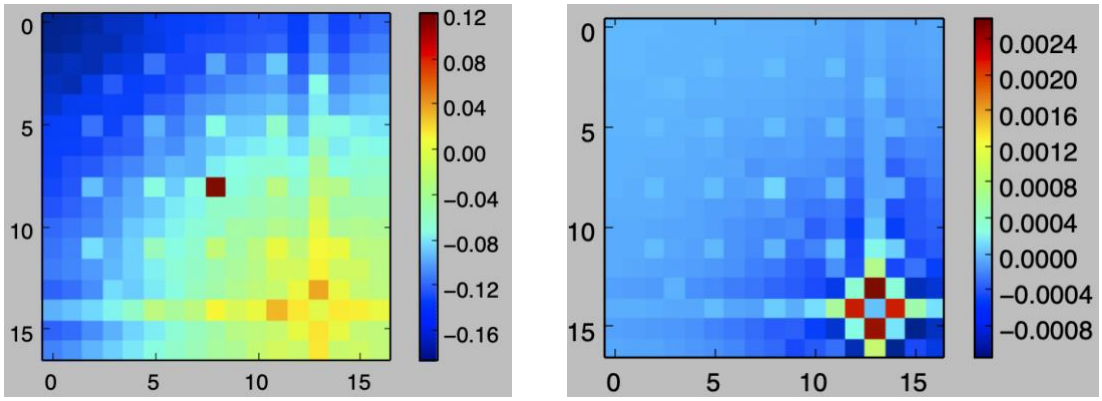


Figure 2-4 2h: 293K vs 600K Gamma Heat Deposition Relative Differences (Left) and Absolute Differences (Right)

Axially, this conclusion is also verified using VERA Progression Problem 3a [2]. VERA 3a is a three-dimensional Westinghouse 17x17-type fuel assembly with structural materials including spacer grid, nozzles and plates at beginning-of-life and hot zero power. A 3D rendering of the model is shown in Figure 2-5.

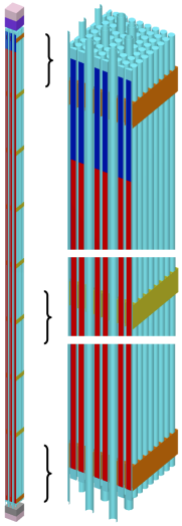

Figure 2-5 VERA Progression Problem 3a Model

A fixed source is placed in the fuel region at pin coordinate (6, 5) from height 240 cm to 250 cm. The transport calculation is performed twice on the whole problem domain, the first time at 293K with 1 g/cc moderator density and the second time at 600K with 0.661 g/cc. Radially integrated gamma heat deposition is tallied for each axial mesh layer. Deposition in meshes within the range 200 cm – 260 cm is plotted on Figure 2-6. It is clear that axial energy deposition distributions are not significantly affected by temperature changes.

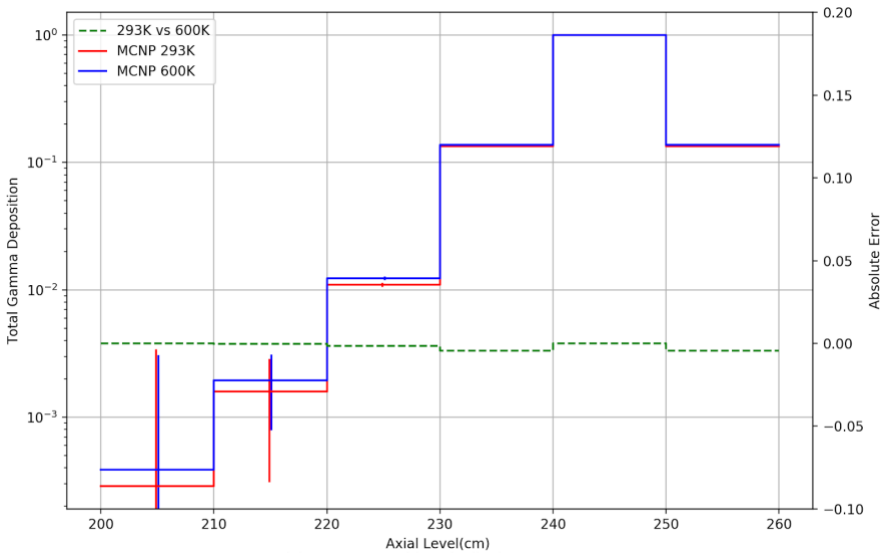


Figure 2-6 3a: Axial Gamma Heat Distribution 293K vs 600K

### 2.3.2. Insensitivity to Depletion

As photons mainly interact with electrons, gamma interactions are dominated by atomic number Z. For burnable materials, the product nuclides will be about the same Z as the initial nuclides. As for fission products, this may not be the case, but the effect may still be negligible because with U-238, the predominant isotopes will still have Z values close to 92 with depletion. This means the macroscopic gamma cross sections should be insensitive to depletion. The quantitative investigation is again performed through MCNP6. The same case as Section 2.3.1, CASL problem 2h, is used for this verification. The system is set to 293K, and the calculations are executed separately with fuels at different burnup stages assigned to the lattice, including 0.1 MWD/kgHM, 10 MWD/kgHM, 30 MWD/kgHM and 60 MWD/kgHM.

The gamma heating distribution of fresh 3.1% fuel lattice is shown in Figure 2-3. The comparison of fresh fuel and 0.1 MWD/kgHM fuel 10 MWD/kgHM, 30 MWD/kgHM and 60 MWD/kgHM are shown in Figure 2-7 through Figure 2-10.

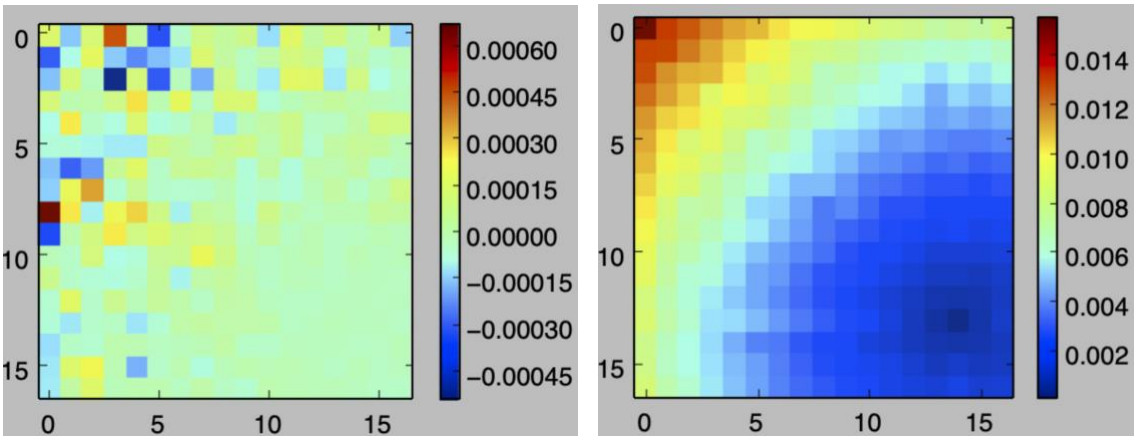


Figure 2-7 2h: Fresh vs 0.1 MWD/kgHM Gamma Heat Deposition Relative Difference (Left) and Uncertainty of 0.1 MWD/kgHM (Right)

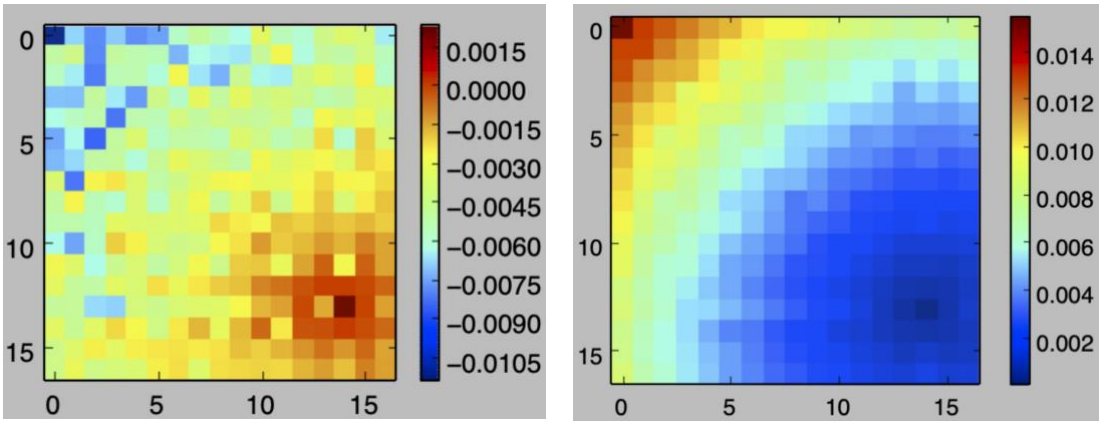


Figure 2-8 2h: Fresh vs 10 MWD/kgHM Gamma Heat Deposition Relative Difference (Left) and Uncertainty of 10 MWD/kgHM (Right)

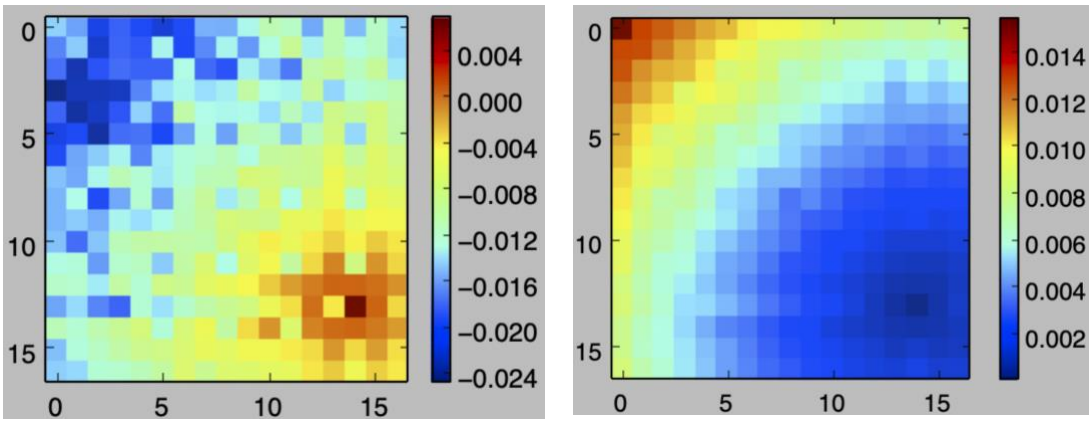


Figure 2-9 2h: Fresh vs 30 MWD/kgHM Gamma Heat Deposition Relative Difference (Left) and Uncertainty of 30 MWD/kgHM (Right)

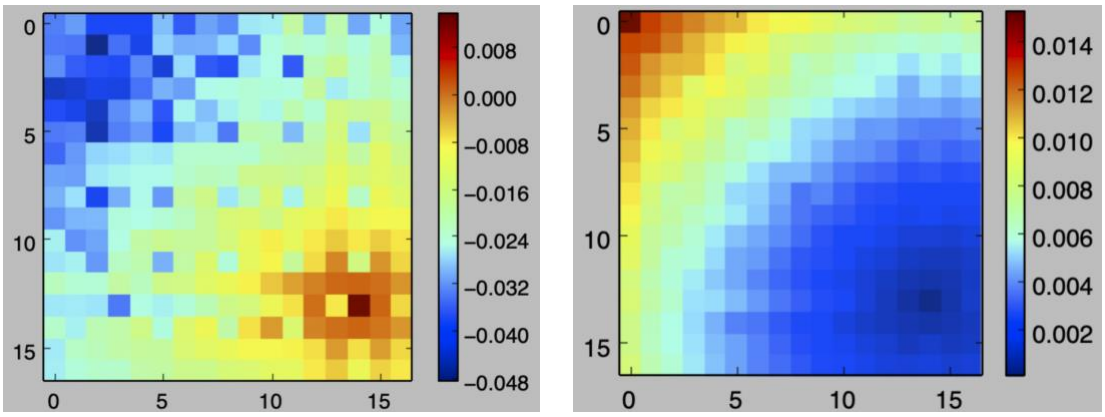


Figure 2-10 2h: Fresh vs 60 MWD/kgHM Gamma Heat Deposition Relative Difference (Left) and Uncertainty of 60 MWD/kgHM (Right)

As shown in these comparisons, the effects of fuel depletion on gamma heat deposition are only noticeable in high burnup stages (60 MWD/kgHM) at pins far away from the source where the absolute values are low and statistical errors are high. As a result, it is reasonable to conclude that fuel burnup does not influence gamma heating distribution significantly.

This chapter has shown that gamma cross sections are not sensitive to temperature or depletion. This will have a substantial impact on the gamma deposition matrix methodology to be discussed in Chapter 3.

# Chapter 3

# Gamma Deposition Matrix (GDM) Method

## 3.1. Green's Function for Gamma Deposition

Physically, when a gamma source of intensity Q in energy group *g'* is placed at pin cell *j*, denoted as $Q_{g',j}$, it can induce energy deposition in target groups *g* and target pin cells *i*, denoted as $D_{g,i}$. The process is shown in Figure 3-1. Note that the notations *g'* and *g* here are slightly different from the *g'* and *g* in the multigroup gamma transport equation ( 2.2 ). The subscripts *g'* and *g* in equation ( 2.2 ) are incoming and outgoing energy groups of scattering reactions, and those two notations in this chapter are the source energy groups and deposition energy groups respectively.

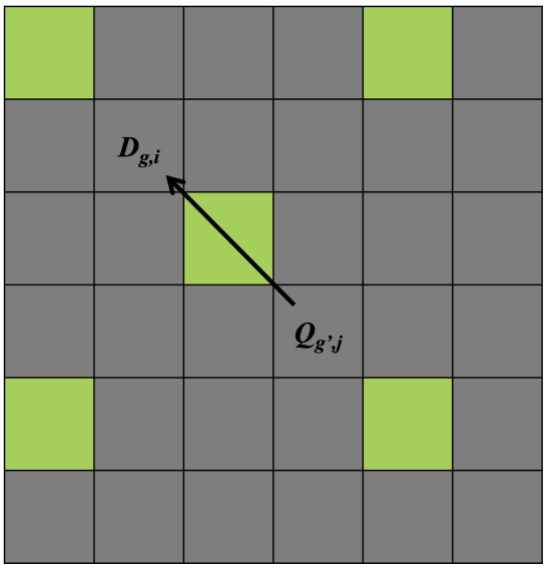


Figure 3-1 Green's Function Diagram

In a reactor assembly or core case, gamma deposition in cell *i* is contributed by multiple $Q_{g',j}$ in different groups *g'* and cells *j*. To clearly distinguish the origin of the energy, energy deposition in target group *g* and target cell *i* induced by gamma source in source

group $g'$ and source cell $j$ is denoted as $D_{g',j\to g,i}$. The total deposition in cell $i$ and group $g$ can be obtained by summing $D_{g',j\to g,i}$ over all the source groups and cells as $D_{g,i} = \sum_{g'}\sum_j D_{g',j\to g,i}$.

The mathematical expression of Green's function $D_{g',j\to g,i}$ can be derived from the isotropic gamma transport equation ( 3.1 ) but the extension to higher-order scattering is straightforward.

$$\begin{aligned} \boldsymbol{\Omega}\cdot\nabla\psi^{\gamma}(\boldsymbol{r},\boldsymbol{\Omega},E^{\gamma}) + \Sigma_t^{\gamma}(\boldsymbol{r},E^{\gamma})\psi^{\gamma}(\boldsymbol{r},\boldsymbol{\Omega},E^{\gamma}) &= Q^{scat}(\boldsymbol{r},E^{\gamma}) + Q^{n\gamma}(\boldsymbol{r},E^{\gamma}) \\ Q^{scat}(\boldsymbol{r},E^{\gamma}) &= \frac{1}{4\pi}\int_0^{\infty}\Sigma_{s0}^{\gamma}(\boldsymbol{r},E^{\gamma\prime}\to E^{\gamma})\phi^{\gamma}(\boldsymbol{r},E^{\gamma\prime})\,dE^{\gamma\prime} \\ Q^{n\gamma}(\boldsymbol{r},E^{\gamma}) &= \frac{1}{4\pi}\int_0^{\infty}\Sigma_{n\gamma}(\boldsymbol{r},E^{n}\to E^{\gamma})\phi^{n}(\boldsymbol{r},E^{n})dE^{n} \end{aligned} \qquad (3.1)$$

First, define the operator M

$$\begin{aligned} M\cdot\psi(\boldsymbol{r},\boldsymbol{\Omega},E^{\gamma}) = \boldsymbol{\Omega}\cdot\nabla\psi^{\gamma}(\boldsymbol{r},\boldsymbol{\Omega},E^{\gamma}) + \Sigma_{tr}^{\gamma}(\boldsymbol{r},\boldsymbol{\Omega},E^{\gamma})\psi^{\gamma}(\boldsymbol{r},\boldsymbol{\Omega},E^{\gamma}) \\ -\frac{1}{4\pi}\int_0^{\infty}\Sigma_{s0}^{\gamma}\left(\boldsymbol{r},E^{\gamma\prime}\to E^{\gamma}\right)\phi^{\gamma}\left(\boldsymbol{r},E^{\gamma\prime}\right)dE^{\gamma\prime} \end{aligned} \qquad (3.2)$$

which gives

$$M\cdot\psi^{\gamma}(\boldsymbol{r},\boldsymbol{\Omega},E^{\gamma}) = Q^{n\gamma}(\boldsymbol{r},E^{\gamma}) \qquad (3.3)$$

Next, define $G\left(\boldsymbol{r_0}\to\boldsymbol{r},\ \boldsymbol{\Omega_0}\to\boldsymbol{\Omega},\ E_0^{\gamma}\to E^{\gamma}\right)$ such that

$$M\cdot G\left(\boldsymbol{r_0}\to\boldsymbol{r},\boldsymbol{\Omega_0}\to\boldsymbol{\Omega},E_0^{\gamma}\to E^{\gamma}\right) = \delta(\boldsymbol{r}-\boldsymbol{r_0})\delta(\boldsymbol{\Omega}-\boldsymbol{\Omega_0})\delta(E^{\gamma}-E_0^{\gamma}) \qquad (3.4)$$

Thus, angular flux $\psi^{\gamma}(\boldsymbol{r},\boldsymbol{\Omega},E^{\gamma})$ can be expressed as

$$\psi^{\gamma}(\boldsymbol{r},\boldsymbol{\Omega},E^{\gamma}) = \int_0^{\infty}\int_0^{\infty}\int_{4\pi}G\left(\boldsymbol{r_0}\to\boldsymbol{r},\boldsymbol{\Omega_0}\to\boldsymbol{\Omega},E_0^{\gamma}\to E^{\gamma}\right)Q^{n\gamma}\left(\boldsymbol{r_0},E_0^{\gamma}\right)d\Omega_0\,dE_0^{\gamma}\,dr_0 \qquad (3.5)$$

and scalar flux $\phi(\boldsymbol{r},E^{\gamma})$ is

$$\phi^{\gamma}(\boldsymbol{r},E^{\gamma}) = \int_{4\pi}\int_0^{\infty}\int_0^{\infty}\int_{4\pi}G\left(\boldsymbol{r_0}\to\boldsymbol{r},\boldsymbol{\Omega_0}\to\boldsymbol{\Omega},E_0^{\gamma}\to E^{\gamma}\right)Q^{n\gamma}\left(\boldsymbol{r_0},E_0^{\gamma}\right)d\Omega_0\,dE_0^{\gamma}\,dr_0\,d\Omega \qquad (3.6)$$

By the definition of Green's function and delta function, the phase space variables $\boldsymbol{r_0}, \boldsymbol{\Omega_0}, E_0^{\gamma}$ describe the gamma sources and $\boldsymbol{r}, \boldsymbol{\Omega}, E^{\gamma}$ describe the energy deposition in the targets.

The multigroup gamma scalar flux in cell *i* and group *g* is obtained by integrating ( 3.6 ) over energy group *g* and cell *i*:

$$\phi_{g,i}^{\gamma} = \int_{g^{lower}}^{g^{upper}} \int_{V_i} \int_{4\pi} \int_0^{\infty} \int_0^{\infty} \int_{4\pi} G\left(\boldsymbol{r_0} \to \boldsymbol{r}, \boldsymbol{\Omega_0} \to \boldsymbol{\Omega}, E_0^{\gamma} \to E^{\gamma}\right) Q^{n\gamma}\left(\boldsymbol{r_0}, E_0^{\gamma}\right) d\Omega_0 \, dE_0^{\gamma} \, dr_0 \, d\Omega dr dE^{\gamma} \quad (3.7)$$

And if the integration of $E_0^{\gamma}$ and $\boldsymbol{r_0}$ are reduced to group *g'* and cell *j* only respectively, equation ( 3.7 ) becomes "gamma scalar flux in cell *i* and group *g* induced by gamma source in group *g'* and cell *j* as $\phi_{g',j\to g,i}^{\gamma}$ in equation ( 3.8 )

$$\phi_{g',j\to g,i}^{\gamma} = \int_{g^{lower}}^{g^{upper}} \int_{V_i} \int_{4\pi} \int_{V_j} \int_{g'^{lower}}^{g'^{upper}} \int_{4\pi} G\left(\boldsymbol{r_0} \to \boldsymbol{r}, \boldsymbol{\Omega_0} \to \boldsymbol{\Omega}, E_0^{\gamma} \to E^{\gamma}\right) Q^{n\gamma}\left(\boldsymbol{r_0}, E_0^{\gamma}\right) d\Omega_0 \, dE_0^{\gamma} \, dr_0 \, d\Omega dr dE^{\gamma} \quad (3.8)$$

$D_{g',j\to g,i}$, the energy deposition in target group *g* and target cell *i* induced by gamma source in source group *g'* and source cell *j*, can be derived similarly. The first step would be to combine gamma heat equation ( 2.6 ) in chapter 2.2.3 with scalar flux ( 3.6 ),

$$\begin{aligned} D(\boldsymbol{r}, E^{\gamma}) &= \phi^{\gamma}(E^{\gamma}, \boldsymbol{r}) \cdot \left(\sum_i N_i(\boldsymbol{r}) \sum_x K_{i,x}(E^{\gamma}, \boldsymbol{r})\right) \\ &= \left(\sum_i N_i(\boldsymbol{r}) \sum_x K_{i,x}(E^{\gamma}, \boldsymbol{r})\right) \int_{4\pi} \int_0^{\infty} \int_0^{\infty} \int_{4\pi} G\left(\boldsymbol{r_0} \to \boldsymbol{r}, \boldsymbol{\Omega_0} \to \boldsymbol{\Omega}, E_0^{\gamma} \to E^{\gamma}\right) Q^{n\gamma}\left(\boldsymbol{r_0}, E_0^{\gamma}\right) d\Omega_0 \, dE_0 \, dr_0 \, d\Omega \end{aligned} \quad (3.9)$$

which is the total gamma deposition at position $\boldsymbol{r}$ and energy $E^{\gamma}$.

And integrating it over target gamma group *g* and cell *i*, the multigroup total deposition in group *g* and *i*, $D_{g,i}$, can be obtained as ( 3.10 )

$$D_{g,i} = \int_{g^{lower}}^{g^{upper}} \int_{V_i} \int_{4\pi} \int_0^{\infty} \int_0^{\infty} \int_{4\pi} \left( \sum_i N_i(\boldsymbol{r}) \sum_x K_{i,x}(E^{\gamma}, \boldsymbol{r}) \right) G\left(\boldsymbol{r_0} \to \boldsymbol{r}, \boldsymbol{\Omega_0} \to \boldsymbol{\Omega}, E_0^{\gamma} \to E^{\gamma}\right) Q^{n\gamma}\left(\boldsymbol{r_0}, E_0^{\gamma}\right) d\Omega_0 \, dE_0^{\gamma} \, dr_0 \, d\Omega dr dE^{\gamma} \quad (3.10)$$

If, instead of the total deposition in cell *i* and group *g*, the deposition in that range induced by gamma source in a certain group(*g'*) and cell(*j*) is interested, the integration of $E_0^{\gamma}$ and $\boldsymbol{r_0}$ can be reduced to group *g'* and cell *j* respectively to obtain this value just like the procedure used in equation ( 3.7 ) through ( 3.8 ):

$$D_{g',j\to g,i} = \int_{g^{lower}}^{g^{upper}} \int_{V_i} \int_{4\pi} \int_{V_j} \int_{g'^{lower}}^{g'^{upper}} \int_{4\pi} \left( \sum_i N_i(\boldsymbol{r}) \sum_x K_{i,x}(E^{\gamma}, \boldsymbol{r}) \right) G\left(\boldsymbol{r_0} \to \boldsymbol{r}, \boldsymbol{\Omega_0} \to \boldsymbol{\Omega}, E_0^{\gamma} \to E^{\gamma}\right) Q^{n\gamma}\left(\boldsymbol{r_0}, E_0^{\gamma}\right) d\boldsymbol{\Omega_0} \, dE_0^{\gamma} \, d\boldsymbol{r_0} \, d\boldsymbol{\Omega} d\boldsymbol{r} dE^{\gamma} \quad (3.11)$$

The ratio of the deposition, $D_{g',j\to g,i}$, and the source, $Q_{g',j}^{n\gamma}$, will be defined as

$$F_{g',j\to g,i} = D_{g',j\to g,i} / Q_{g',j}^{n\gamma} \quad (3.12)$$

This value will be the entry of the gamma deposition matrix element. The multigroup $(n,\gamma)$ source is defined as $Q_{g',j}^{n\gamma} = \int_{g'^{lower}}^{g'^{upper}} \int_{V_j} Q^{n\gamma}(\boldsymbol{r}, E^{\gamma}) d\boldsymbol{r} \, dE^{\gamma}$. In the rest of this thesis, $Q^{n\gamma}(\boldsymbol{r}, E^{\gamma})$ will be written as $Q(\boldsymbol{r}, E^{\gamma})$ and the multigroup forms are simplified accordingly. As described in Section 2.3, the source $Q_{g',j}$ can be easily calculated after neutron sweep in a standalone procedure. So as long as $F_{g',j\to g,i}$ is known, heat deposition can easily be calculated through simple matrix multiplications and summations. The multiplication calculation scheme will be discussed in Section 3.2 and the generation of $F_{g',j\to g,i}$ will be discussed in Section 3.3.

## 3.2. Gamma Deposition Matrix (GDM)

With $D_{g',j\to g,i} = F_{g',j\to g,i} * Q_{g',j}$ from equation ( 3.12 ) where $F_{g',j\to g,i}$ is a known value and $Q_{g',j}$ is calculated based on neutron flux, the total deposition in group *g* and cell *i* can

be expressed as $D_{g,i} = \sum_{g'} \sum_j D_{g',j\to g,i} = \sum_{g'} \sum_j F_{g',j\to g,i} * Q_{g',j}$ , which is equivalent to the matrix multiplication scheme shown in equation ( 3.13 ):

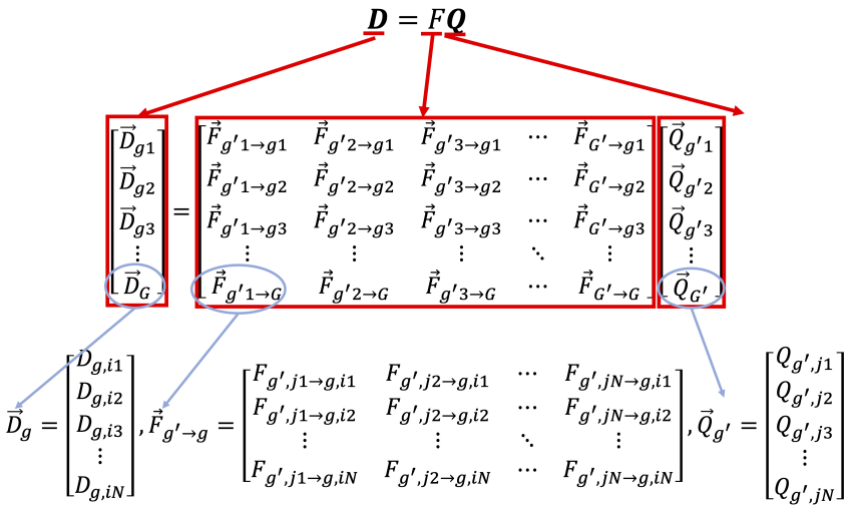


( 3.13 )

where N is the total number of pin cells in the problem, *g1*, *g2*…, *g'1*, *g'2*, … are different gamma energy groups, *G'* and *G* are the total number of gamma energy groups. Note that the value of *G'* and that of *G* are the same. The reason to use two different notations is to distinguish the source groups and target groups. ***D*** and ***Q*** are energy deposition vector and source vector respectively, and the matrix *F* is the Gamma Deposition Matrix (GDM). As there are *N* pin cells and *G* energy groups, ***D*** and ***Q*** are of size *N*G* and *F* is *N*N*G*G*. This matrix-vector multiplication scheme gives the possibility to calculate gamma deposition without explicitly solving the gamma transport equation. Within a coupled neutron-gamma iteration, this step is performed to substitute the gamma transport solver and heat deposition calculations (the third block and part of the fourth block on Figure 2-2). This method can make the gamma deposition calculation process much simpler and can be significantly faster than solving the transport equation.

## 3.3. Generation of GDM

By the definition in equation ( 3.12 ), if the intensity of the source $Q_{g',j}$ is 1, $F_{g',j\to g,i}$ would simply be the same as deposition $D_{g',j\to g,i}$. In other words, $F_{g',j\to g,i}$ can be physically interpreted as "deposition in group *g* and pin *i* induced by unit source in group

*g'* and pin *j*", which is essentially a discrete Green's function for energy deposition. Thus, to generate the matrix entries $F_{g',j\to g,i}$, a unit source in energy group *g'* will be placed at cell *j*, then the transport equation will be solved on the whole problem domain as a fixed source problem, and finally heat deposition in each energy group *g* and pin cell *i* will be tallied. And the deposition in *g* and *i* will be $F_{g',j\to g,i}$. This process is shown in Figure 3-2.

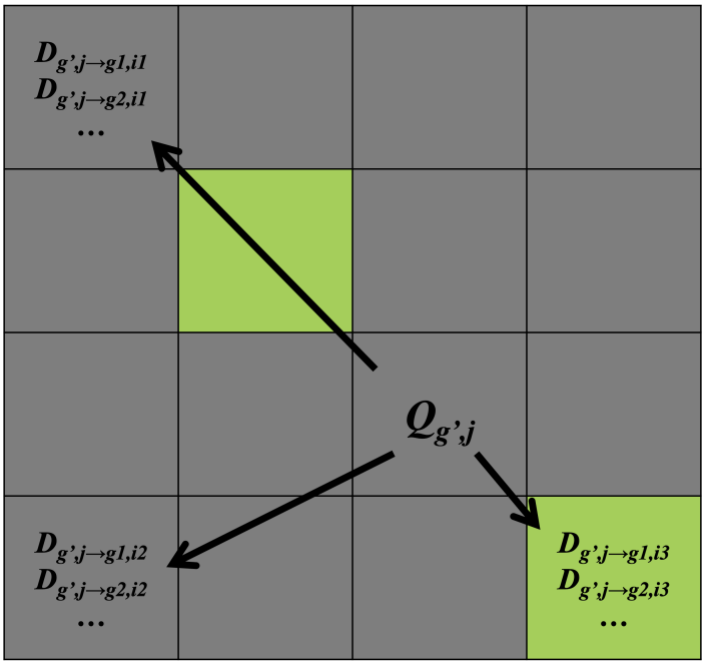


Figure 3-2 Generation of GDM's Green's Function

To generate the full GDM, the fixed source run will be repeated with the unit source in different cell *j* and group *g'*, and as a result *N* * *G* fixed source runs will be executed. Within each of the runs, deposition in each cell *i* and group *g*, a total of *N* * *G* values, will be tallied and stored. For ease of description in later chapters, each of these *N* * *G* fixed source runs will be named as "matrix generation fixed source run" or simply "matrix generation run".

In general, $F_{g',j\to g,i}$ changes with changes in cross sections along the path from *j* to *i*. That makes it painful to use this method on neutronics problems with thermal feedback or burnup effects on. When the cross sections are updated after each iteration, the whole

matrix has to be regenerated correspondingly. Obviously, recalculating the whole matrix in each iteration can be very computationally expensive and would be much slower than solving the transport equation directly. However, as shown in Section 2.3.1, pure gamma cross sections are insensitive to temperature changes and thus thermal feedback effects, which means matrix elements $F_{g',j\to g,i}$ would not change significantly over thermal feedback iterations. As a result, the GDM can be pre-calculated and stored in advance and used over thermal feedback iterations without any additional transport calculations during the iterations. Even with burnup calculations on, as introduced in Section 2.3.2, gamma deposition is only slightly affected in low deposition pins of very high burnup stages. In this case, it may be necessary to recalculate the GDM after some high burnup stages if very high accuracy is required but this needs to be examined more closely for a specific configuration.

In summary, the GDM method substitutes the explicit transport equation with a much simpler matrix-vector multiplication scheme, and the insensitivity of gamma cross sections to temperature and depletion make it possible to pre-calculate the matrix and store it once for all gamma calculations, including T-H iterations, during a depletion cycle.

# Chapter 4
# Groupwise Reduced GDM

Although the GDM can be pre-calculated and stored to use over neutron-gamma iterations and depletion as verified in Section 3.1, it is still expensive to generate and store such a big matrix. As introduced in Section 3.3, there are *N*G* matrix generation runs to be executed, and each of them is about solving the transport equation on the whole problem domain and tallying *N*G* values. Thus, there are *N*N*G*G* tallied results to be stored explicitly. For example, the VERA Progression Problem 4a-2d [2] has 3x3 assemblies and 17x17 pins in each assembly. If 18 gamma groups as with the HELIOS library are used, there are 46818 matrix generation runs and in each of them there are 46818 values to be computed and stored. Furthermore, whole core problems like VERA Progression Problem 5a-2d [2] would be even more prohibitive. To reduce the size of the GDM and make it more useful, several simplifications on reducing the group dependence of the GDM will be applied to optimize the generation and storage process.

## 4.1. Integrating Out the Deposition Spectral Dependence

The GDM method is developed to calculate gamma heat deposition for heating distribution calculations and thermal feedback calculations. For either of these purposes, there is no need to know the groupwise heat deposition in target cell *i*. Instead, only the total energy deposition in *i* is required. A new term $D_{g',j\to i}$ is physically defined as "the total heat deposition in target cell *i* induced by a gamma source in group *g'* and cell *j*". Mathematically speaking, it is obtained by integrating the groupwise deposition $D_{g',j\to g,i}$ over target group *g* as given in equation ( 4.1 ):

$$D_{g',j\to i} = \sum_g D_{g',j\to g,i} = \sum_g F_{g',j\to g,i}\, Q_{g',j} \qquad (4.1)$$

where $D_{g',j\to g,i}$ is expanded by equation ( 3.12 ). The source term $Q_{g',j}$ is independent of the target group $g$, and thus the summation can be rewritten as

$$D_{g',j\to i} = (\sum_g F_{g',j\to g,i}) Q_{g',j} = F_{g',j\to i} Q_{g',j} \qquad (4.2)$$

in which a new matrix entry is defined as $F_{g',j\to i} = \sum_g F_{g',j\to g,i}$. By using equation ( 4.2 ) and $F_{g',j\to i}$, even without the more detailed term $F_{g',j\to g,i}$, the total heat deposition in all the cell $i$'s can be calculated exactly.

To generate the new GDM of $F_{g',j\to i}$, there are still *N*G'* matrix generation runs to be performed. However, within each of the runs, there are only N values to be tallied and stored instead of *N*G* as in $F_{g',j\to g,i}$. For transport code systems whose performances are sensitive to the number of tallies such as MCNP, reducing the number of tallies can significantly improve the speed of the matrix generation process. Furthermore, regardless of the code systems, reducing the number of values in the GDM can improve the matrix-vector multiplication speed and also reduce the space required to store the matrix from *N*N*G*G'* to *N*N*G'*. The size reduction from $F_{g',j\to g,i}$ to $F_{g',j\to i}$ is shown by the diagrams in Table 4-1.

Table 4-1 Integrating Out the Deposition Spectral Dependence

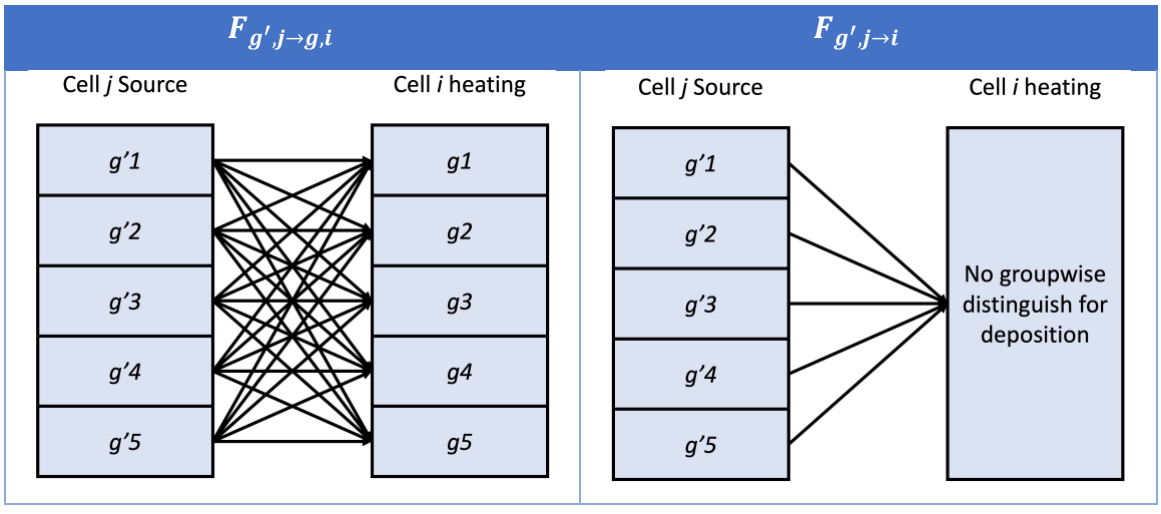

## 4.2. Neglecting Source Spectral Dependence

As the size of the matrix is reduced to *N*N*G'* by getting rid of the group dependence on the target (deposition) side, the next step would be to explore if there exists an approach that can get rid of the group dependence on the source side as well. If this assumption can be valid, the matrix will be further reduced to size *N*N*, which is a relationship between total heat deposition in cell *i* and total source intensity in cell *j*.

Mathematically speaking, the gamma source can be separated as the intensity multiplied by its spectrum as ( 4.3 ):

$$Q_{g',j} = \chi_{j,g'} Q_j \qquad (4.3)$$

where $\chi_{j,g'}$ is the spectrum and $Q_j$ is the intensity. Then put it back into equation ( 4.2 ) and sum over source group *g'*,

$$D_{j\to i} = \sum_{g'} D_{g',j\to i} = \sum_{g'} F_{g',j\to i} Q_{g',j}$$

$$= \sum_{g'} F_{g',j\to i} \chi_{j,g'} Q_j$$

If the spectrum $\chi_{j,g'}$ does not change over neutron-gamma iterations just like $F_{g',j\to i}$, the summation term stays invariant. As a result, the whole term can be pre-calculated and stored just as a GDM, and the new matrix multiplication scheme is presented by equation ( 4.4 ):

$$D_{j\to i} = (\sum_{g'} F_{g',j\to i} \chi_{j,g'}) Q_j = F_{j\to i} Q_j \qquad (4.4)$$

where $F_{j\to i} = \sum_{g'} F_{g',j\to i} \chi_{j,g'}$ are the new GDM entries without energy group dependence.

The physical interpretation would be that, for the matrix entries to be simplified as $F_{j\to i}$, as the sources in cell *j* are different over iterations, the total deposition in cell *i* induced by sources in cell *j* should be linearly proportional to the intensity of the sources. For example, if the intensity of the source in *j* after the *l*th iteration is $Q_j^l$, that after the k-th iteration is

$Q_j^k$, and the intensities of the sources are off by a factor of c such that $Q_j^l = cQ_j^k$, the corresponding induced heat deposition should be $D_{j\to i}^l = cD_{j\to i}^k$.

For this to be strictly true, the two sources $Q_j^l$ and $Q_j^k$ must have identical spectra. If the two spectra are different, taking an extreme example, if one source is mainly in energy groups < 100 eV and the other source is mainly in groups > 1 MeV, the attenuation pattern along the path from *j* to *i* would be quite different, leading to different gamma spectra at *i* due to these sources. As a result, heat deposition will not be linearly proportional to source intensity. However, intuitively speaking, if the spectra of $Q_j^l$ and $Q_j^k$ are approximately the same, $Q_j^l$ would just be the same source as $Q_j^k$ but scaled by a factor of c. They will have similar attenuation pattern along the *j* to *i* path, induce flux of similar spectra with the scaling factor c and finally induce heat deposition different by the same factor c. Then with equation ( 4.2 ), the heat deposition induced by an arbitrary group *g'* will have the relationship $D_{j,g'\to i}^l = cD_{j,g'\to i}^k$, and summing it over *g'* will give $D_{j,\to i}^l = cD_{j,\to i}^k$.

The rest of Section 4.2 will investigate the changes of gamma source spectra over neutron-gamma coupled iterations and discuss whether it is feasible to assume a constant gamma source spectrum in each cell *j*.

### 4.2.1. Invariance of Gamma Source Spectrum Over Coupled $(n, \gamma)$ Iterations

If gamma source spectra are insensitive to incident neutron spectra, or equivalently spectra of gamma sources induced by incident neutron in different energy groups are similar, it would be reasonable to conclude that gamma source spectra are invariant over coupled neutron-gamma calculations because potentially varying incident neutron spectra do not affect gamma production spectrum. Overall, this is a valid assumption for U-235 and is a reasonable assumption for U-238, as will be described in the following paragraphs.

Figure 4-1 includes the normalized $(n, \gamma)$ production cross sections of U-235 as a function of gamma energy group. The plots are normalized to unity. The x-axis is gamma energy

in group $g$, $E_g$, and the y-axis is the normalized $(n,\gamma)$ cross section at 293K from the HELIOS library for the corresponding neutron group. The normalized $(n,\gamma)$ cross section for a neutron in group $h$ to yield a gamma in group $g$ is defined as $\Sigma_{n\gamma,h\to g}/\Sigma_{n\gamma,h}$ where $\Sigma_{n\gamma,h} = \sum_{g=1}^{18} \Sigma_{n\gamma,h\to g}$ because HELIOS has 18 gamma groups. Different lines correspond to different incident neutron energy groups with the legend indicating the neutron energy group. In other words, each line is proportional to the gamma source spectrum induced by neutrons in the specified neutron group.

For U-235, most of the lines have the same shape, which suggests that the gamma production spectra by neutrons in different groups are generally similar. The lines induced by incident neutrons in group 19, 20 and 22, which are 7.34 eV, 6.48 eV and 5.04 eV respectively, are slightly different from the others but not by a significant amount, so it is reasonable to conclude that the $(n,\gamma)$ source spectrum from U-235 is relatively insensitive to the incident neutron energy.

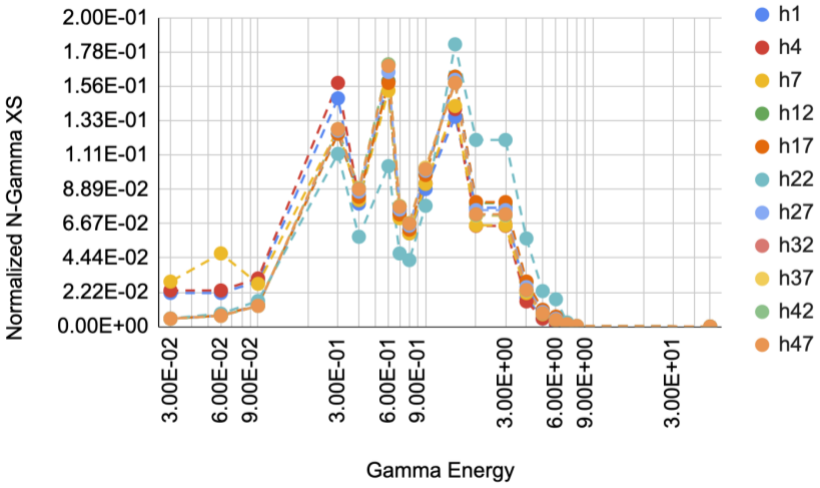


Figure 4-1 Normalized $(n,\gamma)$ Production Cross Sections of U-235

Gamma source spectra of U-238 is a little more complicated than for U-235. Figure 4-2 through Figure 4-5 are $(n,\gamma)$ cross sections of selected neutron groups of U-238. From these figures, one can see that there are four different patterns of gamma source spectra for different incident neutron energy. Gamma production spectra induced by neutrons in group 1-4 (1.35 MeV and above) are similar, those induced by neutron in group 6-8 (higher than

67.4 keV and lower than 821 keV) are similar, those induced by neutrons in group 9-47 (67.4 keV or lower) are identical, and the gamma source spectrum induced by neutrons in group 5 is unique.

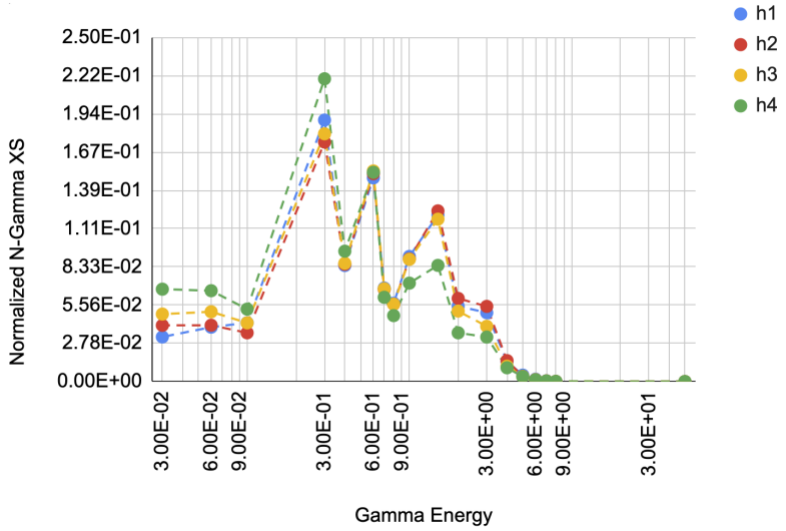


Figure 4-2 Normalized $(n, \gamma)$ Production Cross Sections of U-238 by Incident Neutron in Group 1-4

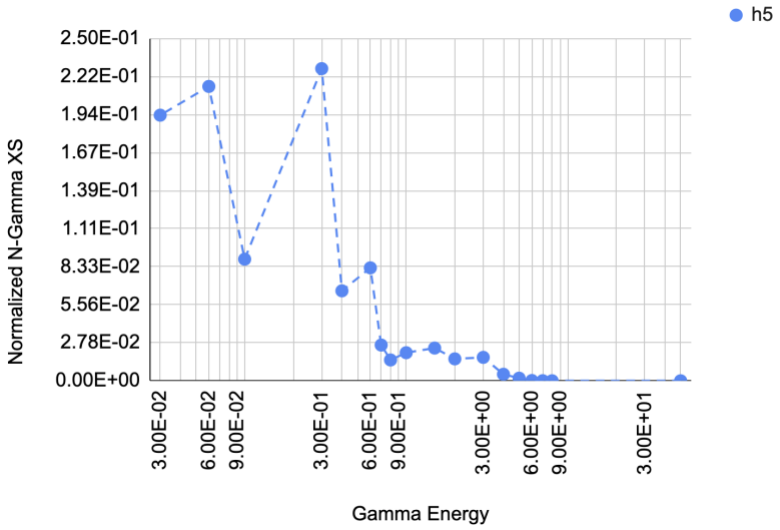


Figure 4-3 Normalized $(n, \gamma)$ Production Cross Sections of U-238 by Incident Neutron in Group 5

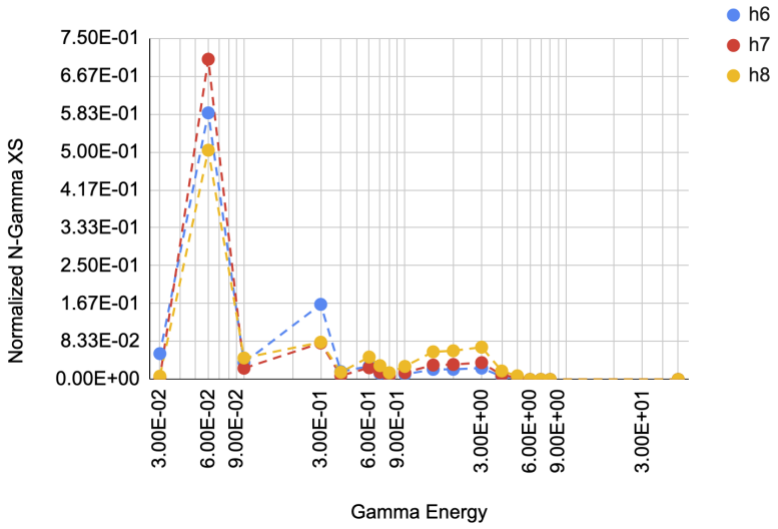


Figure 4-4 Normalized $(n, \gamma)$ Production Cross Sections of U-238 by Incident Neutron in Group 6-8

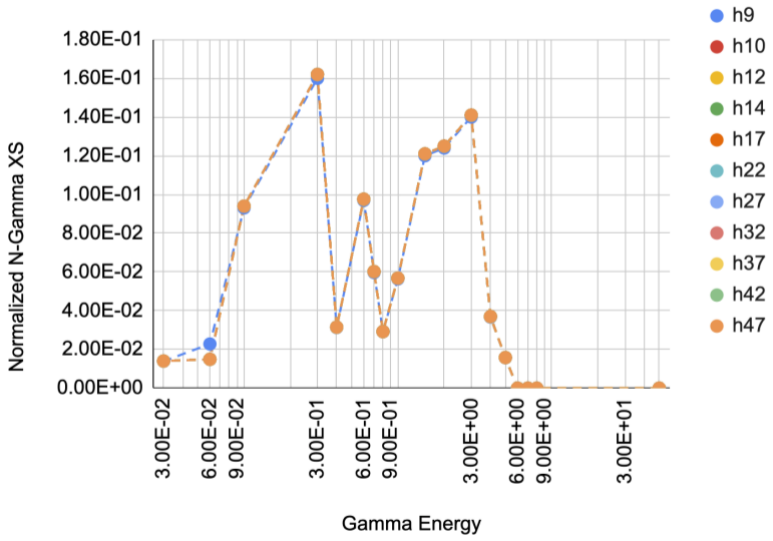


Figure 4-5 Normalized $(n, \gamma)$ Production Cross Sections of U-238 by Incident Neutron in Group 9-47

The reason for such differences is that they are from different neutron reactions. Gamma production induced by high energy neutrons is mainly from fast fission and inelastic scattering in U-238, while gammas induced by epithermal and thermal neutrons are mainly from neutron capture reactions. Although there are 4 different patterns for U238 gamma production spectra induced by incident neutrons in 47 different energy groups, the total gamma source spectrum can still be relatively invariant over n-gamma iterations because local changes in the neutron flux spectrum, such as what might be expected in a T-H

iteration, will not significantly affect the induced gamma source spectra. For ease of description, neutron flux in iteration $l_1$ and $l_2$ are defined as $\phi^n_{h,l_1}(\boldsymbol{r})$ and $\phi^n_{h,l_2}(\boldsymbol{r})$ respectively. For example, if $\phi^n_{h,l_2}(\boldsymbol{r})$ is higher in group 3 and lower in group 1 compared to $\phi^n_{h,l_1}(\boldsymbol{r})$, the gamma source spectra induced by $\phi^n_{h,l_1}(\boldsymbol{r})$ and $\phi^n_{h,l_2}(\boldsymbol{r})$ should be the same because normalized n-gamma XS of group 1 incident neutrons has the same pattern as the normalized n-gamma XS of group 3 incident neutrons. In contrast, the gamma source spectra would be noticeably different if $\phi^n_{h,l_2}(\boldsymbol{r})$ is higher in group 20 and lower in group 1 compared to $\phi^n_{h,l_1}(\boldsymbol{r})$ by an outstanding amount. However, such global and significant changes of neutron flux spectrum over iterations are not expected to be common in practice. Figure 4-6 shows the normalized neutron flux after the first, the 5th and the last iterations of the simplified pin cell problem in Figure 1-1. CMFD was turned on. The plot indicates that the neutron flux spectrum after the first iteration is very close to the final converged spectrum. With this modest change in the neutron spectrum over T-H iterations, it is reasonable to conclude that the neutron induced gamma source spectrum of U-238 is relatively invariant, especially considering the global changes of the neutron flux are very subtle.

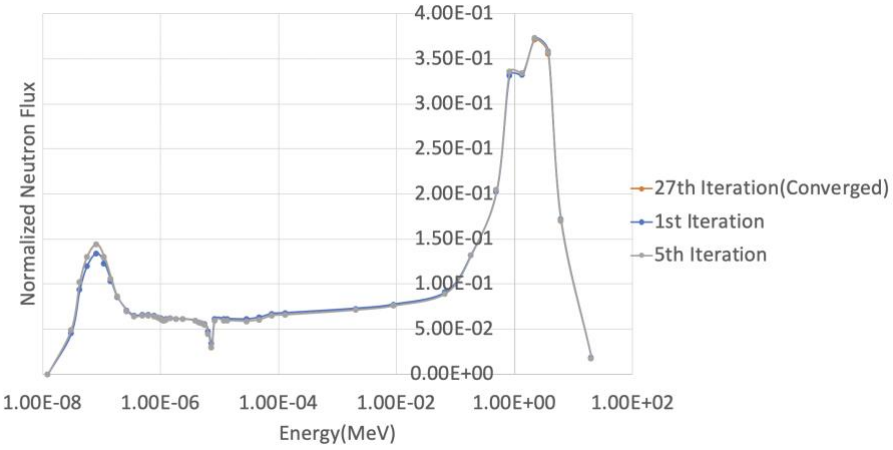


Figure 4-6 Normalized Neutron Flux Changes Over T-H Iterations in MPACT

Lastly, for LWR cases, there are only a small number of fast fission reactions in the system, so it is expected that most of the gamma productions are still induced by neutron in group 9-47. Quantitatively, if the fuel rod is a typical LWR fuel with 3.1% enrichment and neutron flux in the fuel is the same as Figure 4-6, it was found that the gamma release by

fast neutron reactions with U-238 counts for <10.0% of the total gamma release. However, since the energy carried by gamma rays counts for only 10% of all the energy released in a LWR system, the gamma release induced by fast fission contributes less than 1% of the total fission energy deposition.

### 4.2.2. Insensitivity of the Gamma Source Spectrum with Depletion

Section 2.3.2 showed that the overall gamma energy deposition in a typical LWR configuration is not sensitive to depletion because depletion products have similar Z numbers as the initial isotopes for high Z materials. Due to the same reason, the gamma source spectra are also relatively insensitive to depletion. To prove this assumption more directly and experimentally, gamma source spectra at different depletion steps and at different neutron-gamma iterations are plotted and compared. MPACT is again used for this verification and the test case used is the same as the one in Section 4.2.1, a pin cell at 293K with 3.1% fuel rod. The gamma spectra for several burnup steps are plotted in Figure 4-7.

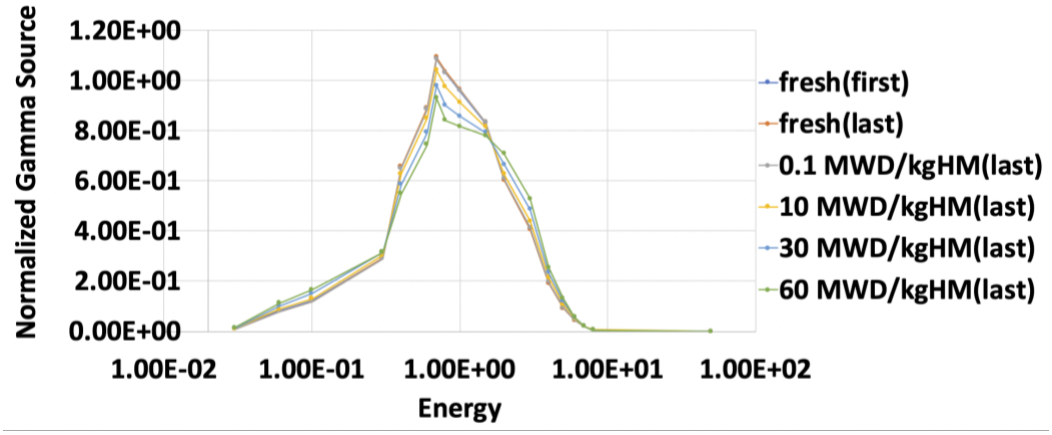


Figure 4-7 Gamma Source Spectra Over Iterations with Burnup Calculations On

First/last in parentheses in the legend means the first/last iteration of the corresponding burnup stage. Overall, the gamma source spectrum is relatively constant even at 60 MWD/kgHM burnup. The spectrum does harden with burnup but only slightly, so there is no need to recalculate the GDM for every burnup stage.

## 4.3. Summary

This chapter has shown that the GDM is not a function of the spectrum of the energy deposition. This is exact since the overall energy deposition is simply an integral over the target energy groups. It has also been demonstrated that gamma source spectra are relatively constant over coupled neutron-gamma iterations for a given depletion step. Finally, it was shown that the gamma source spectrum is relatively insensitive to burnup. This invariance indicates that the new gamma deposition matrix entries $\sum_{g'} F_{g',j\to i}\chi_{j,g'}$ in equation ( 4.4 ) do not change and can be summed over source energy groups to yield the new GDM $F_{j\to i}$. This matrix can be pre-calculated and used over iterations and during a complete cycle without additional transport calculations during the T-H iterations or at different burnups. The resultant GDM is shown next.

To obtain the mathematical expression of $F_{j\to i}$, equation ( 4.4 ) is combined with equation ( 4.2 ) to yield equation ( 4.5 ).

$$F_{j\to i} = \sum_{g'}\sum_{g} F_{g',j\to g,i}\,\chi_{j,g'} \qquad (4.5)$$

Then expand $F_{g',j\to g,i}$ by equation ( 3.11 ) and ( 3.12 ), equation ( 4.5 ) becomes equation ( 4.6 ).

$$F_{j\to i} = \sum_{g'}\sum_{g}\int_{g^{lower}}^{g^{upper}}\int_{V_i}\int_{4\pi}\int_{V_j}\int_{g'^{lower}}^{g'^{upper}}\int_{4\pi}\left(\sum_i N_i(\boldsymbol{r})\sum_x K_{i,x}(E^\gamma,\boldsymbol{r})\right)G\big(\boldsymbol{r_0}\to\boldsymbol{r},\boldsymbol{\Omega_0}\to\boldsymbol{\Omega},E_0^\gamma\to E^\gamma\big)\frac{Q(\boldsymbol{r_0},E_0^\gamma)}{Q_{g',j}}\,d\Omega_0\,dE_0^\gamma\,dr_0\,d\Omega dr dE^\gamma\,\chi_{j,g'} \qquad (4.6)$$

Finally, applying $\sum_g\int_{g^{lower}}^{g^{upper}}(\cdot)dE^\gamma = \int_0^\infty(\cdot)dE^\gamma$ and equation ( 4.3 ), equation ( 4.7 ) can be obtained.

$$F_{j\to i}=\frac{1}{Q_j}\int_0^{\infty}\int_{V_i}\int_{4\pi}\int_{V_j}\int_0^{\infty}\int_{4\pi}\left(\sum_i N_i(\boldsymbol{r})\sum_x K_{i,x}(E^{\gamma},\boldsymbol{r})\right)G\left(\boldsymbol{r_0}\to\boldsymbol{r},\boldsymbol{\Omega_0}\to\boldsymbol{\Omega},E_0^{\gamma}\to E^{\gamma}\right)Q\left(\boldsymbol{r_0},E_0^{\gamma}\right)d\Omega_0\,dE_0^{\gamma}\,dr_0\,d\Omega dr dE^{\gamma} \quad (4.7)$$

Note that, again, $(n,\gamma)$ source terms $Q\left(\boldsymbol{r_0},E_0^{\gamma}\right)$ and $Q_{g',j}$ are simplified notations of $Q^{n\gamma}\left(\boldsymbol{r_0},E_0^{\gamma}\right)$ and $Q_{g',j}^{n\gamma}$. $F_{j\to i}$ is "the total heat deposition in target cell *i* induced by unit gamma source in cell *j*". Similar to the generation of $F_{g',j\to g,i}$, to obtain the value of $F_{j\to i}$, just place a unit source in cell *j*, execute the fixed source run on the whole problem domain, and tally the energy deposition in cell *i* which will be the value of $F_{j\to i}$. The spectrum for the unit source, $\chi_{j,g'}$, should be a typical spectrum. For example, $(n,\gamma)$ source induced by neutron flux in cell *j* after the first few neutron iterations. $F_{j\to i}$ is used to calculate the total heat deposition from total source intensity through matrix-vector multiplication scheme given in equation ( 4.4 ) and expanded as equation ( 4.8 ).

$$\begin{bmatrix}D_{i1}\\D_{i2}\\D_{i3}\\\vdots\\D_{iN}\end{bmatrix}=\begin{bmatrix}F_{j1\to i1}&F_{j2\to i1}&F_{j3\to i1}&\cdots&F_{jN\to i1}\\F_{j1\to i2}&F_{j2\to i2}&F_{j3\to i2}&\cdots&F_{jN\to i2}\\F_{j1\to i3}&F_{j2\to i3}&F_{j3\to i3}&\cdots&F_{jN\to i3}\\\vdots&\vdots&\vdots&\ddots&\vdots\\F_{j1\to iN}&F_{j2\to iN}&F_{j3\to iN}&\cdots&F_{jN\to iN}\end{bmatrix}\begin{bmatrix}Q_{j1}\\Q_{j2}\\Q_{j3}\\\vdots\\Q_{jN}\end{bmatrix} \quad (4.8)$$

To generate the full $F_{j\to i}$ GDM, fixed source runs will be repeated with unit sources in each cell *j*, so there are a total of N fixed source runs to be executed. Within each of the runs, there are N values to be tallied and stored.

As a result, the GDM is reduced from the *N*N*G'* matrix $F_{gg',j\to i}$ to the *N*N* matrix $F_{j\to i}$ and the complexity of the matrix-vector multiplication scheme is reduced accordingly. This reduction is visualized in Table 4-2 below. The energy dependence of the GDM has been removed, reducing the dependence of the GDM on only the source and target spatial cells. In the next chapter, approaches to reduce the spatial complexity of the GDM will be discussed.

Table 4-2 Neglecting Source Spectral Dependence

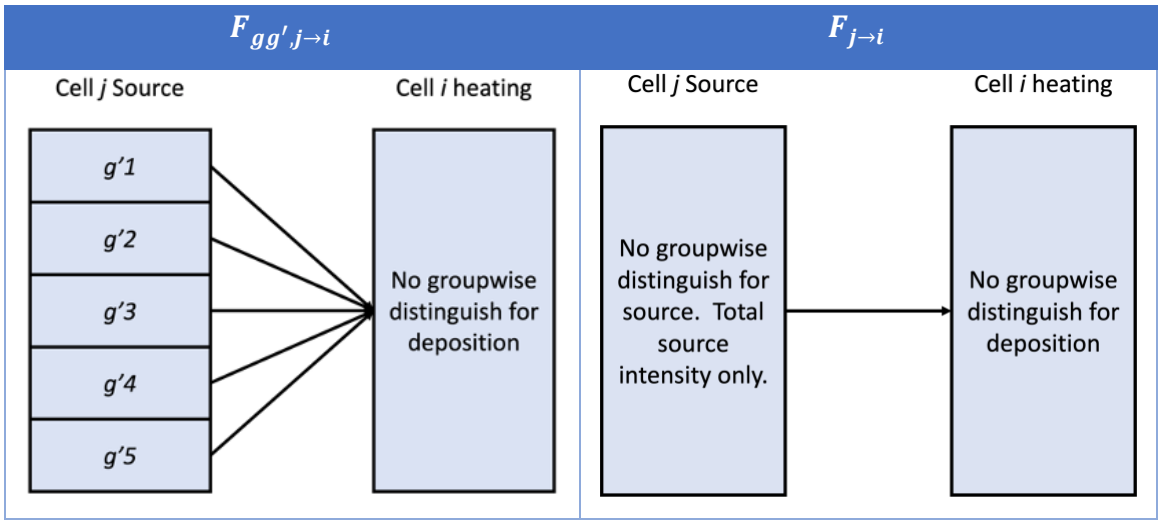

# Chapter 5
# Spatially Reduced GDM

Although getting rid of the energy dependence of GDM as discussed in Chapter 4 can reduce the matrix size significantly, generating and storing the full N by N matrix for cases with big N can still be expensive. For example, VERA Progression Problem 5a-2d [2] has 193 assemblies and each assembly has 289 pin cells. If the GDM method is applied to this problem, there would be 55777 fixed source runs and, more importantly, each of them will have been executed on the whole problem domain. To make the GDM method more applicable for big cases, several simplifications and approximations are applied to the GDM method to reduce the matrix generation time, memory storage, and execution time to perform the matrix-vector multiplication calculations.

## 5.1. Geometric Symmetry

For typical LWRs, there is a lot of symmetry in the configurations that are analyzed. For example, most LWRs are quadruple or even octantal symmetric. Such geometric similarities make it possible to eliminate a lot of redundant matrix generations runs.

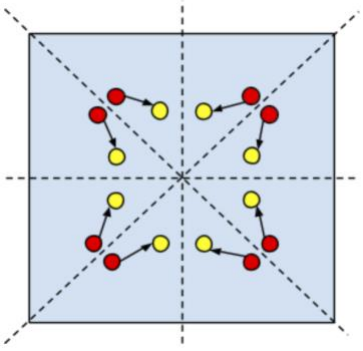

Figure 5-1 Symmetric Similarity. Green's Functions of the 8 Arrows are Identical

As shown in Figure 5-1, for problems with octantal symmetry, the 8 Green's functions are identical. Once one of them is computed, the same value can be used for the other seven arrows. As a result, the number of matrix generation runs as well as storage for the matrix can be reduced by a factor of 8 approximately. Specifically, only matrix generation fixed source runs whose sources are located within the yellow triangle in Figure 5-2 need to be executed.

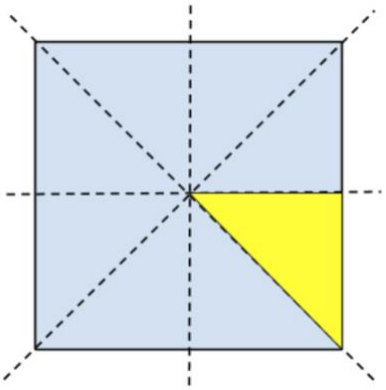

Figure 5-2 Source Locations of Matrix Generation Runs That Should be Performed

## 5.2. Reducing the Spatial Range of Interaction: Subdomain Method

### 5.2.1. Ignoring Low Value Matrix Entries

Physically, the matrix element $F_{j\to i}$ would approach 0 when source cell $j$ and target cell $i$ are far away from each other. Figure 2-3 in Section 2.3.1 shows this tendency clearly: deposition in pin cells 6 pins away from the source pin is only about 1% of the deposition in the source pin, and it can be even lower in more distant pins. Axially, Figure 2-6 shows that deposition could drop to 1% in the target axial mesh that is 2 axial levels away from the source mesh, given a typical axial mesh size.

Another investigation is done using MCNP on the same case CASL Vera Progression Problem 2h as shown in Figure 5-3. A fixed gamma source is placed at pin cell with coordinate (3, 2, 0) marked as 'S'. Gamma flux in pin cell (3, 2, 0) and (3, 7, 0) are tallied and the results are shown in Figure 5-4.

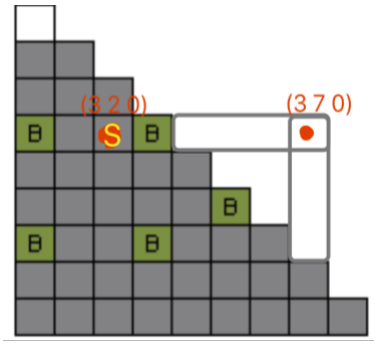


Figure 5-3 Octant Plot of CASL Problem 2h

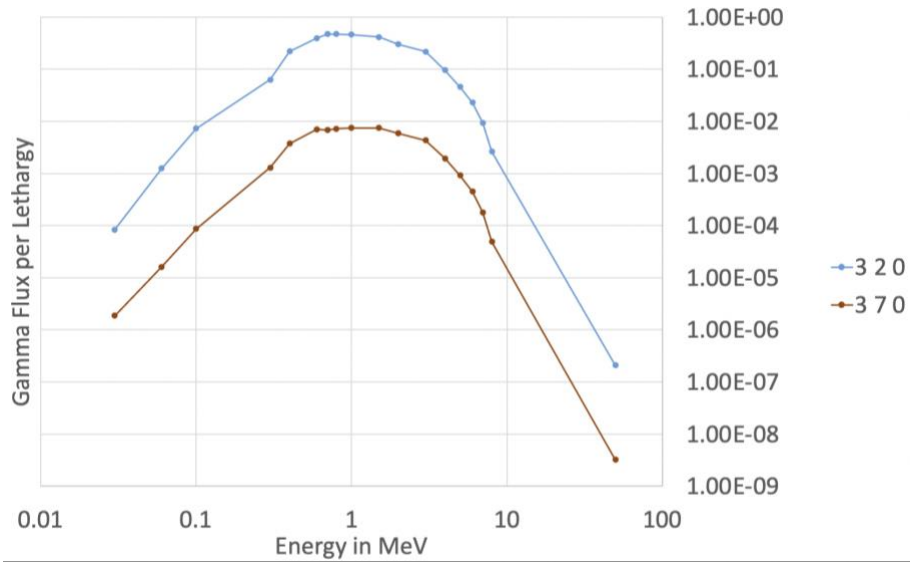


Figure 5-4 Gamma Flux at Pin Location (3, 2, 0) and (3, 7, 0)

One can see that, at pin (3, 7, 0), which is 5 pins away from the source pin, the magnitude of gamma flux drops by a factor of approximately 60 compared to the source pin. Furthermore, although the magnitude of gamma flux drops significantly through attenuation, the attenuation is approximately the same for each gamma energy group, showing again that the gamma spectrum does not change much over its trajectory even though there are both fuel pins and $B_4C$ control rod pins along the path from (3, 2, 0) to (3, 7, 0). These similar spectra indicate that heat deposition in pin cell (3, 7, 0) should also be ~1/60 of that in the source cell (3, 2, 0).

Given this level of gamma attenuations, it is reasonable to set $F_{j\to i}$ to 0 instead of explicitly calculating $F_{j\to i}$ for target cell $i$'s that are outside a given range from a source cell $j$. As a result, a matrix generation run is only needed to be executed on a small square region instead of the whole problem domain. Each of these small square regions is defined as a "subdomain", and Figure 5-5 illustrates some subdomain examples. The squares are the subdomain regions for the matrix generation runs and the triangles of corresponding colors are the source cell locations.

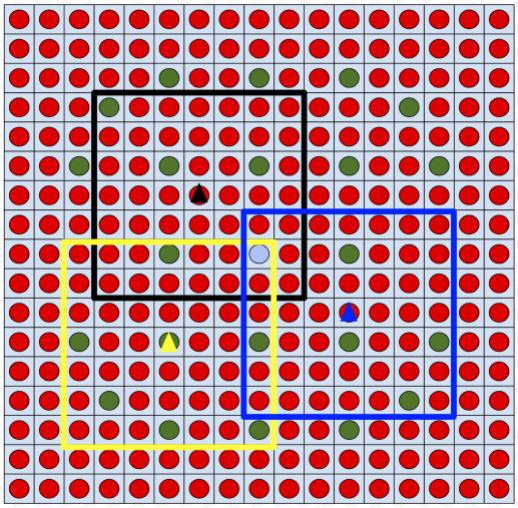

Figure 5-5 Subdomain Method

To quantify the energy deposition within a subdomain as a function of subdomain sizes, calculations were done using MCNP6 on a modified version of CASL VERA Progression Problem 4a-2d [2] with vacuum boundary conditions. Figure 5-6 is a quarter plot of the 4a-2d configuration with the 8 triangles showing the source locations for 8 different fixed source runs. Note that for this verification case, the transport calculations are not performed with subdomain-sized cases. Instead, each of the 8 fixed source runs is still done on the whole problem domain and heat deposition values in the 1x1(source pin itself), 3x3, 5x5, etc. subdomain regions centered at the source pin are computed. Also note that the fixed gamma sources used for these 8 runs are identical.

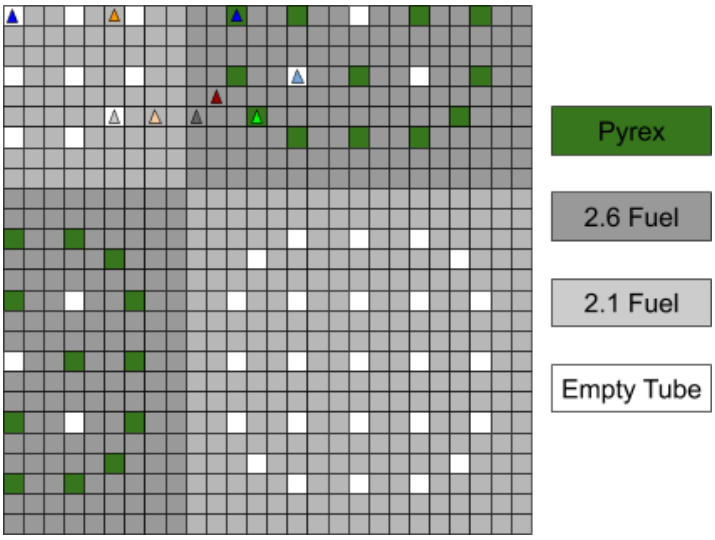


Figure 5-6 Quarter Plot of CASL VERA Progression Problem 4a-2d with Vacuum Boundary Conditions

Results are shown in Figure 5-7. The x-axis is the number of pins in one dimension (e.g. 7 means a 7x7 box centered at the source pin) and the y-axis is the ratio of the energy deposited in the subdomain to the total energy released by the source. The 8 plots correspond to the 8 fixed source runs with the legend showing the source pin location. Uppercase 'X' and 'Y' indicate the coordinate of the assembly in which the source pin is located with (X, Y) = (0, 0) refers to the central assembly, and lowercase 'x' and 'y' give the location of the source pin within that assembly with, (x, y) = (0, 0) referring to the central pin. As shown in the plot, generally 90% of the energy is deposited within a 15x15 subdomains. Furthermore, one can see that, the deposition values are location-dependent for small subdomains due to the heterogeneous assembly design. For example, a 3x3 subdomain consisting of 9 fuel pins would have more energy deposited than a 3x3 subdomain with 8 fuel pins and 1 guide tube pin. However, depositions tend to equalize after subdomain size 17x17 regardless of the source pin locations because, for large subdomains, fuel pins are dominate and the subdomain regions are less heterogeneous. For example, if a 17x17 subdomain is used, neglecting $F_{j\to i}$ outside the subdomains would underestimate the heat deposition by less than 10%. As mentioned in Section 1.1, since gammas account for only about 10% of total energy release in LWRs, this is a reasonable approximation, especially since the energy that is "lost" is actually put back into the lattice as will be described later.

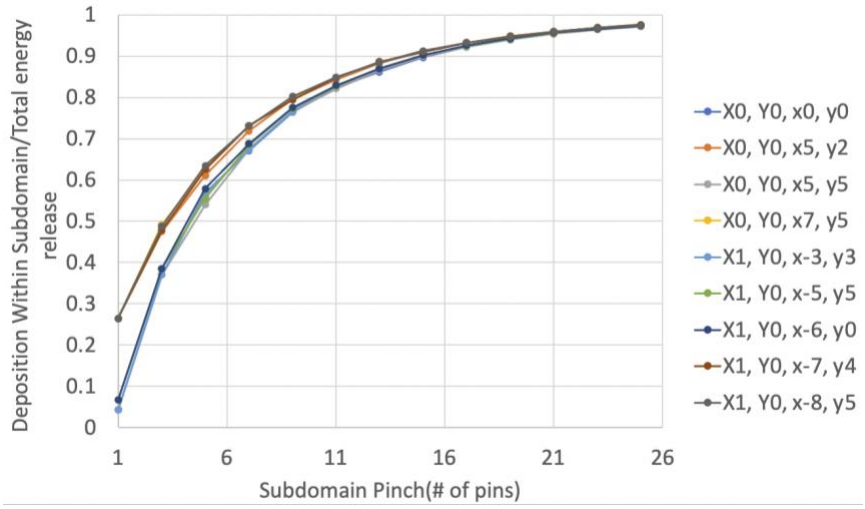


Figure 5-7 Modified 4a-2d: Deposition vs Subdomain Size

When the matrix generation transport calculations are executed on subdomain regions, vacuum boundaries will be used for these subdomains because it will be shown that the probability of gammas returning to the subdomain is very small. The investigation is again done on the same CASL Progression Problem 4a-2d as analyze above, with vacuum boundary conditions. A fixed gamma source is placed at the central pin of the central assembly, transport calculation is done on the whole problem domain, and energy leakages on 1x1, 3x3, 5x5, … 17x17 square surfaces, shown as yellow boxes in Figure 5-8, are tallied. To compute the probability of gammas returning to the given region, the outgoing energy and incoming energy for each of these surfaces are tallied separately.

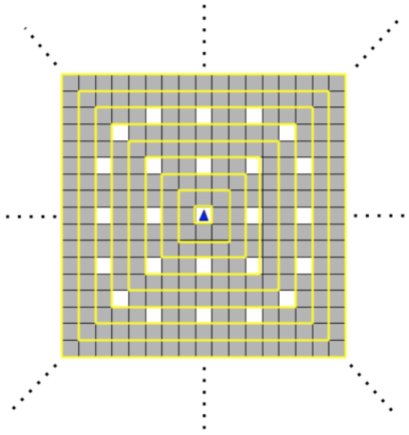

Figure 5-8 Surfaces for Energy Leakage Tallies

Figure 5-9 plots (energy coming back) / (source energy) as a function of subdomain sizes. As one can see, energy comeback drops very fast and it reaches 0.1% of the energy released by the source for a 17x17 subdomain. Such low returning rate indicates the feasibility to use vacuum boundary for matrix generation runs on subdomains.

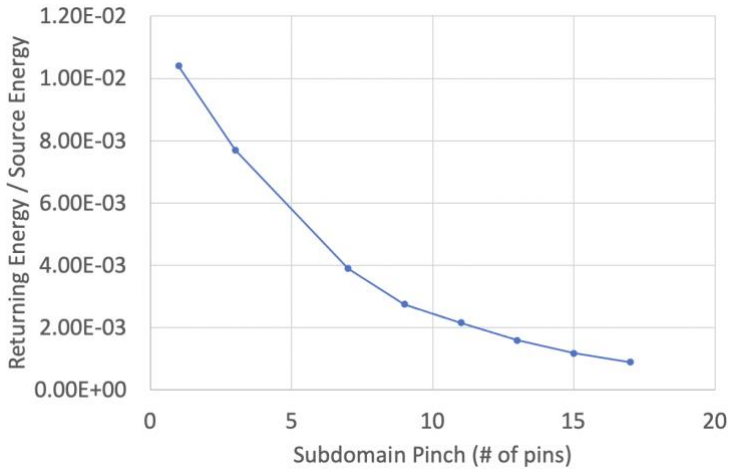


Figure 5-9 Modified 4a-2d: Returning Gamma Energy / Source Gamma Energy for Different Subdomain Sizes

In summary, as $F_{j\to i}$ becomes negligible for target cell *i*'s far away from the source cell *j*, it is only necessary to calculate nontrivial $F_{j\to i}$'s in a subdomain around the source cell *j*. This is done by executing the transport calculation and tallying the heat deposition on the subdomain with vacuum boundary conditions instead of solving the whole problem domain. With this simplification, the matrix size will be reduced from *N***N* to approximately *N**(subdomain size) and corresponding matrix generation time and matrix multiplication time are also optimized. The reason why it is approximately *N**(subdomain size) instead of exactly *N**(subdomain size) is that when a source approaches the problem boundary, the subdomain boundary will intersect with the problem boundary and thus the number of pins to be tallied is different from a fixed source run at the center of the problem. This will be explained in detail in Section 5.2.3.

### 5.2.2. Approximations for Middle Value Matrix Entries: Secondary Domain

The subdomain can be further simplified. Although deposition in pins far from the source location but within the subdomain is not negligible like deposition outside the subdomain, it is still significantly less important than deposition in pins close to the source pin. Such regions with a middle level of heat deposition (low level refers to deposition outside of the subdomain region) is defined as "secondary" domain. Correspondingly, regions closer to the source pin with higher deposition belong to the "primary" domain. The primary domain and secondary domain of the subdomain are shown on Figure 5-10, where the yellow triangle is the source pin cell of the fixed source matrix generation run, the blue region is the primary domain and the gray region is the secondary domain. Transport calculations for the matrix generation run are performed on the whole subdomain and heat deposition in each pin in the primary domain is tallied explicitly. However, since deposition in the secondary domain pins is relatively low, approximations can be applied to their calculation to optimize memory storage and generation speed. In this section, two different approaches to estimate the heat deposition in pins in the secondary domain will be introduced. One is named as "leakage-based approximation", and the other is called "segment-based approximation".

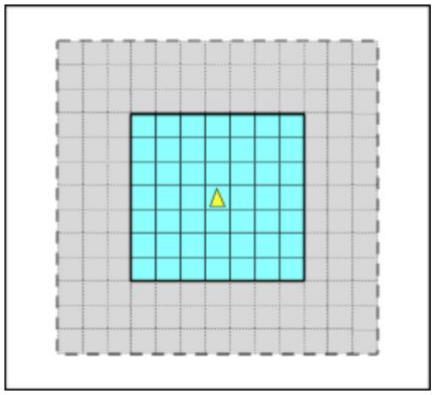

Figure 5-10 Primary (Blue) and Secondary (Grey) Domain

Before talking about the two approximation approaches, a new term "n x n ring" will be defined for ease of description. A "n x n ring" means the region consisting of the outermost pins of a n x n block. For example, the blue region in Figure 5-11 is a 7x7 ring.

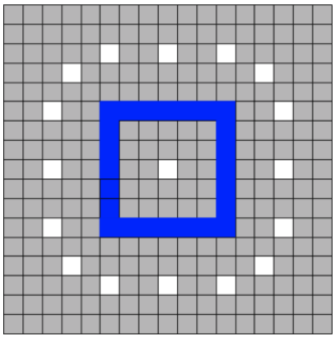

Figure 5-11 7x7 Ring

The two approaches share the same first step. The secondary domain will be split as several such rings. For instance, if the subdomains for matrix generation runs are chosen to be 23x23 and the primary domains are chosen to be 17x17, the secondary domain will be split as 19x19, 21x21 and 23x23 rings. Figure 5-12 shows the total gamma deposition in each of the n x n rings as a function of n at different locations for vacuum boundary VERA Progression Problem 4a-2d. Just as Figure 5-7, different plots in Figure 5-12 are correspond to fixed source runs with different sources and the legend indicates the location of the source pin. From Figure 5-12, it can be concluded that heat deposition in these 3 rings is very small, which again shows that there is no need for pins in these rings to be as accurate as pins in the primary domain.

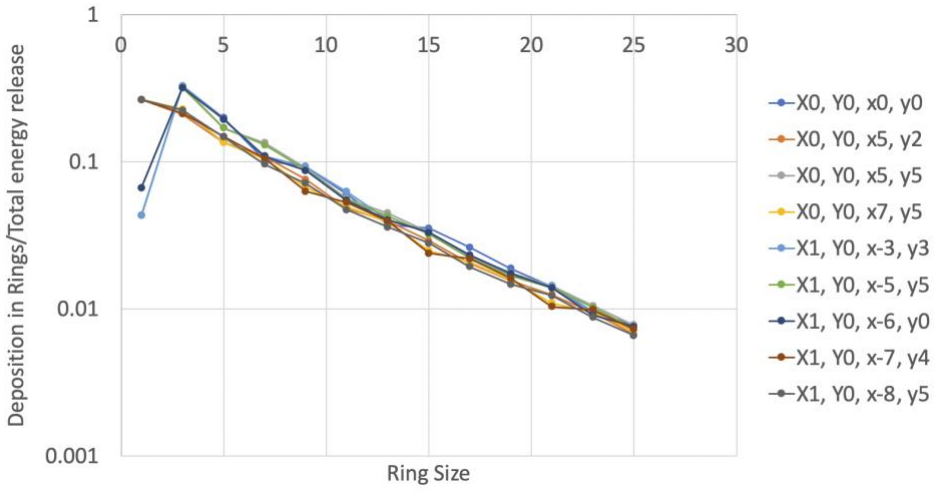


Figure 5-12 Modified 4a-2d: Total Deposition in Outermost Pins of Subdomain Regions vs Subdomain Sizes

Then the two approaches calculate heat deposition in the secondary domain rings through different methods. The "leakage-based approximation" treats the 4 sides of the rings separately with each side represented as a trapezoid as shown in Figure 5-13. The corner pins are split diagonally and each half is taken care of by the trapezoid of the corresponding side.

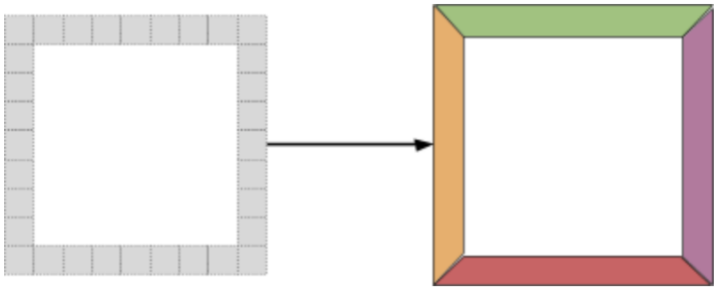

Figure 5-13 Leakage-based Approximation for Secondary Domain Rings

For each trapezoid, heat deposition is calculated through boundary leakages. Net energy leakage on the top and bottom sides are tallied separately as shown in Figure 5-14. Note that "top" and "bottom" are relative to the direction of the trapezoid itself, not the whole ring. For example, in Figure 5-13, the "bottom" of the left (orange) trapezoid is the left outer boundary of the ring. Physically, the net leakage on the top base is going into the trapezoid and that on the bottom base is leaking out because the fixed gamma source is inside the ring. As a result, total heat deposition in this trapezoid can be approximated as $E_{in} - E_{out}$. This is approximate because leakages on the diagonal sides are not tallied but these are small due to symmetry as well as the short lengths compared to the horizonal surfaces.

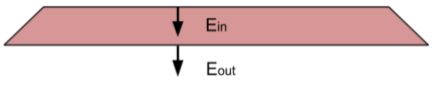


Figure 5-14 Energy Leakage Tally for Leakage-based Approximation Approach

Next, total heat distribution in the trapezoidal side blocks will be redistributed to pins belong to the blocks. The most basic scheme would be to evenly redistribute the total deposition to the pins. For example, the trapezoid in Figure 5-15 has 7 whole pins and 2

half pins, and thus heat deposition in each whole pin would be $(E_{in} - E_{out})/8$ and that in a half pin would be $(E_{in} - E_{out})/16$. Because a half pin is a part of a corner pin in its ring, it means contribution to that corner pin by this side trapezoid is $(E_{in} - E_{out})/16$. The other part of this corner pin is contributed by the other side trapezoid and, if the incoming and leaking out energy values of that trapezoid are $E_{in}'$ and $E_{out}'$ respectively, the total heat deposition in the corner pin with contributions from both sides would be $(E_{in} + E_{in}' - E_{out} - E_{out}')/16$.

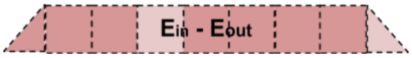


Figure 5-15 Leakage-based Approximation: Trapezoid to Pin Redistribution

To improve the redistribution scheme, additional correction factors would be applied to non-fuel pins like control rods, insertions or guide tubes because non-fuel pins usually get considerably less gamma deposition compared to fuel pins. A non-fuel pin correction factor is defined as the ratio of heat deposition in the whole non-fuel pin to that in a whole fuel pin in the same trapezoid. For example, if the lighter red pins in Figure 5-15 are non-fuel pins with correction factor equals to 0.2, the total weight for this trapezoid will be (1*number of whole fuel pins+0.5*number of half fuel pins+0.2*number of whole non-fuel pins+0.5*0.2*number of half non-fuel pins=) 6.8, which means deposition would be $(E_{in} - E_{out})/6.8$ for each whole fuel pin, $(E_{in} - E_{out})/6.8/2$ for the half fuel pin, $0.2 * (E_{in} - E_{out})/6.8$ for the whole non-fuel pin and $0.2 * (E_{in} - E_{out})/6.8/2$ for the half non-fuel pin.

A gamma smearing model was recently developed in MPACT by Y. Liu et al. [7]. The gamma smearing model redistributed gamma energy release to a predefined block of 7x7 pin cells and deposition in each pin cell is based on the isotope atomic number Z in that pin, because gamma interaction cross sections are proportional to a power of Z, or equivalently number of electrons, according to Knoll [25]. Photoelectric, Compton scattering, and pair production cross sections are proportional to $Z^{4-5}$, Z and $Z^2$ respectively, and the power was empirically selected to be 1.6, which is a reasonable

approximation because Compton scattering is the dominate gamma reaction in reactors. In other words, gamma deposition is proportional to $(\text{number of electrons})^{1.6}$ in the pin cell. The exponent 1.6 was shown to work very well for the gamma smearing model. In this work, the $Z^{1.6}$ factor is used as the non-fuel pin correction factors for secondary domain energy redistribution. The relative $Z^{1.6}$ values, $\frac{(\text{number of electrons in a pin})^{1.6}}{(\text{number of electrons in a U21 pin})^{1.6}}$, of different pin cell types in VERA Progression Problem 4a-2d are on the second column of Table 5-1.

Table 5-1 Non-fuel Pin Correction Factor vs Authentic Tallied Heating

| Pin Type | Relative (Number of e)^1.6 | Relative Tallied Heating |
|---|---|---|
| **U21** | 1.000 | 1.000 |
| **U26** | 1.000 | 0.991 |
| **Pyrex** | 0.437 | 0.427 |
| **Guide Tube** | 0.320 | 0.284 |

The third column of Table 5-1 shows the relative actual gamma deposition of different types of pins when they are given similar gamma fluxes of secondary domain intensity level. These deposition values are tallied through fixed source runs on problem 4a-2d as shown in Figure 5-16. First, a fixed gamma source is placed in the pin indicated by the light blue triangle, and deposition in the Pyrex insertion pin and 2.6% fuel pin indicated by the blue arrows are tallied. Next, the same source is placed in the white triangle location and depositions in the 2.1% fuel pin and guide tube pin are tallied. The 4 target pins are equally distant from the gamma sources and the paths from the sources to the pins are similar. Also, the source-to-pin distances are the same as source-to-secondary-domain distances in matrix generation runs. This setup ensures that the verification runs duplicate an authentic secondary domain environment. Also, the comparison between the relative tallied heat deposition and relative $(\text{number of electrons in a pin})^{1.6}$ shows that the electron quantity-based factors have excellent agreement with the tallied heat deposition. The factor in guide tube pins is a little bit off but overall it is about the same level as the tallied heat deposition in empty guide tubes.

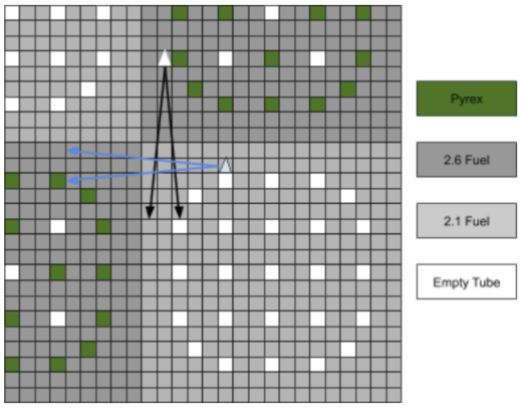


Figure 5-16 Fixed Source Runs to Verify Non-fuel Pin Correction Factors

The second approach, the segment-based approximation, treats the four sides of a ring as four rectangles as depicted Figure 5-17. Different from the leakage-based approximation, each of the corner pins is given to one of the rectangles as a whole in the segment-based approximation. As shown in Figure 5-17, the top-left and bottom-left pins are in the left rectangle (yellow), top-right pin is in the top rectangle (green) and bottom-right pin is in the bottom rectangle (red).

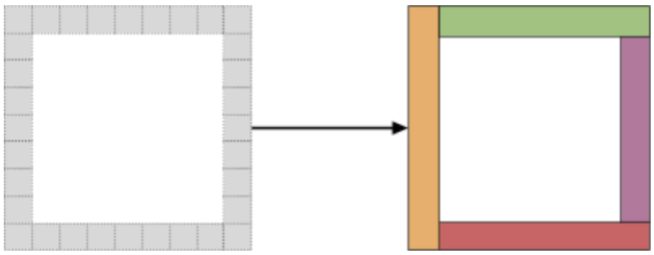

Figure 5-17 Segment-based Approximation for Secondary Domain Rings

For each side, unlike leakage-based approximation's trapezoid whose total heat deposition is estimated through leakage tallies on the two bases, total heat deposition in the rectangular segment is tallied or calculated directly. Then total heat deposition in a segment is redistributed evenly to the pins belong to it except with some non-fuel pin correction factors applied. This redistribution step is similar to how the redistribution is done for the side trapezoids in the leakage-based approximation approach without the complexities and approximations with the diagonally halved corner pins. For example, for a segment containing 5 fuel pins and 2 non-fuel pins and the total deposition is $E_{dep}$ as shown in

Figure 5-18, if non-fuel pin correction factors are 0.2 for both of the two non-fuel pins, the total weight would be (1*number of fuel pins+0.2*number of non-fuel pins=) 5.4. As a result, gamma heat deposition would be $E_{dep}/5.4$ in each fuel pin and $0.2 * E_{dep}/5.4$ in each non-fuel pin.


Figure 5-18 Segment-based Approximation: Rectangle to Pin Redistribution

Although the fixed source runs are still on the whole subdomain, the number of separate tallies in the secondary domain is significantly reduced. Such simplification can greatly reduce the matrix generation time in code systems whose performances are tally dependent like MCNP.

### 5.2.3. Problem Boundaries

Section 5.2.2 presented the general case for a subdomain with primary and secondary regions, and the secondary domains consist of only complete rings. However, if the source location is close to the core boundaries, the subdomain, including both the primary region and the rings of the secondary domain, will be cut by the core boundaries. For square problems, Figure 5-19 shows how subdomains are cut by one side of the core boundary when the source location is close to that side, and Figure 5-20 shows how subdomains are cut by two sides of the core boundary when the source location is close to a corner.

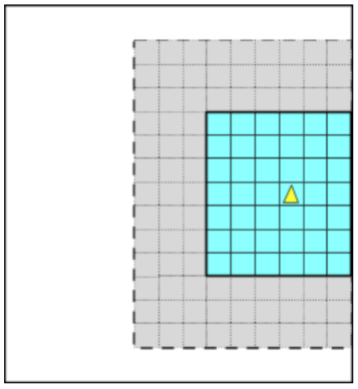

Figure 5-19 Source Location Close to One Core Boundary

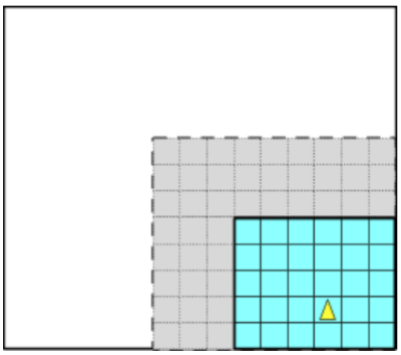

Figure 5-20 Source Location Close to a Corner of the Core

Both the leakage-based approximation and the segment-based approximation are able to calculate such incomplete secondary rings close to square core boundaries. The basic procedures are the same as those presented in Section 5.2.2, with sizes of side trapezoids/rectangles and thus number of pins for heat redistributions as the only differences. However, authentic whole core problems might have more complicated core boundary shapes. For example, the zigzag boundary of VERA Progression Problem 5a-2d [2] core as shown in Figure 5-21 represents a "re-entrant" boundary and requires additional analysis.

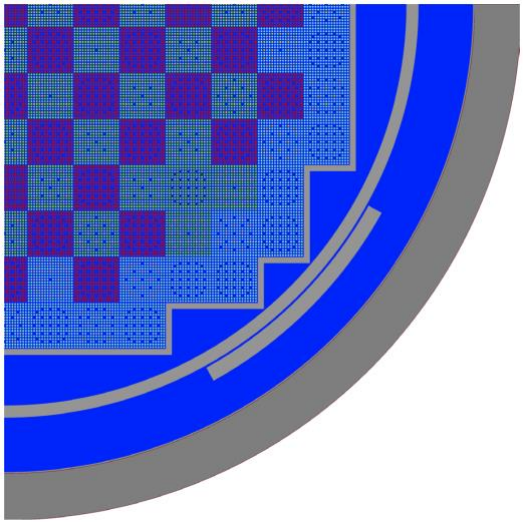

Figure 5-21 Configuration of VERA Progression Problem 5a-2d

A subdomain cut by zigzag shaped boundaries would be like the one in Figure 5-22. Note that, although the subdomain intersects with the core boundary and there is no need to tally

gamma depositions outside the core region, the transport calculation should still be performed on the whole subdomain instead of only the intersection of the core region and the subdomain. The region outside of the core region but inside the subdomain, which is the white segment next to the primary domain on the left of Figure 5-22, usually consists of core baffle, moderator, barrel, etc. Gamma depositions in these materials are insignificant, but gamma rays leaking from the core and entering this segment can enter the core region again due to the re-entrant boundary. If the white segment is treated as a void in the subdomain fixed source run, such leaking-and-reentering gamma rays will be omitted and that could have a significant effect on the accuracy.

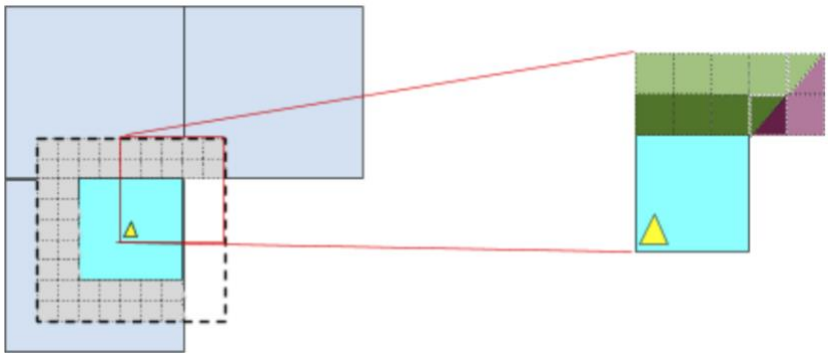

Figure 5-22 Zigzag Core Boundaries and Leakage-based Approximation Approach

The leakage-based approximation approach has significant issues with zigzag boundaries. How this approach splits the secondary domain is shown on the right of Figure 5-22. The dark purple triangle, which is essentially the right side trapezoid of the innermost secondary ring, would get a negative deposition value from the leakage-based approximation because the top base's length is 0 and thus tallied energy coming into the trapezoid (triangle) would be 0. In contrast, the segment-based approximation is compatible with zigzag boundary cores because deposition in each rectangular segment is tallied directly. As a result, the segment-based approximation is chosen as the key secondary domain approximation approach for this work due to its adaptivity and ease of implementation.

## 5.3. Energy Preservation Corrections

Although gamma deposition outside of a properly sized subdomain is very small, for example, it would be about 3% for problem 4a-2d according to Figure 5-7, completely neglecting deposition outside the subdomain violates conservation of energy. To address this error, two different energy preservation correction schemes have been developed and applied to the calculation of the GDM. The first is a simple attempt to put all energy leaking out of the subdomain, but still supposed to be deposited inside the core, evenly back to all pins outside the subdomain. The value of energy to be put back for the subdomain fixed source run with source located at pin cell *j* is obtained from matrix generation run on the whole problem domain with source at the same pin cell *j* as shown in equation ( 5.1 ).

$$\begin{aligned} &energy\ to\ be\ put\ back \\ &= (total\ energy\ deposition\ from\ fixed\ source\ run\ on\ the\ whole\ problem\ domain) \\ &- (total\ energy\ deposition\ from\ fixed\ source\ run\ on\ the\ subdomain) \end{aligned} \quad (5.1)$$

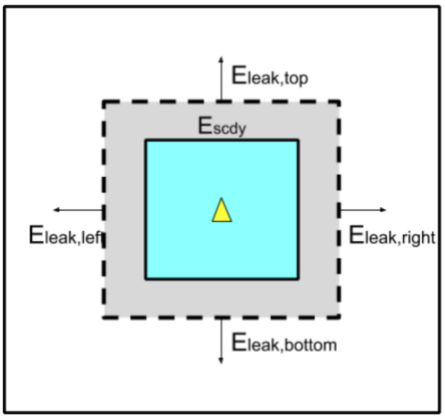


Figure 5-23 Energy Preservation for Full Subdomain

The second energy preservation correction method is based on energy leakages. First, net energy leakages on the 4 surfaces of the subdomain will be tallied. As shown in Figure 5-23, net energy leakage of the top, bottom, left and right surfaces are denoted as $E_{leak,top}$, $E_{leak,bottom}$, $E_{leak,left}$ and $E_{leak,right}$ respectively. Total deposition in the secondary

domain is $E_{scdy}$. To preserve total energy release, the leakages will be put back to the secondary domain by linearly scaling up the depositions in each of the secondary domain pins. For example, if deposition in an arbitrary cell *i* in the secondary domain is $E_i$, which is calculated from the segment-based approximation, after the energy preservation correction, the new gamma deposition value in cell *i*, $E_{i,corrected}$, becomes equation ( 5.2 ):

$$E_{i,corrected} = \frac{E_{scdy} + E_{leak,top} + E_{leak,bottom} + E_{leak,left} + E_{leak,right}}{E_{scdy}} \cdot E_i \qquad (5.2)$$

The reason why the leaked energy is put back to the secondary domain instead of the whole subdomain is that, as heat deposition in primary domain is relatively high and deposition in each pin is explicitly tallied without approximations, additional errors will be introduced if the correction method modifies the deposition values in these high-deposition and low-uncertainty pins.

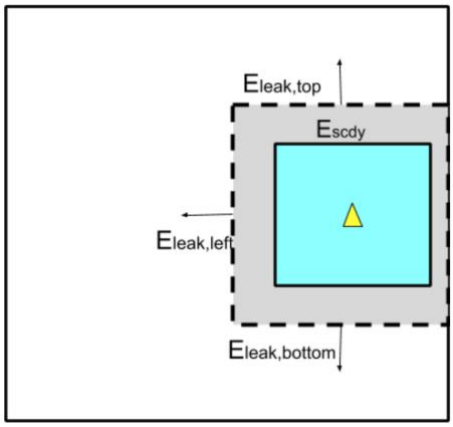


Figure 5-24 Energy Preservation for Subdomain Cut by Core Boundary

If the subdomain boundary touches or crosses the core boundary like Figure 5-24, then energy leakage on the surface touching the core boundary, which is the right surface of the subdomain in Figure 5-24, does not need to be put back because it is actually leaking out of the core region. For surfaces cut by the core boundary like the top and bottom in Figure 5-24, only energy leakage on the part of the surface inside the core region should be tallied. This scheme applies to subdomains touching or crossing zigzag core boundaries as well.

As shown in Figure 5-25, a part of the right surface of the subdomain touches the core boundary, so only energy leakage on the segment inside the core region, as shown by the red error and line, need to be put back to the subdomain to preserve total energy deposition.

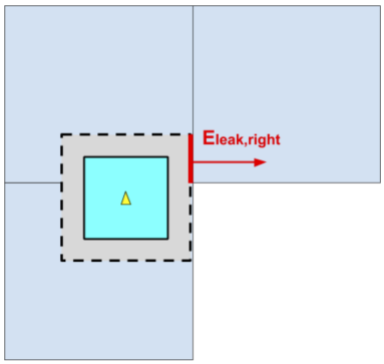


Figure 5-25 Leakage Tally on Right Side of the Subdomain for Energy Preservation on Zigzag Boundary Cores

# Chapter 6
# Numerical Results

Numerical results with GDM using different approximations will be presented in this chapter. In addition, some results using MPACT's explicit gamma transport solver will be presented. Section 6.1 will introduce how MCNP is set up and used for this work. Next, verification for the explicit gamma transport solver in MPACT will be presented in Section 6.2. Finally, verification for the GDM method with various approximations is presented in Section 6.3.

## 6.1. MCNP Model Setup

In this work, MCNP6 with ENDF.VI library is used to generate reference solutions to verify MPACT's explicit gamma transport capability. ENDF.VI library is adopted because, as mentioned in Section 2.2.1, the HELIOS library used for gamma transport calculation in MPACT is based on ENDF.VI and it was important to keep MCNP6 consistent with MPACT. In contrast, for the GDM method development and verification, MCNP6 with ENDF.VII is used to generate the GDM, since consistency with MPACT was not necessary.

### 6.1.1. MCNP Tallies

MCNP has several built-in tally capabilities [26] related to this work. This section will briefly introduce these tally cards as well as how they are used to calculate the required values.

The F1 card tallies surface current as shown in equation ( 6.1 ):

$$J = \int dE \int dt \int dA \int d\Omega \left|\hat{\Omega} \cdot \hat{n}\right| \psi(\vec{r}, \hat{\Omega}, E, t) \qquad (6.1)$$

Along with a C card, which splits F1 tallies into several cosine bins, partial currents crossing in the positive and negative directions with respect to the surface can be obtained separately as ( 6.2 ):

$$J_{\pm} = \int dE \int dt \int dA \int_{\substack{\hat{\Omega}\cdot\hat{n}>0 \\ \hat{\Omega}\cdot\hat{n}<0}} d\Omega \left|\hat{\Omega} \cdot \hat{n}\right| \psi(\vec{r}, \hat{\Omega}, E, t) \qquad (6.2)$$

The net current across the surface is $J_{net} = J_+ - J_-$. With an asterisk flag, the F1 tally will be converted into an energy tally *F1, which is the energy leakage across the surface. *F1 card is used to tally the energy leakage of the subdomain for the leakage-based energy preservation.

Next the F6 card specifies a track length estimate of energy deposition as equation ( 6.3 ):

$$H_t = \frac{\rho_a}{m} \int dE \int dt \int dV \int d\Omega \sigma_t(E) H(E) \psi(\vec{r}, \hat{\Omega}, E, t) \qquad (6.3)$$

where $H_t$ stands for total energy deposition, $\sigma_t$ is the total cross section and $\rho_a$ is atomic density. F6 can be F6:N and F6:P, which are neutron energy deposition and gamma energy deposition tallies, respectively. The heating number H(E) for the neutron energy tally is defined in equation ( 6.4 ).

$$H_n(E) = E - \sum_i p_i(E)[\bar{E}_{i,out}(E) + \bar{E}_{i,\gamma}(E) - Q_i] \qquad (6.4)$$

$p_i(E)$ = probability of reaction i at neutron incident energy E

$\bar{E}_{i,out}(E)$ = average exiting neutron energy for reaction i at neutron incident energy E

$\bar{E}_{i,\gamma}(E)$ = average exiting gamma energy for reaction i at neutron incident energy E

$Q_i$ = Q-value of reaction i

H(E) for gamma energy tally is defined in equation ( 6.5 ). By default, F6:P calculates energy deposition by both prompt and capture gammas. If the PIKMT card is used, F6:P will tally prompt gamma energy only.

$$H_\gamma(E) = E - \sum_{i=1}^{3} p_i(E)[\bar{E}_{i,out}(E)] \quad (6.5)$$

$p_i(E) =$ probability of reaction i at gamma incident energy E

$\bar{E}_{i,out}(E) =$ average exiting gamma energy for reaction i at gamma incident energy E

$i = 1 \rightarrow$ Compton scattering, $2 \rightarrow$ Pair production, $3 \rightarrow$ Photoelectric absorption

The F6 tally, especially F6:p, is used on both the verification for MPACT gamma heating calculation capability and for generation of the GDM.

Finally, the F4 card specifies a track length estimate of cell flux as shown in equation ( 6.6 ). It is used to tally gamma flux to verify MPACT's explicit gamma transport solver.

$$\bar{\phi}_V = \frac{1}{V} \int dE \int dt \int dV \int d\Omega \, \psi(\vec{r}, \hat{\Omega}, E, t) \quad (6.6)$$

Similar to the F6 card, the F4 card includes F4:N and F4:P which estimate the neutron flux and gamma flux, respectively. By default, the F4:P card calculates the sum of prompt and capture gammas, and the PIKMT card can be used along with F4:P to tally the prompt gamma flux alone.

### 6.1.2. Delayed Gammas

Gamma rays include prompt gamma, capture gammas, and delayed gammas. Prompt gammas and capture gammas can be directly tallied by MCNP's F4:P and F6:P cards, while delayed gammas cannot be estimated directly and require special attention. Since the HELIOS library contains delayed gamma production data and thus MPACT accounts for the equilibrium delayed gammas for both flux and heat deposition, delayed gammas should be added to MCNP results to be consistent with MPACT. According to Y. Liu et al [27], the spatial energy deposition as well as the spectrum of delayed gamma rays are close to those from prompt gamma rays. As a result, flux and heat deposition of delayed gammas can be scaled from the prompt gamma counterparts as shown in equation ( 6.7 ) and equation ( 6.8 ) respectively.

$$H_{\gamma d}(r) = H_{\gamma p}(r) * \frac{Q_{\gamma d}}{Q_{\gamma p}} \quad (6.7)$$

$$\phi_{\gamma d}(E, r) = \phi_{\gamma p}(E, r) * \frac{Q_{\gamma d}}{Q_{\gamma p}} \quad (6.8)$$

where $H_{\gamma d}$ and $H_{\gamma p}$ are delayed and prompt gamma heat, $\phi_{\gamma d}$ and $\phi_{\gamma p}$ are delayed and prompt gamma flux, $Q_{\gamma d}$ and $Q_{\gamma p}$ are delayed and prompt gamma energy per fission from the ENDF library respectively.

### 6.1.3. Photon Fluorescence

When a photon is incident on an electron whose binding energy is lower than the photon energy, the electron can absorb energy and jump to an excited state. Then the electron falls back to its ground state, and a photon with energy equal to the difference between these two states will be emitted. There is also another possible reaction: the photon knocks the electron out of the atom and another electron from a higher energy shell falls into the vacancy, and the amount of energy carried by the emitted photon is the difference between the binding energies of the two shells. This reaction is shown in Figure 6-1 [28].

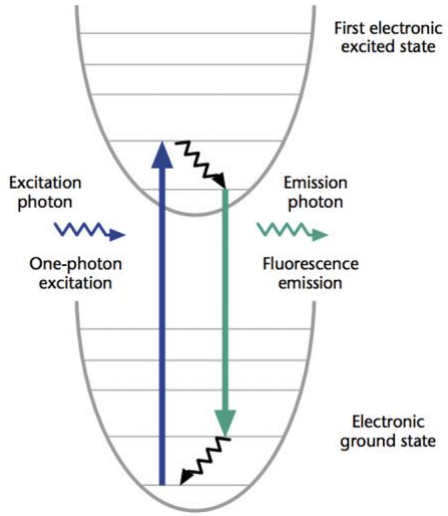


Figure 6-1 Jablonski Diagram of One-photon Excitation

This effect is called the photon fluorescent effect, and the emitted photon is the fluorescent photon. For high energy photons, electrons with the highest binding energy, which are the electrons in the innermost shell, k-shell, in an atom, are the easiest to be knocked out. The k-shell emission energy for uranium atoms is approximately 0.1 MeV [29].

The HELIOS library does not include photon fluorescence reactions, which means MPACT with the HELIOS library will underestimate the gamma flux in the energy group containing 0.1 MeV. For consistency, MCNP calculations for gamma flux distributions will be generated with the photon fluorescence effect turned off to match what is done in MPACT. However, MCNP reference calculation for gamma energy deposition will be run with this effect turned on. This is not a small effect - when fluorescence is turned off in MCNP, energy calculations are significantly impacted. For example, energy by prompt gamma released per fission for 3.1% uranium fuel, which is 6.64 MeV in MCNP6 runs, becomes 6.17 MeV when the photon fluorescence effect is turned off.

## 6.2. MPACT Explicit Gamma Transport

This section is devoted to presenting numerical results of the explicit gamma transport solver in MPACT introduced in Section 2.2. MPACT's capabilities on calculating gamma spectrum, gamma spatial distribution and gamma heat deposition are verified through various different test cases including single fuel cell, 2D assembly, 3D assembly and 2D quarter core.

### 6.2.1. Flux Spectrum

The gamma flux spectrum calculation is verified through the same simplified pin cell model as Figure 1-1 in Section 1.1. The k-effective from MPACT run is 1.17357, which is good agreement with the MCNP6 + ENDF.VI result 1.17373 ± 0.00006. Also, the neutron spectra in fuel regions calculated by both code systems agree very well as shown in Figure 6-2. Such consistency proved the correctness of both the MPACT model and the MCNP model.

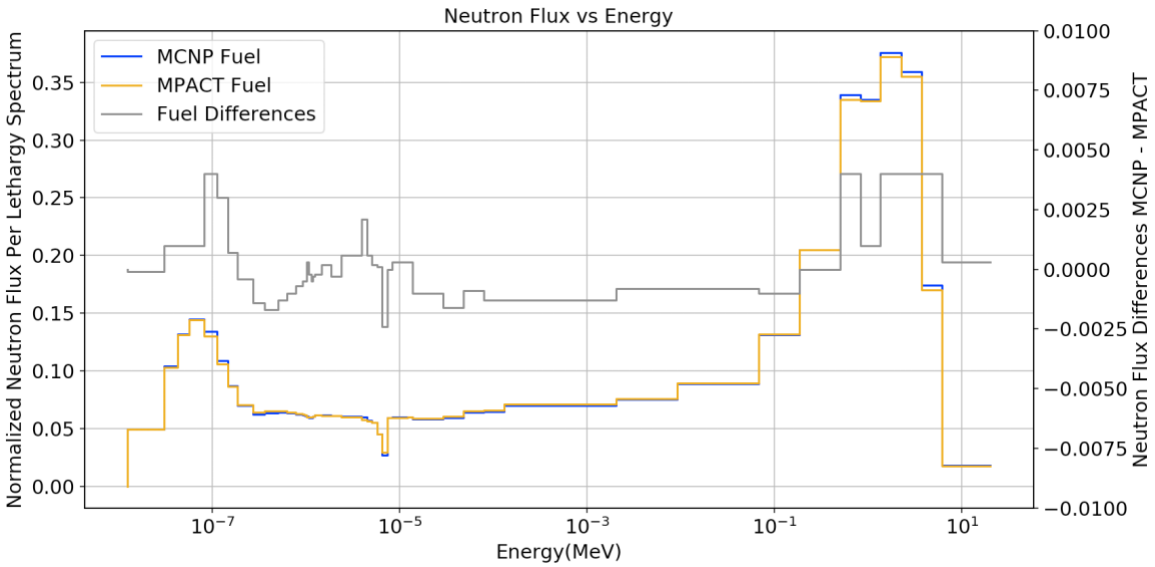


Figure 6-2 Pin Cell: Neutron Spectrum

Figure 6-3 shows the groupwise gamma flux calculated by MPACT and by MCNP with photon fluorescent effect on. Overall, the MPACT flux is close to the MCNP reference except in the 0.1 MeV group containing k-shell emission photon for both the fuel region and the moderator region. When photon fluorescent effect is turned off in MCNP, MPACT gamma spectrum shows excellent agreement with MCNP spectrum in all groups as shown in Figure 6-4. The total gamma flux is 111% of the total neutron flux value in the MPACT run and that in the MCNP run is 113%, and gamma flux plots in Figure 6-4 are normalized by the total neutron flux in the fuel region. The gray lines plot the absolute errors and one can see that the errors are < 1% in most groups. Such low error level shows the accuracy of the MPACT gamma solver for groupwise flux in pin cell problems.

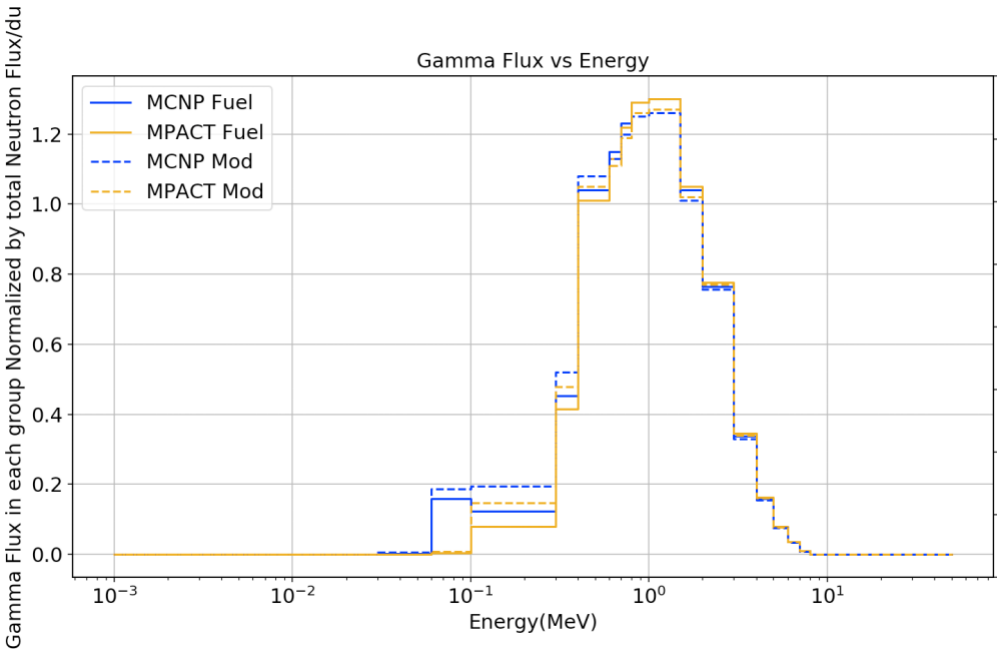


Figure 6-3 Pin Cell: Gamma Spectrum with Photon Fluorescent Effect on

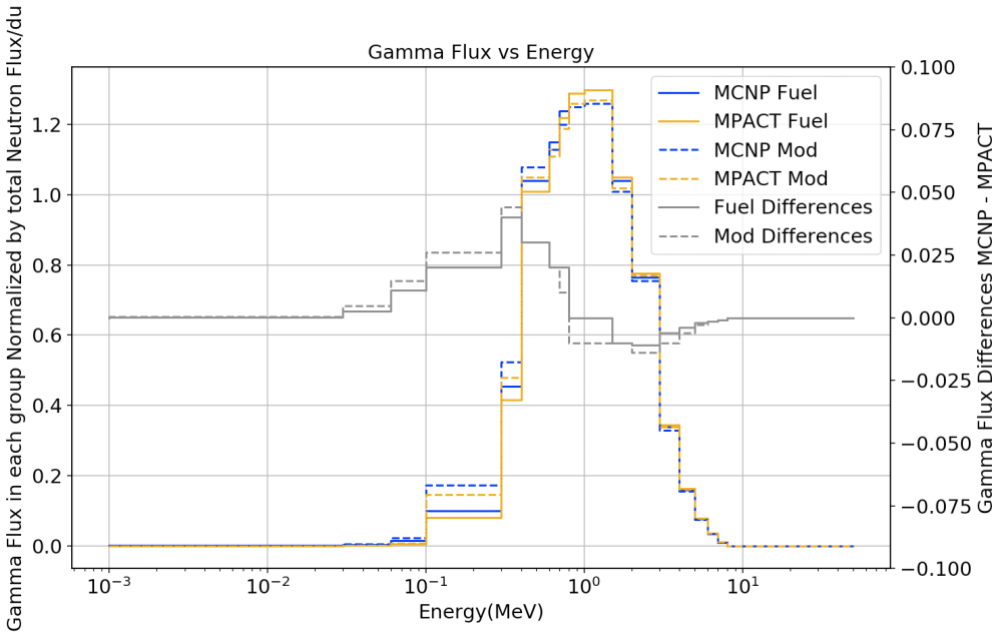


Figure 6-4 Pin Cell: Gamma Spectrum with Photon Fluorescent Effect off

### 6.2.2. Radial Flux Distribution

Verifications for radial flux distribution calculations start with 2D assembly case CASL VERA Progression Problem 2b [2]. This case contains only fuel rods and guide tubes as

shown in Figure 6-5. The k-eff calculated by MPACT is 1.16102 and that from the MCNP run is 1.16138 ± 0.00006. The validity of this model is further proved by comparing the neutron flux distributions from MCNP and MPACT. The normalized neutron flux distribution is calculated by MPACT as shown in Figure 6-6 and the comparison with MCNP is shown in Figure 6-7, which show that neutron flux differences are no more than 0.15%, verifying the model is correctly handled in both MCNP and MPACT.

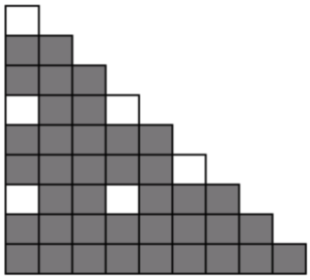

Figure 6-5 CASL Vera Progression Problem 2b Configuration

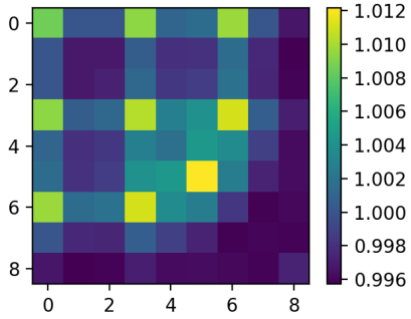


Figure 6-6 2b: Normalized Total Neutron Flux by MPACT

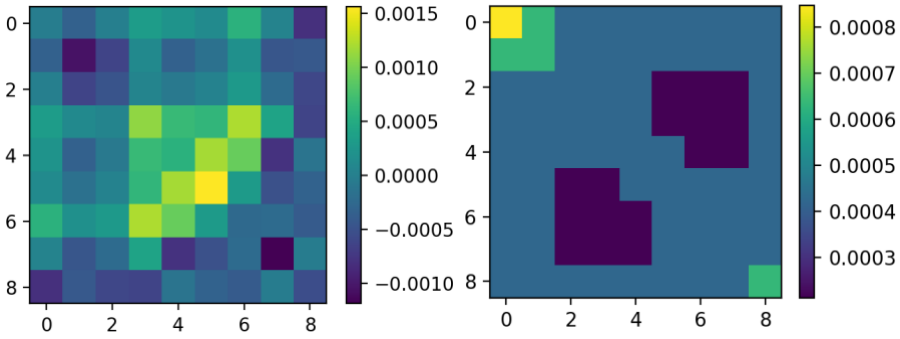


Figure 6-7 2b: Neutron Flux MCNP vs MPACT Relative Errors (Left) and MCNP Relative Uncertainty (Right)

The normalized gamma flux distribution, shown in Figure 6-8, is similar to the neutron flux distribution, with higher values in guide tubes pins and fuel pins adjacent to guide tubes. This is due to the fact that fuel regions are better gamma absorbers than moderator regions, and fuel pins adjacent to guide tubes are better gamma sources. Comparison of MCNP and MPACT results quantitatively proves the correctness of the gamma calculation, as shown in Figure 6-9, with errors less than 0.4%.

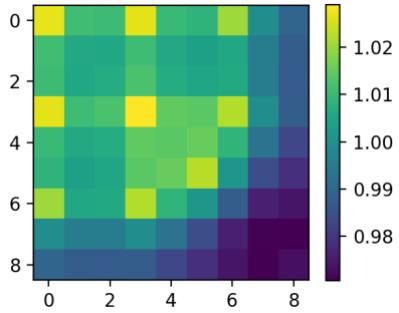


Figure 6-8 2b: Normalized Total Gamma Flux by MPACT

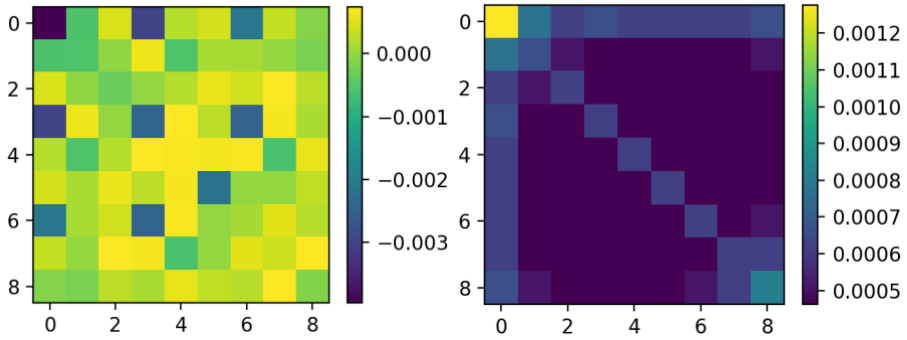


Figure 6-9 2b: Gamma Flux MCNP vs MPACT Relative Errors (Left) and MCNP Relative Uncertainty (Right)

Next, VERA Problem 2h is chosen to test the gamma transport solver performance when control rods are present. It is the same case 2h used in Section 5.2.1 and its configuration is shown on Figure 5-4. The k-eff calculated by MPACT is 0.85362 and that from the MCNP run is 0.85100 ± 0.00007. Although 262 pcm is not a trivial difference, it is found that, when the MCNP run is using ENDF.VII library, k-eff from MCNP will become 0.85322 ± 0.00007 which is much closer to the MPACT k-eff. The MPACT neutron flux distribution and comparison with the MCNP6 reference are shown in Figure 6-10 and Figure 6-11. The neutron flux is lower in control rod pins as expected, and the comparison

with MCNP6 indicates the difference to be less than 0.25% in all pins. The gamma flux distribution is shown in Figure 6-12. Unlike the neutron flux which is lower in control rod pins, the gamma flux is higher in the control rod pins than in the fuel pins. This distribution pattern can be explained by the neutron absorption reaction in B-10, where the outgoing particles are a lithium nucleus, an alpha particle and a photon. Quantitative comparison with MCNP6 further proves the accuracy of the gamma transport calculation. As shown in Figure 6-13, the maximum error is about 0.6%.

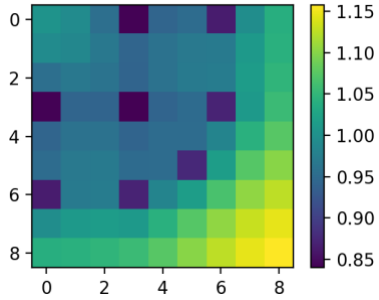


Figure 6-10 2h: Normalized Total Neutron Flux by MPACT

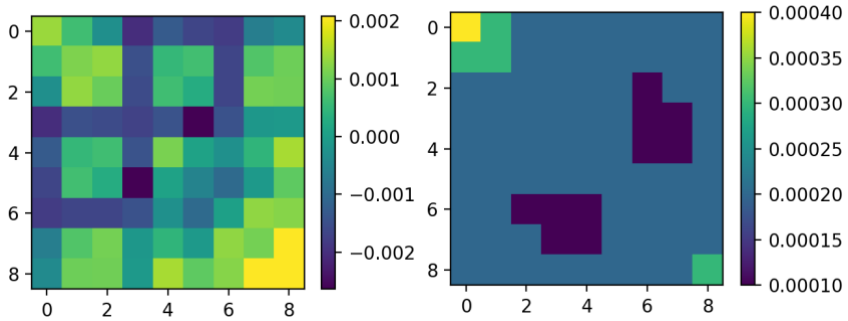


Figure 6-11 2h: Neutron Flux MCNP vs MPACT Relative Errors (Left) and MCNP Relative Uncertainty (Right)

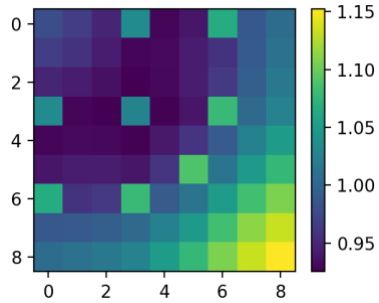


Figure 6-12 2h: Normalized Total Gamma Flux by MPACT

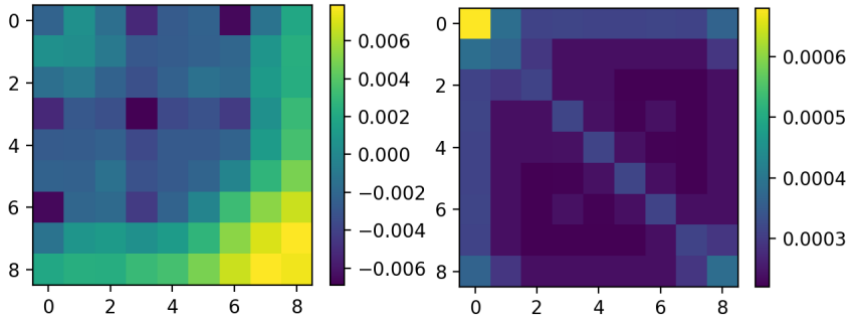


Figure 6-13 2h: Gamma Flux MCNP vs MPACT Relative Errors (Left) and MCNP Relative Uncertainty (Right)

The last 2D assembly case is CASL VERA Progression Problem 2p [2] as shown in Figure 6-14. This assembly contains gadolinia fuels as indicated by the brown 'G' marks. The purpose of this case is to investigate the performance of the solver when strong gamma sources are present. Note that the MCNP6 ENDF.VI library lacks gamma production data for gadolinium, so the ENDF.VII data is used for gadolinium when generating the MCNP reference. MPACT is still using the same ENDF.VI based HELIOS library.

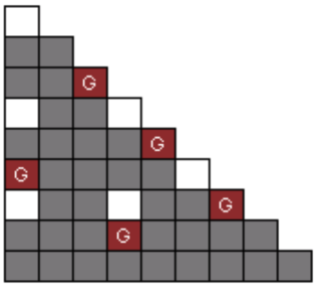


Figure 6-14 CASL Vera Progression Problem 2p Configuration

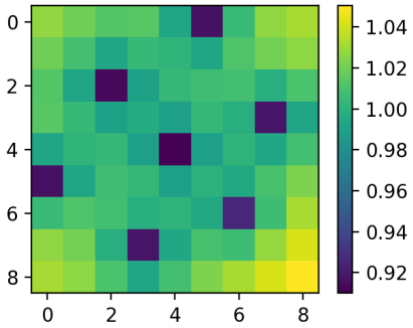


Figure 6-15 2p: Normalized Total Neutron Flux by MPACT

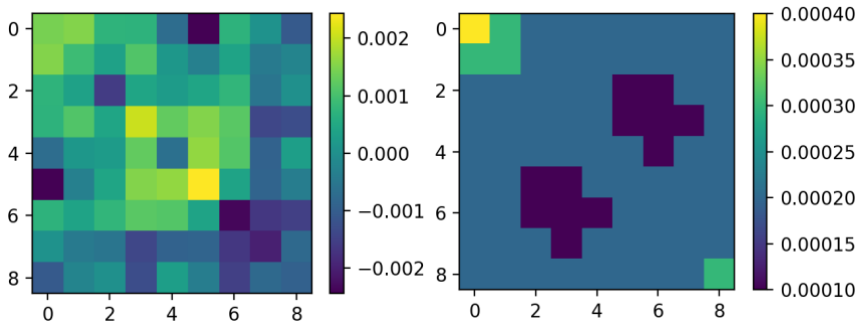


Figure 6-16 2p: Neutron Flux Relative Errors MCNP vs MPACT (Left) and MCNP Relative Uncertainty (Right)

The k-eff calculated by MPACT is 0.94860 and that from the MCNP run is 0.94793 ± 0.00007, for a difference of 67 pcm with an uncertainty of 7 pcm. This is a reasonable comparison. The neutron flux distribution calculated by MPACT is shown in Figure 6-15. One can see that neutron flux in gadolinium fuel pins is lower than other fuel pins and guide tubes as expected. Quantitative comparison with MCNP reference shows that the errors are all within 0.2%, which proves the correctness of this model. As for the gamma flux, Figure 6-17 shows that, different from neutron flux, gamma flux is noticeably higher in the gadolinium fuel pins due to the strong gamma sources in the gadolinium. Comparison with MCNP6 results is shown in Figure 6-18. Overall, the differences are within reasonable ranges. The maximum differences reach 2%, but only in the gadolinium fuel pins. This discrepancy may be due to the use of different versions of cross section libraries for gadolinium in MPACT versus MCNP6.

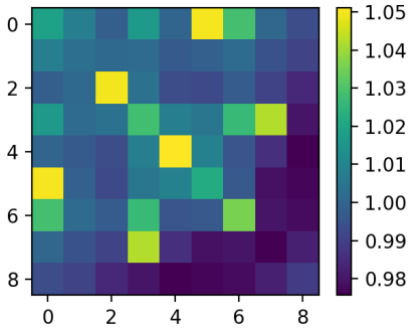


Figure 6-17 2p: Normalized Total Gamma Flux by MPACT

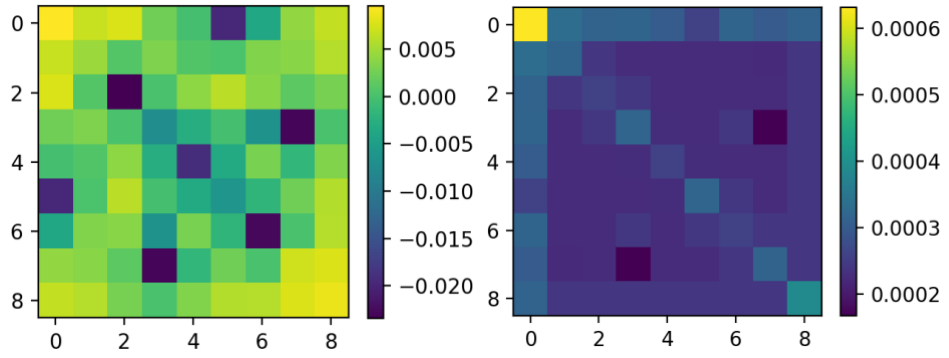


Figure 6-18 2p: Gamma Flux Relative Errors MCNP vs MPACT (Left) and MCNP Relative Uncertainty (Right)

Finally, quarter-core case VERA Progression Problem 5a-2D [2] is chosen to test pin-wise and assembly-wise gamma distributions as well as parallel performance of the gamma solver in MPACT. This case has 193 assemblies and 17x17 pins within each assembly as shown in Figure 5-21 and Figure 6-19.

| | H | G | F | E | D | C | B | A |
|---|---|---|---|---|---|---|---|---|
| 8 | 2.1 | 2.6<br>20 | 2.1 | 2.6<br>20 | 2.1 | 2.6<br>20 | 2.1 | 3.1<br>12 |
| 9 | 2.6<br>20 | 2.1 | 2.6<br>24 | 2.1 | 2.6<br>20 | 2.1 | 3.1<br>24 | 3.1 |
| 10 | 2.1 | 2.6<br>24 | 2.1 | 2.6<br>20 | 2.1 | 2.6<br>16 | 2.1 | 3.1<br>8 |
| 11 | 2.6<br>20 | 2.1 | 2.6<br>20 | 2.1 | 2.6<br>20 | 2.1 | 3.1<br>16 | 3.1 |
| 12 | 2.1 | 2.6<br>20 | 2.1 | 2.6<br>20 | 2.6 | 2.6<br>24 | 3.1 | |
| 13 | 2.6<br>20 | 2.1 | 2.6<br>16 | 2.1 | 2.6<br>24 | 3.1<br>12 | 3.1 | |
| 14 | 2.1 | 3.1<br>24 | 2.1 | 3.1<br>16 | 3.1 | 3.1 | | |
| 15 | 3.1<br>12 | 3.1 | 3.1<br>8 | 3.1 | Enrichment<br>Number of Pyrex Rods | | | |

Figure 6-19 5a-2d: Assembly Map

The total gamma flux distribution and the thermal neutron flux distribution calculated by MPACT are in Figure 6-20 and Figure 6-21, respectively. The gamma flux smearing effect is apparent when qualitatively compared with the thermal neutron flux. Such pattern suggests that gamma power distribution will be more uniform than the pin power distribution, which is an expected result. In addition, the spatial distribution is reasonable. Within a single assembly, guide tube pins have higher gamma flux and lower gamma

absorption than fuel pin, similar to the case 2b results, and the hottest (the reddest block in Figure 6-20) assembly is due to the absence of Pyrex insertions. All the qualitative analysis indicates the correctness of the gamma calculation on this quarter core case.

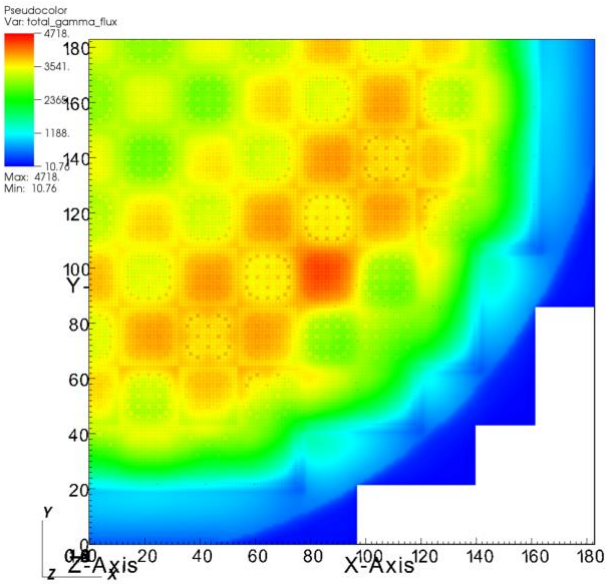


Figure 6-20 5a-2d: Total Gamma Flux

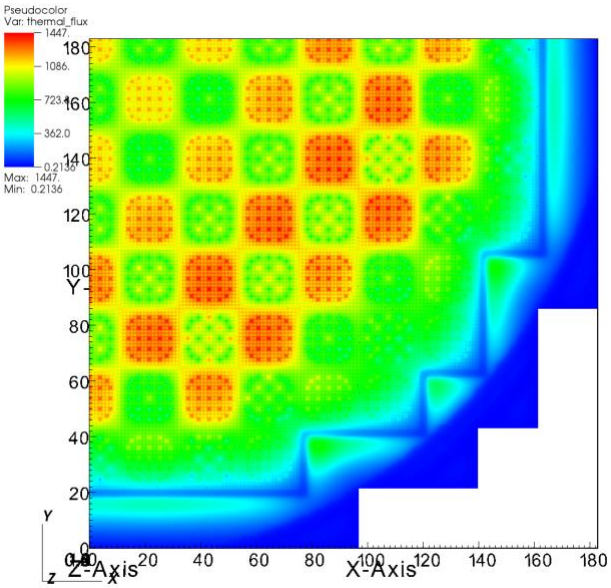


Figure 6-21 5a-2d: Thermal Neutron Flux

### 6.2.3. Axial Flux Distribution

In addition to the 2D transport solver, the 2D/1D solver in MPACT is also leveraged to do 3D gamma calculations. To test this newly developed 3D gamma transport capability, a 5×5 mini assembly case was created and named the "$B_4C$ 5x5 3D" case. The configuration is shown in Figure 6-22. The assembly has 100 cm fuel pins and a nozzle with thickness 10 cm and a plate with thickness 5 cm on each end. Radially, the core region has 20 fuel pins and 5 guide tubes. Everything is at 293K. It has vacuum boundaries on the top and bottom and reflective radial boundaries. The fuel pins are identical to those in CASL problem 2b and 2h, each with a 3.1% fuel rod with a radius of 0.4096 cm, cladding with an inner radius of 0.418 cm, and an outer radius of 0.475 cm with moderators outside. The guide tubes have an inner radius of 0.561 cm and an outer radius of 0.602 cm. A $B_4C$ control rod is inserted in the center guide tube.

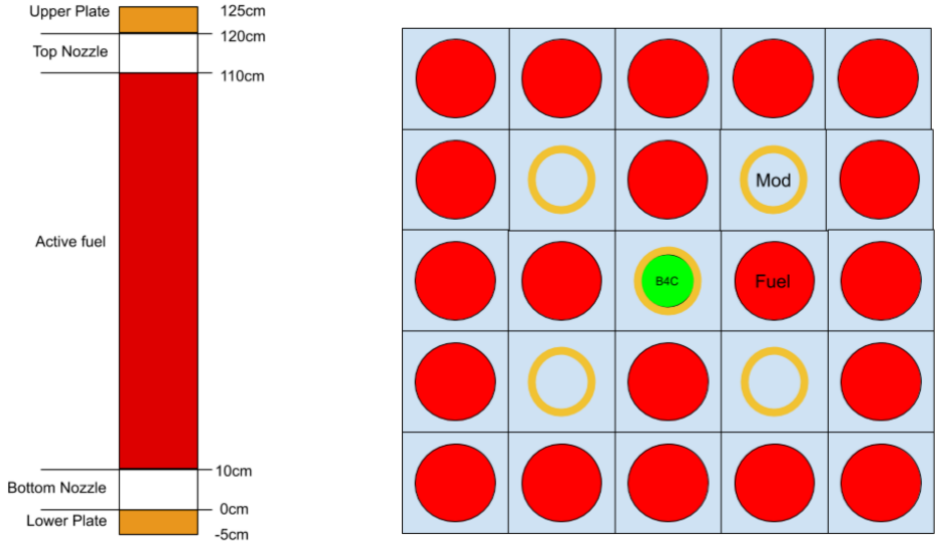


Figure 6-22 $B_4C$ 5x5 3D: Configuration Side View (Left) and Top View (Right)

The axial neutron flux and gamma flux of the $B_4C$ 5x5 3D case in which the control rod is fully inserted are shown in Figure 6-23 and Figure 6-24 respectively. Both neutron and gamma fluxes are radially integrated and presented as axial distributions. The neutron flux calculated by MPACT is consistent with that calculated by MCNP, with errors less than 1%. Such consistency verifies the effectiveness of this modeling. Gamma flux results in MPACT are consistent with the results from MCNP as most of the errors are within 1% as

well. In addition, the accuracy can be further improved by running the case with finer axial meshes and integrating the result to 10 axial levels. As shown in Figure 6-24, if the calculation is performed using 40 axial meshes and integrated into 10 meshes, the results are better compared with the results calculated using 10 axial meshes, especially for the top and bottom meshes in which the absolute flux values are low.

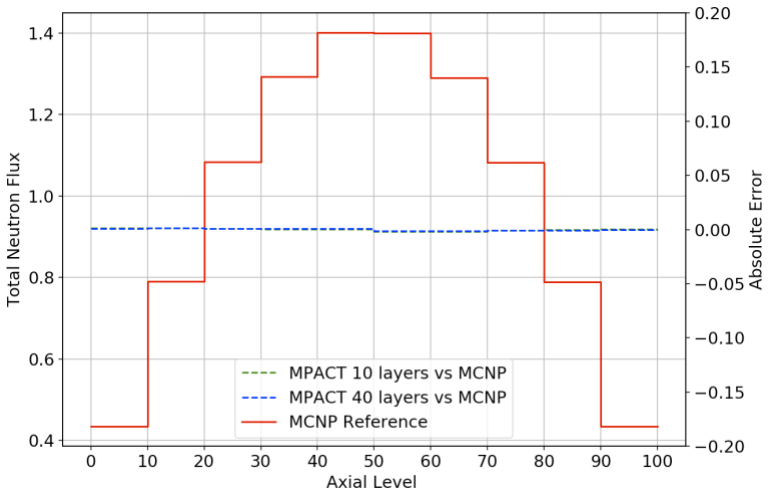


Figure 6-23 $B_4C$ 5x5 3D: Axial Neutron Flux with Control Rod Fully Inserted

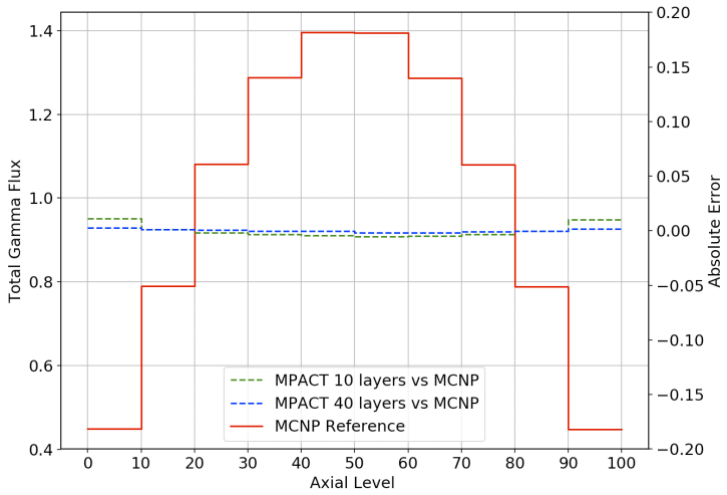


Figure 6-24 $B_4C$ 5x5 3D: Axial Gamma Flux with Control Rod Fully Inserted

Another test was done on the same $B_4C$ 5x5 3D case but with the control rod half inserted. Axial neutron flux and gamma flux are in Figure 6-25 and Figure 6-26 respectively. The agreement between MCNP and MPACT on neutron flux results verifies the effectiveness of this modeling. Gamma flux results from MPACT are noticeably different compared

with results from MCNP, but using finer axial meshes in MPACT can greatly improve the accuracy. As shown in Figure 6-26, if the calculation is performed with 40 axial layers and integrated into 10, the differences with MCNP reference are all within 1%.

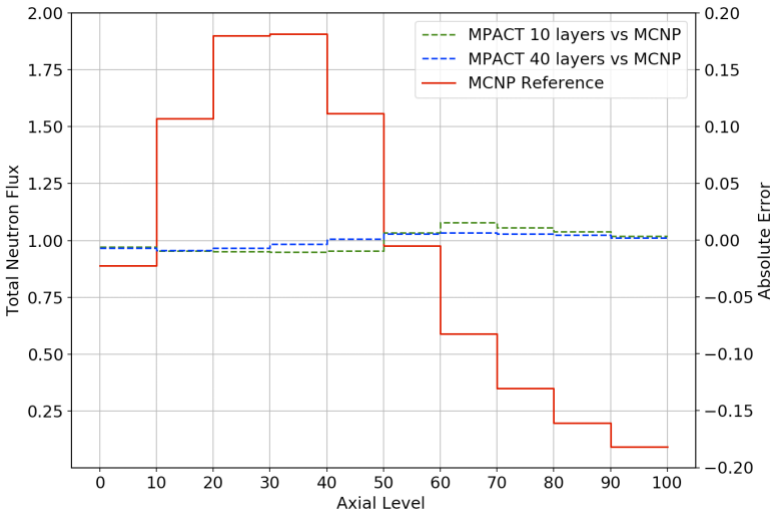


Figure 6-25 $B_4C$ 5x5 3D: Axial Neutron Flux with Control Rod Half Inserted

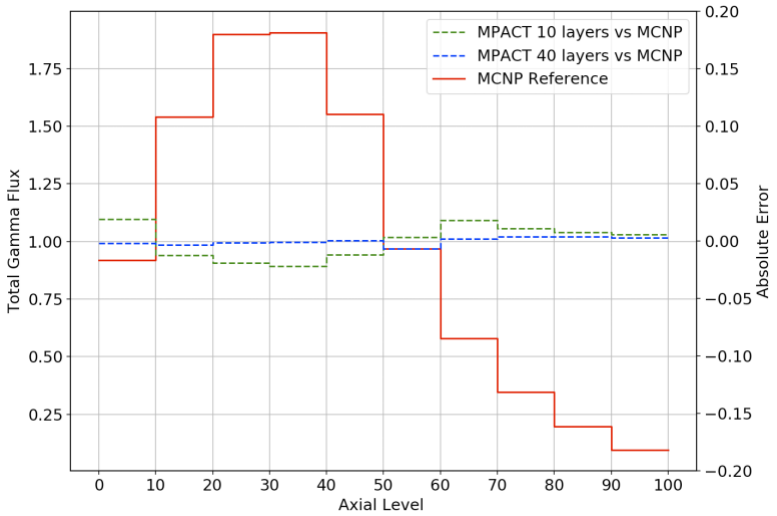


Figure 6-26 $B_4C$ 5x5 3D: Axial Gamma Flux with Control Rod Half Inserted

### 6.2.4. Heat Deposition

The newly implemented gamma heating calculation capability in MPACT was tested on VERA Progression problem 2b. As shown in Figure 6-27, heat depositions in guide tubes are about 15-20% of the values in the surrounding fuel pins. Figure 6-28 shows the

differences between MCNP and MPACT on gamma energy deposition distribution. Note that, as discussed in Section 6.1.3, turning off photon fluorescent effect in MCNP can significantly affect gamma deposition, so the photon fluorescent effect is turned on in MCNP for all gamma deposition calculations. From Figure 6-28, one can see that MPACT results are consistent with MCNP results with photon fluorescence on and relative errors in all pins are under 1%.

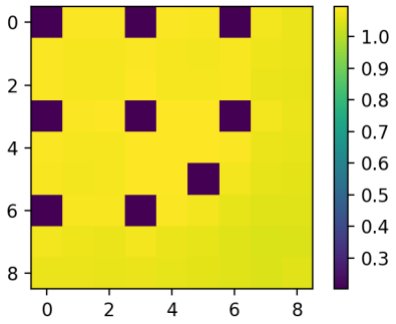


Figure 6-27 2b: Gamma Heating by MPACT

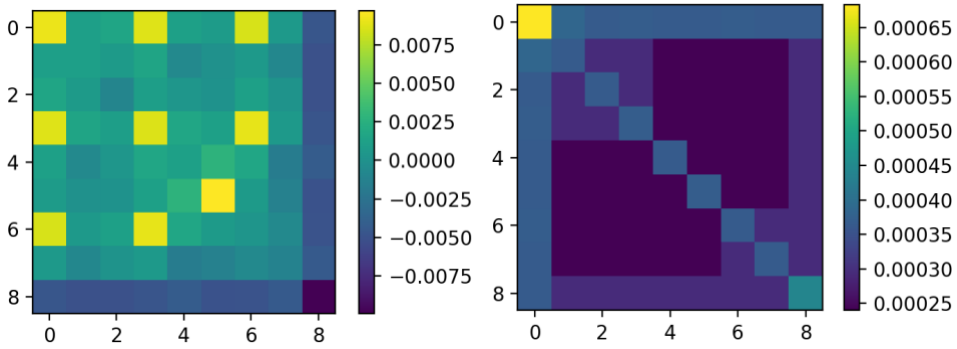


Figure 6-28 2b: Gamma Heating Relative Errors MCNP vs MPACT (Left) and MCNP Relative Uncertainty (Right)

Gamma heating calculation for problem 2h is shown in Figure 6-29. Gamma heating in a $B_4C$ control rod is about 25-30% of that in a fuel rod pin. This is higher than that in an empty guide tube in case 2b because $B_4C$ has a stronger gamma source than a moderator. The errors are < 1% in most pins compared to MCNP. The maximum difference of 3% only occurs at the central guide tube pin where the absolute gamma deposition value is low.

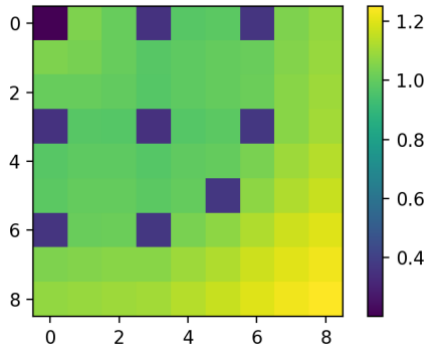


Figure 6-29 2h: Normalized Gamma Heating by MPACT

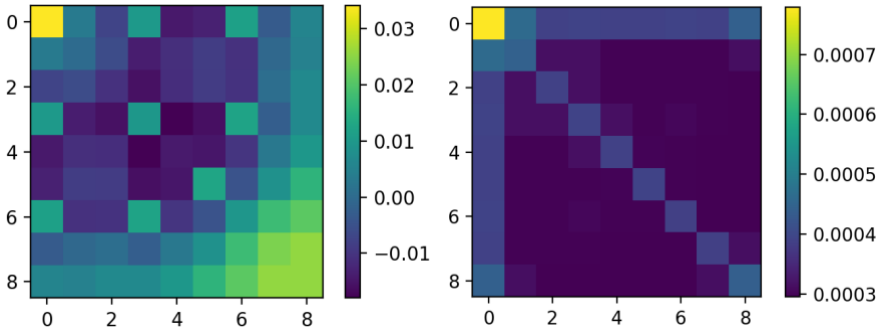


Figure 6-30 2h: Gamma Heating Relative Errors MCNP vs MPACT (Left) and MCNP Relative Uncertainty (Right)

Finally, the performance of gamma deposition calculations on 3D problems is tested using the $B_4C$ 5x5 3D case. The axial gamma heating distribution shown in Figure 6-31 has a similar pattern as the axial gamma flux shown in Figure 6-24. Axial gamma deposition errors are 2-3% on average when MPACT is running with 10 axial meshes, and using finer axial meshes can improve the results just as in the flux calculations. When the MPACT run is performed using 40 meshes and integrating into 10 meshes to compare with MCNP, the errors are less than 0.5% in 9 out of 10 meshes. One exception is the bottom of control rod, which shows a 2% difference. Overall, the gamma heating scheme with the 2D/1D transport solver gives accurate results for gamma energy deposition on 3D calculations.

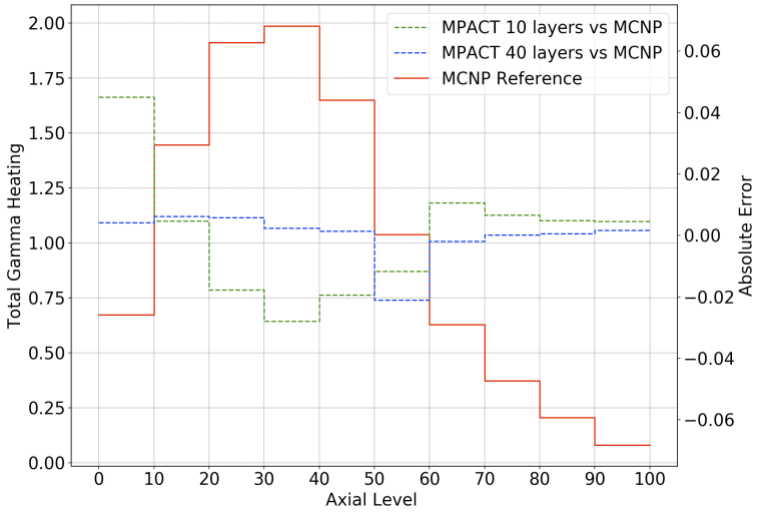


Figure 6-31 $B_4C$ 5x5 3D: Axial Gamma Deposition with Control Rod Half Inserted

## 6.3. Gamma Heating Calculated by GDM

This section presents the numerical results of the gamma deposition matrix method. To use the GDM method, a vector containing the source intensity of each pin cell, which is the $[Q_{j1}, Q_{j2}, \dots, Q_{jN}]^T$ vector in equation ( 4.8 ), and the GDM, matrix F in equation ( 4.8 ), are required. In this work, the Q vector is computed by MPACT's n-gamma source calculation scheme using the converged neutron flux after eigenvalue iterations, and the matrix F is generated through fixed source runs in MCNP. Furthermore, to verify the accuracy of the gamma deposition results from GDM method, references are generated using MCNP for comparison. Specifically, for each test case, the reference is created by putting all the sources into the core all at once, executing the fixed source run and tallying heat depositions in each pin in MCNP.

### 6.3.1. Quantitative Error Acceptance Criteria

CASL's accuracy goal for V4.2m5 and V5.0m0 multigroup cross section libraries for MPACT for PWR and BWR development [30] is used as a reference to quantitatively assess the errors of the GDM method with different approximations and energy

preservation approaches. According to Chapter 2 of [30], errors in pin power distribution shall be less than ±1.5% for 2D assembly cases and less than ±2.5% for 2D core cases. To use this criteria to evaluate gamma calculation errors, gamma errors should be converted to pin power error contributions so that the comparison is consistent. The relationship is shown in equation ( 6.9 )

$$Pin\ Power\ Error\ from\ Gamma\ Power\ Error = \frac{Gamma\ Power}{Total\ Power} \cdot Gamma\ Power\ Error \quad (6.9)$$

Although it is known that the (gamma power) / (total power) ratio in a whole LWR is about 10%, knowing the exact portion of energy deposition contributed by gamma in each individual pin cell can help to quantify the errors more accurately. Therefore, pin-wise (gamma power) / (total power) ratio distribution maps of CASL Progression problem 5b-2d [2] are plotted as shown in Figure 6-33. The maps are obtained from a previous energy deposition distribution analysis work on 5b-2d originally presented in [3]. Problem 5b-2d is similar to 5a-2d but with AIC control rods. As one can see, the (gamma power) / (total power) ratio could be 8.5% to 13% in fuel pins and up to 38% in non-fuel pins. To make the criteria realistic while strict, the upper bounds of (gamma power) / (total power) in this core problem, 13% in a fuel pin and 38% in a non-fuel pin, are selected for gamma power error to induced pin power error conversion factor in the rest of this section. In other words, if the observed error in the gamma heating calculation is X% in the fuel, then if 13% of X% is less than the CASL error criteria of 1.5%, the gamma heating error is within the bounds of what is considered to be an acceptable error for the pin power. However, it isn't clear how to scale gamma heating errors in the non-fuel regions.

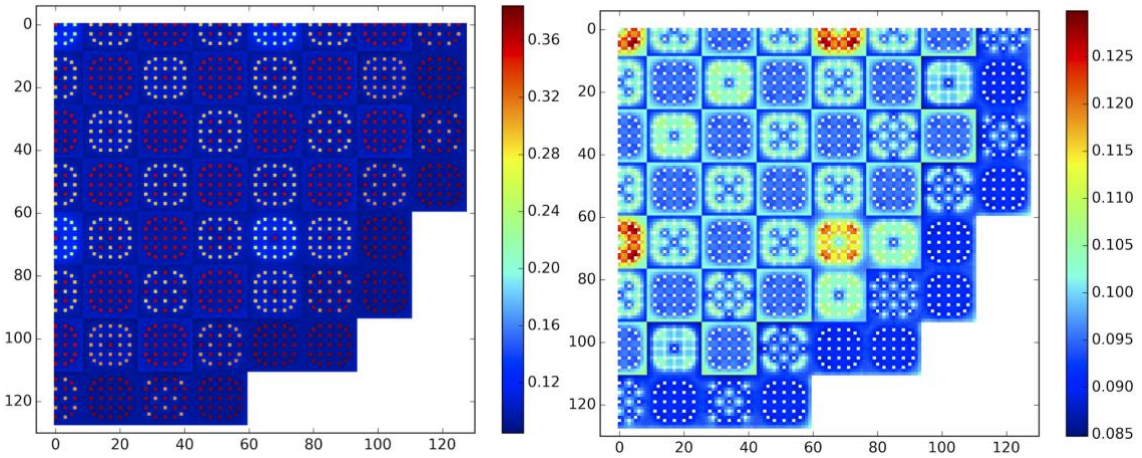


Figure 6-32 CASL 5b-2D: Gamma Power / Total Power in Each Pin (Left) and Each Fuel Pin (Right)

### 6.3.2. Full Sized GDM

Verification of the GDM method starts with a 2D 29x29 case with vacuum radial boundary. This case is based on the IPEN reactor core [31] and modified for this work. A quarter plot of the configuration is shown in Figure 6-33. Temperature of the whole problem is 293K.

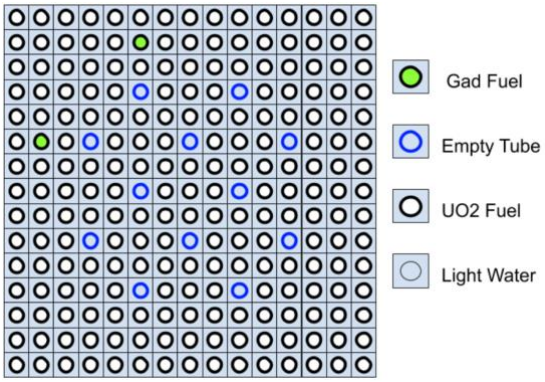


Figure 6-33 Modified IPEN: Configuration Quarter Plot

The MCNP fixed source reference is shown in Figure 6-34. The central pins are much hotter than the boundary pins due to the vacuum boundary and guide tubes have much lower heat than adjacent fuel pins.

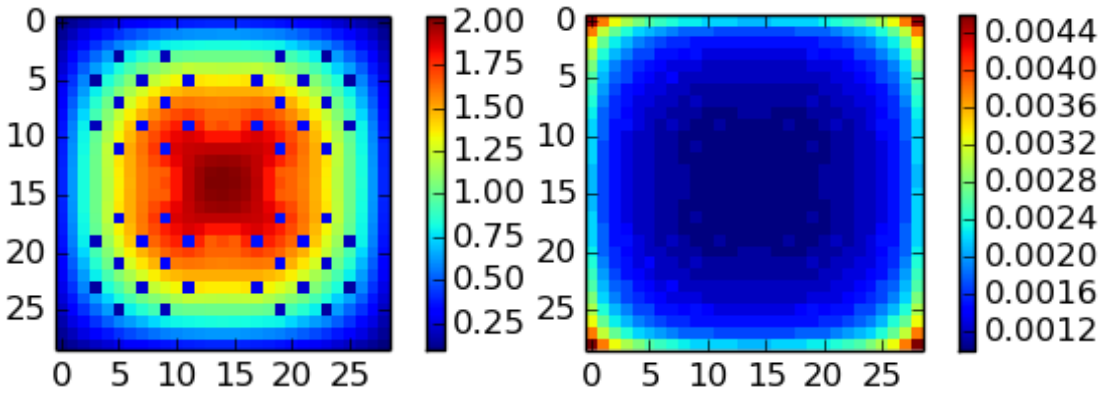


Figure 6-34 Modified IPEN: Reference Gamma Heat Distribution (Left) and Uncertainty (Right)

The first step of the verification work is to verify the effectiveness of the GDM method without any spatial approximations. That is, each of the matrix generation runs is performed on the whole problem domain and every matrix element $F_{j\to i}$ is explicitly tallied and stored without any approximations or truncations. In other words, the subdomain is just the problem domain and no energy preservation corrections are needed.

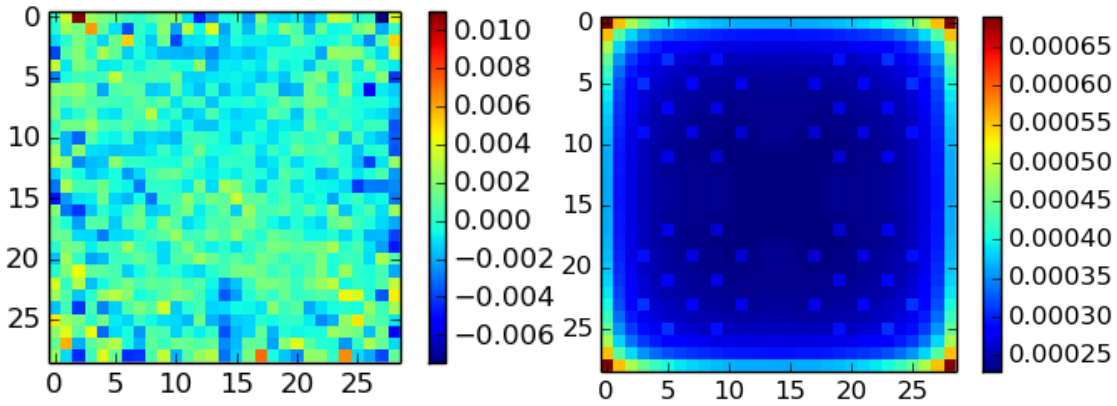


Figure 6-35 Modified IPEN: Gamma Heat Distribution by Full Sized GDM VS Reference Relative Errors (Left) and Uncertainty of GDM Results

The gamma heat deposition distribution calculated by the full sized GDM is compared with the reference and the relative errors are shown in Figure 6-35. The errors in most pins are about 0.2% or less and the maximum error is about 1%. Moreover, the errors are randomly distributed, which means they are mainly from the uncertainty in the MCNP results. From equation ( 6.9 ), one can easily calculate that the maximum pin power error contributed by gamma heat from GDM method would be no more than (13%*1%=) 0.13%, which is well below the 1.5% standard for 2D assembly cases as introduced in Section 6.3.1. Thus, it is

reasonable to quantitatively conclude that the errors of the full sized GDM method are low enough to be acceptable. Next, performance of the various approximations for the GDM method will be tested.

### 6.3.3. Spatially Reduced GDM

This section tests the accuracy of the GDM method for subdomain simplification. The 29x29 modified IPEN case same as Section 6.3.3 is used for this test. The subdomain size is chosen to be 21x21 and no further simplifications or corrections are applied. In other words, each fixed source matrix generation run is performed on the 21x21 subdomain, gamma deposition in each cell is tallied explicitly and deposition outside of the 21x21 subdomain is neglected.

The spatial gamma energy deposition calculated by the GDM method with a 21x21 subdomain is shown in Figure 6-36 and comparison with the reference is in Figure 6-37. The relative errors are not trivial with a maximum to be about 10%. Quantitatively, according to equation ( 6.9 ) and the 13% (gamma power) / (total power) ratio, the 10% maximum gamma power error can lead to a pin power error of approximately 1.3%. Since this is very close to the 1.5% upper limit, this order of error may not be acceptable. On the other hand, these high errors are only in low-deposition corner pins, so these errors will not significantly affect the pin power calculations of the whole problem overall. But it is prudent to improve the methodology to reduce these errors to a level that is clearly not going to increase the overall area in the pin powers.

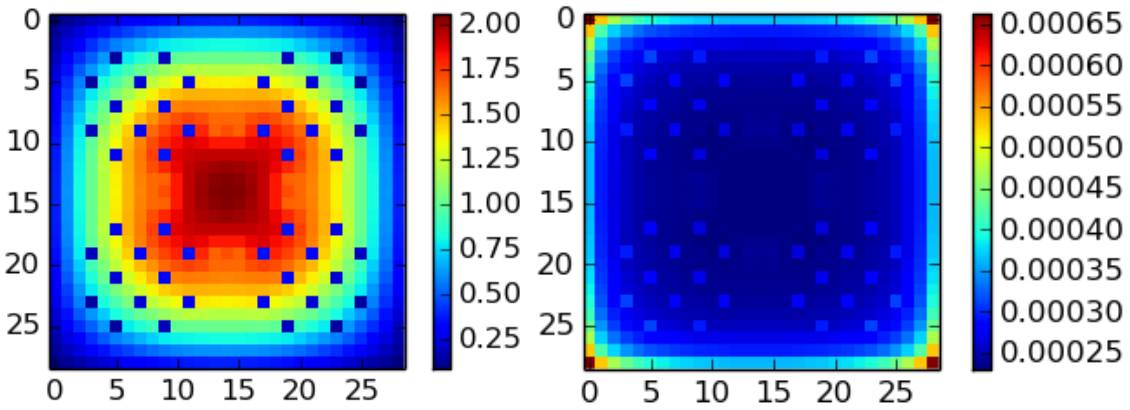


Figure 6-36 Modified IPEN: Gamma Heat Distribution by GDM with 21x21 Subdomain (Left) and Uncertainty (Right)

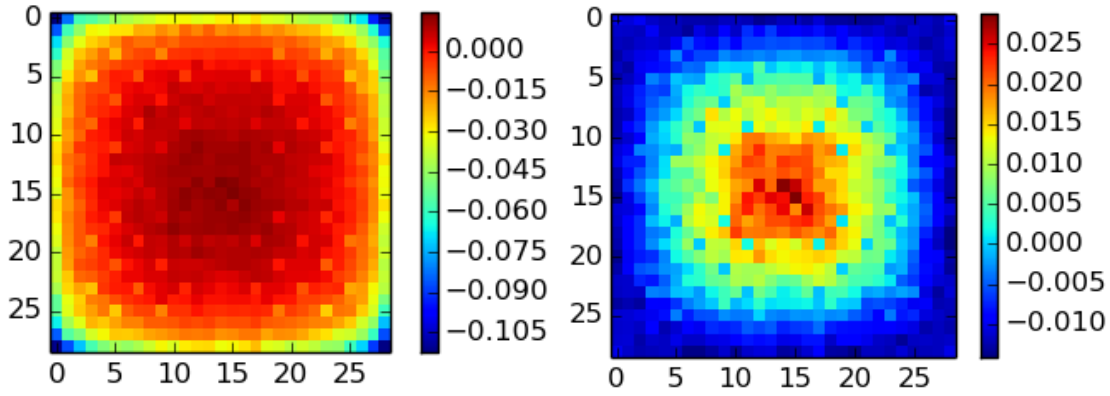


Figure 6-37 Modified IPEN: Gamma Heat Distribution by GDM with 21x21 Subdomain vs Reference Relative Errors (Left) and Absolute Errors (Right)

### 6.3.4. Spatially Reduced GDM with Secondary Domain Approximation

Next, the subdomain will be simplified by the secondary domain approximation. This is tested on the same 29x29 modified IPEN case. The subdomain size is still 21x21 like that in Section 6.3.3, and the primary domain is chosen to be 15x15. Deposition in the outermost 3 rings of the subdomain will be calculated by the segment-based secondary domain approximation approach introduced in Section 5.2.2. The results are shown in Figure 6-38 and comparison with the reference is in Figure 6-39.

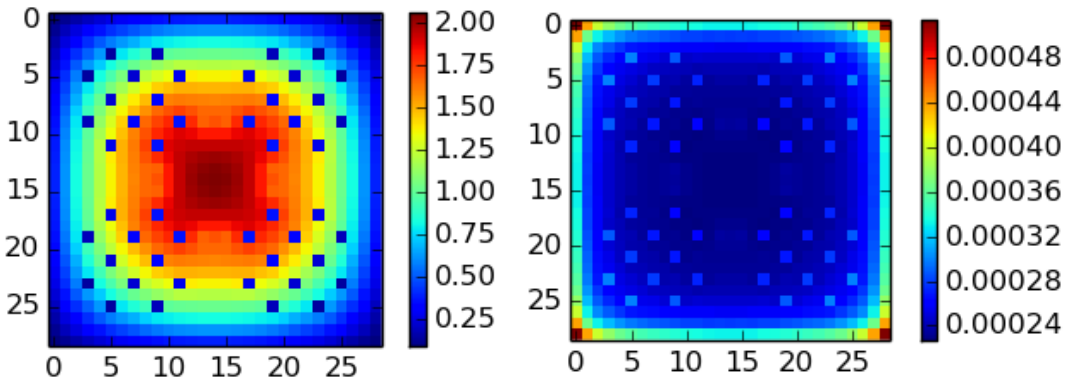


Figure 6-38 Modified IPEN: Gamma Heat Distribution by GDM with 21x21 Subdomain and 15x15 Primary Domain Results (Left) and Uncertainty (Right)

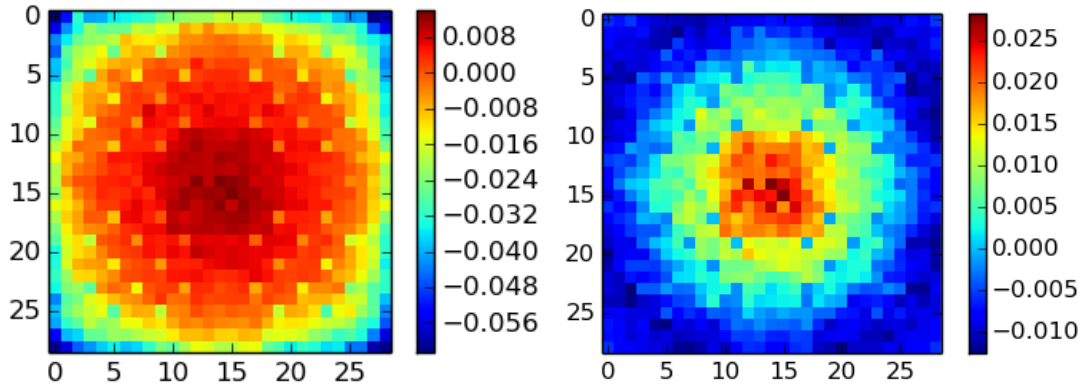


Figure 6-39 Modified IPEN: Gamma Heat Distribution by GDM with 21x21 Subdomain and 15x15 Primary Domain vs Reference Relative Errors (Left) and Absolute Errors (Right)

Surprisingly, although more simplifications are applied, the errors are actually lower than those in Section 6.3.3 especially in boundary pins. This could be due to that, when the secondary domain approximation redistributes the gamma heat in the side rectangle to each pin, the heat is evenly redistributed. For example, a pin at the end of a rectangle, like cell $i_2$ in the yellow side rectangle in Figure 6-40, gets the same amount of gamma energy as a pin in the middle of the same rectangle, cell $i_1$ in Figure 6-40, from the flat redistribution scheme. However, physically, $i_2$ is further from the source than $i_1$ and thus $i_2$'s deposition should be lower than $i_1$, which means the flat redistribution scheme overestimates heat deposition in end pins. As shown in Figure 6-37, when the GDM is using 21x21 subdomains and no other simplifications, the GDM method underestimates the heat

deposition in corner pins. As a result, the underestimated core corners are partially balanced by the overestimated subdomain corners.

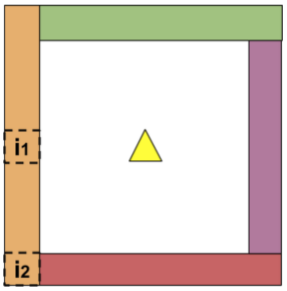


Figure 6-40 Pin Cells on a Secondary Domain Ring

From equation ( 6.9 ) and the error acceptance criteria in Section 6.3.1, the maximum gamma power error from this 21x21 subdomain + 15x15 primary domain GDM approach, ~6%, would contribute a pin power error of up to 0.78%, which is well below the required 1.5% but can still be improved, as will be seen in the coming sections.

### 6.3.5. Flat Energy Preservation Correction

Although the errors of the two approaches in Section 6.3.3 and 6.3.4 are within the acceptable range numerically, completely ignoring energy deposition outside of the subdomains still violates the conservation of energy and thus the two approaches cannot be adopted as the default GDM method. To resolve this issue, the flat energy preservation correction mentioned in Section 5.3 is applied to the 21x21 subdomain + 15x15 primary domain GDM approach. The test is on the same 29x29 modified IPEN case. The gamma heat deposition calculated by this approach is shown in Figure 6-41 and comparison with the reference is in Figure 6-42.

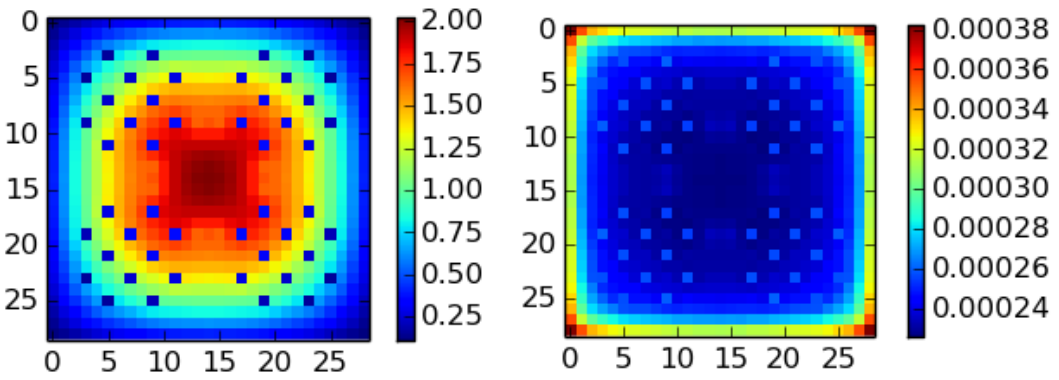


Figure 6-41 Modified IPEN: Gamma Heat Distribution by GDM with 21x21 Subdomain, 15x15 Primary Domain and Flat Outside Energy Preservation (Left) and Uncertainty (Right)

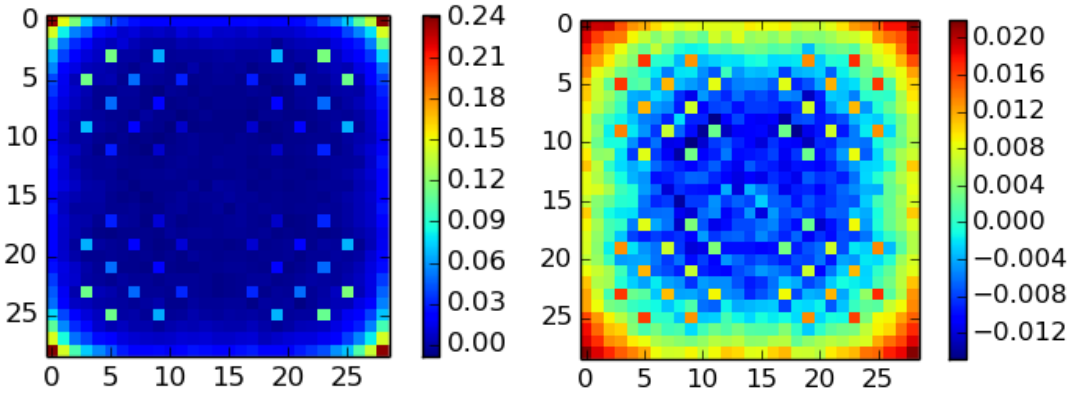


Figure 6-42 Modified IPEN: Gamma Heat Distribution by GDM with 21x21 Subdomain, 15x15 Primary Domain and Flat Outside Energy vs Reference Relative Errors (Left) and Absolute Errors (Right)

One can see that the errors are not negligible especially in the guide tube pins, in which the relative errors can be higher than 10%, and corner pins, in which the relative errors can reach 24%. This 24% maximum gamma power error in fuel pins could lead to a pin power error potentially as high as 3.12% according to Section 6.3.1. Although such high errors are only in low-power corner pins, it is still not within the acceptable range because 3.12% is more than double the pin power error tolerance. Furthermore, errors from gamma energy deposition are only a portion of the total pin power errors. As for the guide tube pins, as the highest gamma portion in a guide tube pin can reach 38% and the highest error of gamma deposition in guide tube pins by this approach is about 10%, errors in the guide tube gamma energy deposition could be up to 3.8%, which may also be too high although there is no CASL error criteria for the heat generation in the guide tubes.

The reason for such large errors is the use of the flat energy preservation approach. For example, the actual matrix value $F_{j\to i}$ in a pin cell i very far away from the subdomain, like cell $i_1$ in Figure 6-43, would be much smaller than a pin cell just outside of the subdomain, like cell $i_2$. However, the flat redistribution scheme will give these two cells identical $F_{j\to i}$'s. As a result, the flat energy preservation approach will overestimate the heat deposition in the corner pins whose absolute heat deposition is supposed to be very small. For the same reason, the flat energy preservation approach will give a guide tube pin an $F_{j\to i}$ identical to that of a fuel pin, which will lead to overestimated non-fuel pin heat deposition. Therefore, the 21x21 subdomain + 15x15 primary domain + flat energy preservation is not an accurate approximation for the GDM method.

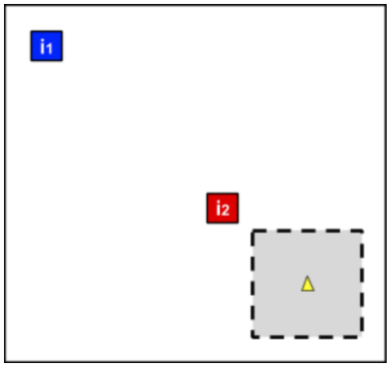


Figure 6-43 Pin Cells Outside of the Subdomain

Besides the poor accuracy, another disadvantage of this energy preservation approach is that it requires the "energy to be preserved" to be known. Equivalently, "total energy deposition from fixed source run on the whole problem domain" in equation ( 5.1 ) is needed to calculate "energy to be put back" through equation ( 5.1 ). For this verification purpose, this value is obtained from the full sized GDM as $\sum_i F_{j\to i}$ over all the cell i in the whole problem domain, but in practice the full sized GDM and thus the "energy to be preserved" are not available. As a result, to avoid using the non-physical energy distribution scheme and the practically unavailable "total energy deposition from fixed source run on the whole problem domain" factor, a more advanced energy preservation approach, leakage-based preservation correction, was developed.

### 6.3.6. Leakage-based Preservation Correction

The test case for this section is also the 29x29 modified IPEN case. The detailed mechanism of the leakage-based preservation correction approach is described in Section 5.3. Compared to the flat energy preservation approach, this approach uses energy leakage on the subdomain boundary, instead of relying on the full sized GDM to determine the energy to be preserved, which is not practical for realistic problems. Furthermore, the energy preserved by scaling up the matrix entries in the secondary domain. In other words, the distribution scheme is based on an authentic gamma distribution profile instead of a non-physical flat distribution, which means this approach could avoid the observed errors in non-fuel pins and corner pins. Heat distribution calculated by GDM method with 21x21 subdomain, 15x15 primary domain and the leakage-based energy preservation approach is shown in Figure 6-44 and comparison with the reference is in Figure 6-45.

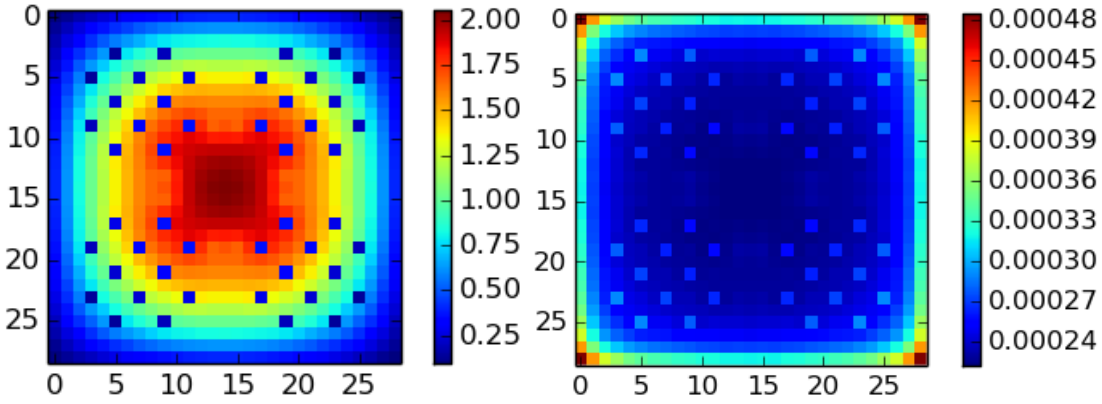


Figure 6-44 Modified IPEN: Gamma Heat Distribution by GDM with 21x21 Subdomain, 15x15 Primary Domain and Leakage-based Energy Preservation (Left) and Uncertainty (Right)

As shown in Figure 6-45, the relative errors are < 0.5% in most pins except the outermost pins of the core. For these boundary pins, the maximum relative error is still reduced from 5.6% in Section 6.3.4 to 2.5%. Given the 13% maximum (gamma power) / (total power) ratio from to Section 6.3.1, gamma-induced pin power error will be no more than (13%*2.5%=) 0.33%, which is far lower than the 1.5% standard. Compared to other approximation and correction approaches in Section 6.3.3 through 6.3.5, this secondary domain approximation + leakage-based energy preservation correction successfully

reduced errors while maintaining energy conservation and being relatively straightforward to implement.

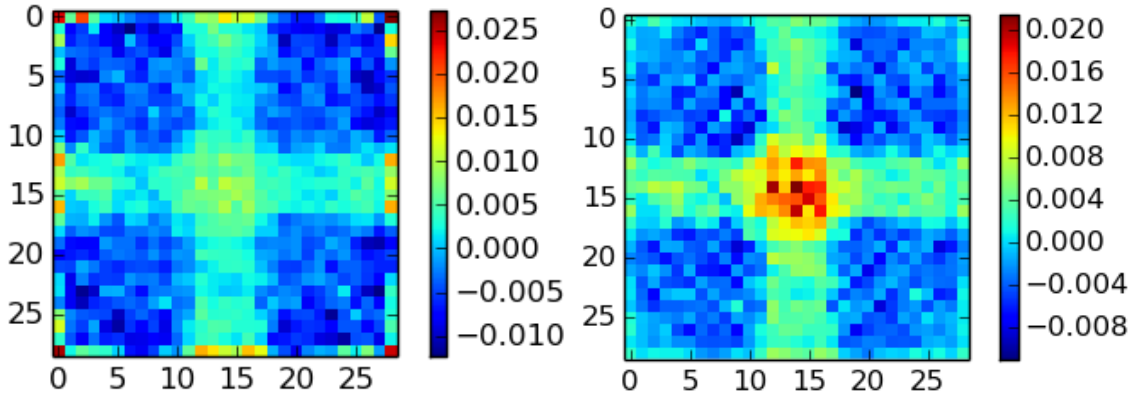


Figure 6-45 Modified IPEN: Gamma Heat Distribution by GDM with 21x21 Subdomain, 15x15 Primary Domain and Leakage-based Energy Preservation vs Reference Relative Errors (Left) and Absolute Errors (Right)

A summary of the error analysis of the GDM method and different approximation approaches from Section 6.3.2 to Section 6.3.6 is shown in Table 6-1. In conclusion, the full sized GDM method is the most accurate approach and the 21x21 subdomain + 15x15 primary domain + leakage-based energy preservation is the most reliable and feasible scheme with approximations.

Table 6-1 Summary of Error Analysis of Different Approximation Approaches

| GDM Mode | Maximum Error | Errors Under Criteria Numerically | Obey Conservation of Energy |
|---|---|---|---|
| **Full Sized GDM** | 1.3% | Yes | Yes |
| **21x21 Subdomain** | 10% | Yes | No |
| **21x21 Subdomain +15x15 Primary Domain** | 6% | Yes | No |
| **21x21 Subdomain +15x15 Primary Domain +Flat Energy Preservation** | 24% | No | Yes |
| **21x21 Subdomain +15x15 Primary Domain +Leakage-based Preservation** | 2.5% | Yes | Yes |

### 6.3.7. 3D Case

Next, the GDM method is used on the $B_4C$ 5x5 3D problem first introduced in Section 6.2.3 to test its performance on 3D problems. Note that, as the $B_4C$ 5x5 3D case is small, the subdomain approximation is not used and there is no need for an energy preservation scheme. The GDM for this calculation is a full sized GDM. The results and comparison with the MCNP fixed source reference are on Figure 6-46. The relative errors are all less than 0.3%, which proves the validity of the method on 3D problems.

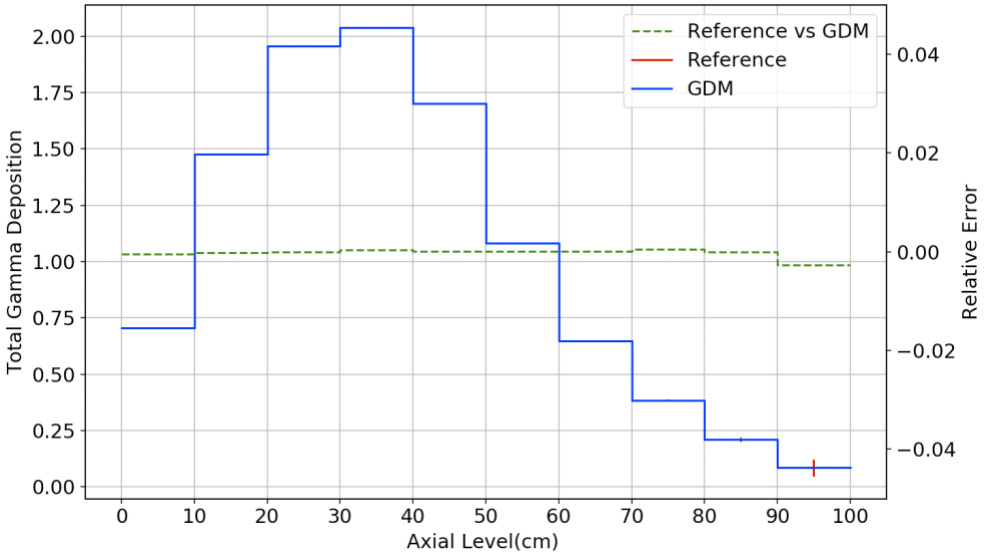


Figure 6-46 $B_4C$ 5x5 3D: Gamma Heat Distribution by Full Sized GDM vs Reference

### 6.3.8. Full SMR Core Case

So far, the GDM method has only been used to calculate small cases. When a new method is developed, it should be tested on whole core cases to test its scalability. The application to larger geometries is even more important for the GDM method because, as stated at the beginning of Chapter 5, the subdomain simplification is primarily developed for large problems. For instance, for a 29x29 problem like the modified IPEN, using a reduced GDM generated on 21x21 subdomains is not a very significant simplification compared to the full sized GDM, but using subdomains of similar sizes to calculate whole core cases can dramatically reduce the matrix generation time and memory usage compared to the full sized GDM. For example, if 21x21 subdomains are used on the VERA Progression

problem 5a-2d, then, for most of the matrix generation runs, it can be shown that, for each GDM generation run, 55336 of the 55777 pins can be eliminated.

To test the GDM method's performance on a whole core configuration, a small modular reactor case with 37 assemblies was created and its configuration is shown in Figure 6-47. Each assembly in this SMR case is 21.5 cm wide and contains 17x17 pins including 25 non-fuel pins just like the assemblies in VERA Progression problems 2 through 5. Dimensions of the fuel pins, the Pyrex insertion pins and the guide tube pins in this SMR case are all identical to those in the CASL 4a-2d case. The reactor radius is 85.0 cm, temperature is 293K and boron level is 1200 ppm. For this case, the GDM method will be tested with the spatially reduced GDM generated in a 23x23 subdomain with a 17x17 primary domain and a leakage-based energy preservation correction for the secondary domain. Also, as mentioned at the beginning of Section 6.3, the source intensity vector Q is computed by the n-gamma scheme with the converged neutron flux from k-eigenvalue iterations on this SMR problem in MPACT.

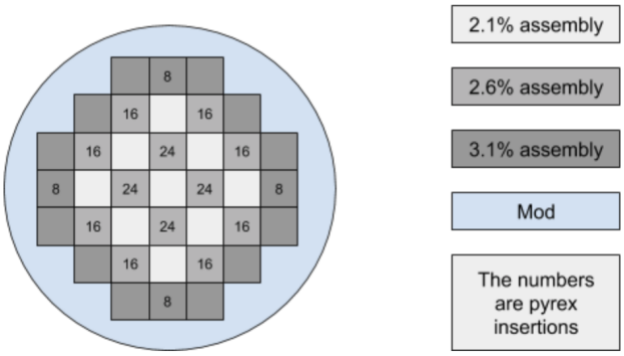


Figure 6-47 7x7 SMR: Configurations

Figure 6-48 is the gamma heat distribution reference generated through MCNP fixed source run and Figure 6-49 is the gamma heat distribution calculated by the GDM method. The reference is generated using MCNP by putting all the gamma sources into the core all at once, executing the fixed source run and tallying heat depositions in each pin. Qualitatively, the GDM calculated results show the same distribution pattern as the reference results: assemblies with higher concentration fuels have higher gamma power,

central assemblies are hotter than boundary assemblies and gamma deposition in pins close to the problem boundary, especially the corners, is extremely low.

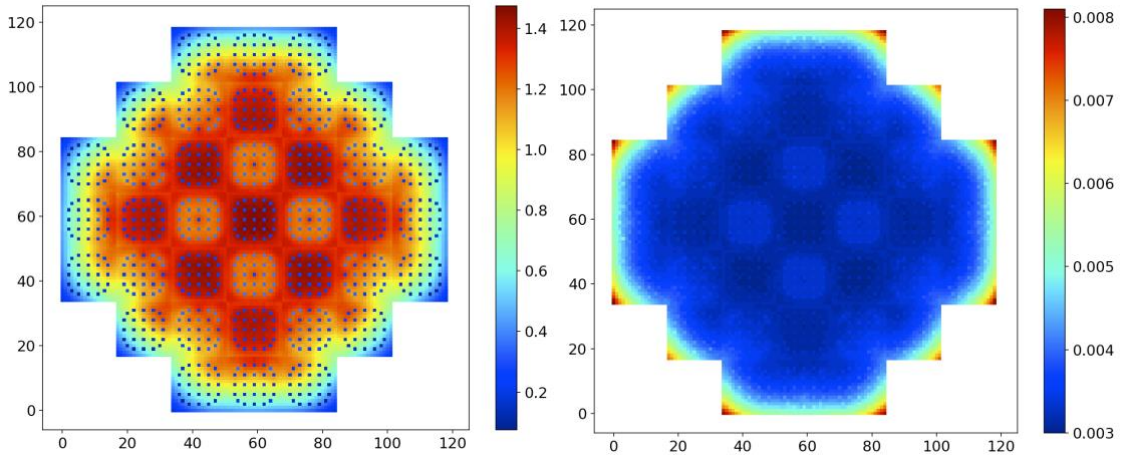


Figure 6-48 7x7 SMR: Reference Heat Distribution (Left) and Uncertainty (Right)

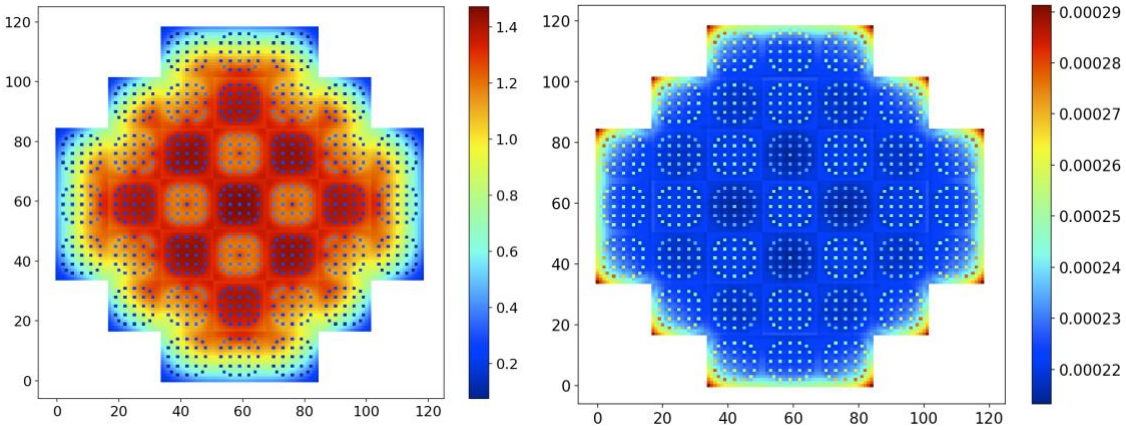


Figure 6-49 7x7 SMR: Gamma Heat Distribution by GDM with 23x23 Subdomain, 17x17 Primary Domain and Leakage-based Energy Preservation (Left) and Uncertainty (Right)

Quantitatively, the relative errors between the GDM results and the reference are shown in Figure 6-50. Pins close to the corners of the core could have very high relative errors, which are up to approximately 19%. The reason for these large errors could be that the leakage-based energy preservation approach does not work well for zigzag boundaries. Considering the (gamma power) / (total power) factor presented in Section 6.3.1, which is 13% in fuel pins, a 19% error in gamma power can lead to 2.47% error in pin power. An error of this level is not acceptable generally because, if deviations contributed by all other forms of energy deposition are taken into account, the total pin power error is very likely

to be out of the ±2.5% accuracy goal for 2D core cases [30]. However, when zoom in on one of the corners in Figure 6-50, as shown in Figure 6-51, one can see that the number of pins with relative errors > 5% is very small and errors in most pins are still < 1% even in the corner assemblies. Besides, just like corner pins in the 29x29 modified IPEN case, these pins with high relative errors all have low absolute gamma deposition values due to boundary leakage, which means that the absolute errors are still within the reasonable range as shown in Figure 6-52. If equation ( 6.9 ) is applied to absolute errors, the maximum absolute pin power error induced by gamma error would be about 0.6%, which is noticeably lower than the ±2.5% standard.

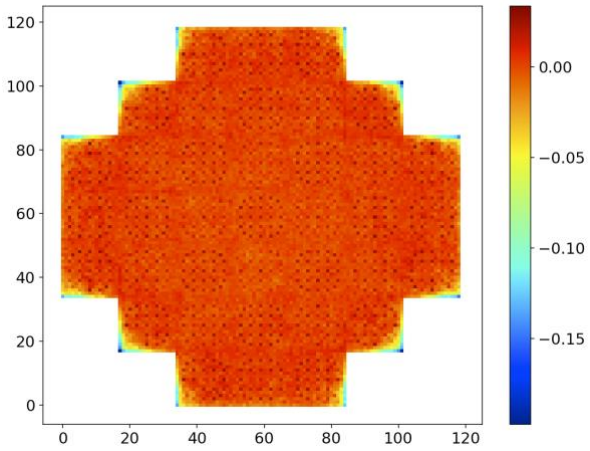


Figure 6-50 7x7 SMR: Gamma Heat Distribution by GDM with 23x23 Subdomain, 17x17 Primary Domain and Leakage-based Energy Preservation vs Reference Relative Errors with Default Colorbar Range

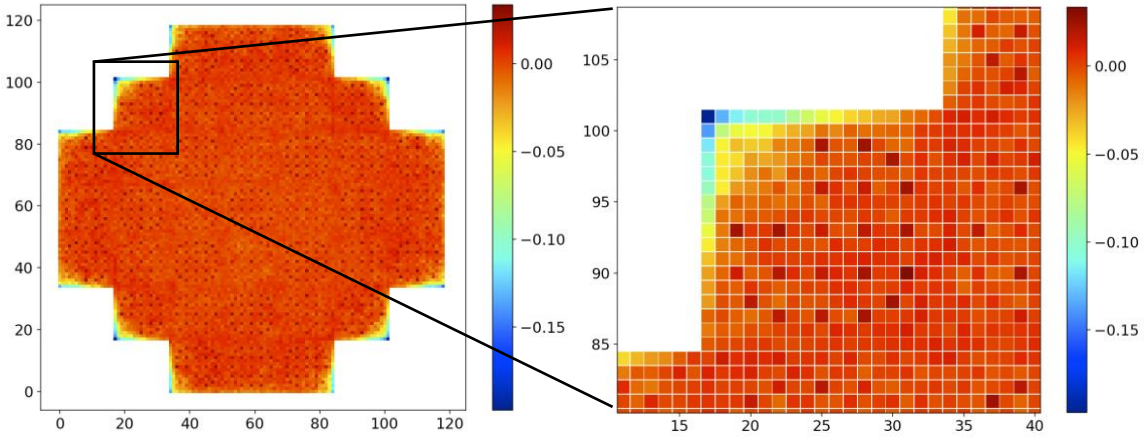


Figure 6-51 7x7 SMR: Gamma Heat Distribution by GDM with 23x23 Subdomain, 17x17 Primary Domain and Leakage-based Energy Preservation vs Reference Relative Errors of a Boundary Corner

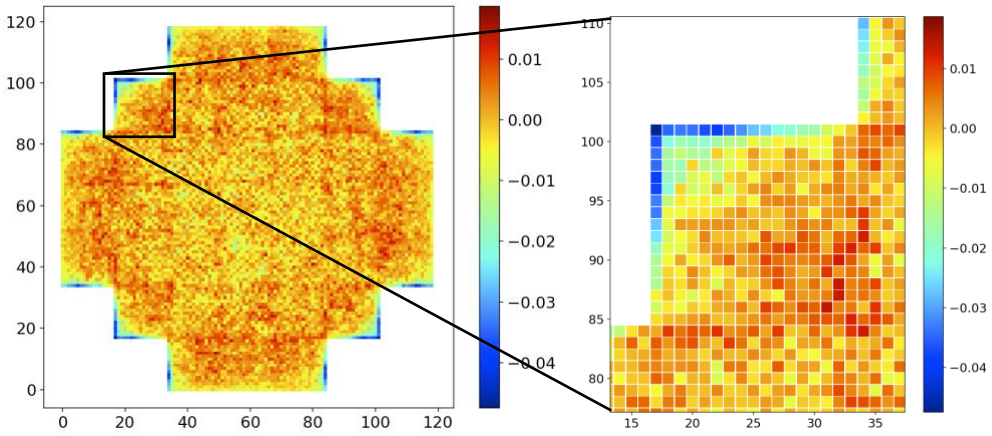


Figure 6-52 7x7 SMR: Gamma Heat Distribution by GDM with 23x23 Subdomain, 17x17 Primary Domain and Leakage-based Energy Preservation vs Reference Absolute Errors

To read the errors inside the core clearer, colorbar of Figure 6-50 is set to a narrower range and the new plot is in Figure 6-53. It can be seen that generally relative errors in fuel pins and Pyrex insertion pins are < 0.5%. Errors in guide tube pins are slightly higher than those in Pyrex pins. This can be explained by the $e^{1.6}$-based non-fuel pin correction factors for secondary domain energy redistribution. As shown in Table 5-1, a Pyrex insertion pin's $e^{1.6}$-based non-fuel pin correction factor agrees well with the realistic gamma deposition with a difference of 2.3%, but the guide tube pin's correction factor and real gamma deposition are off by 12.7%. The maximum gamma power relative error in guide tube pins is about 2.5%. If the (gamma power / total power) ratio, which is 38% for non-fuel pins, is taken into account, the 2.5% gamma power error can lead to a 0.95% pin power error.

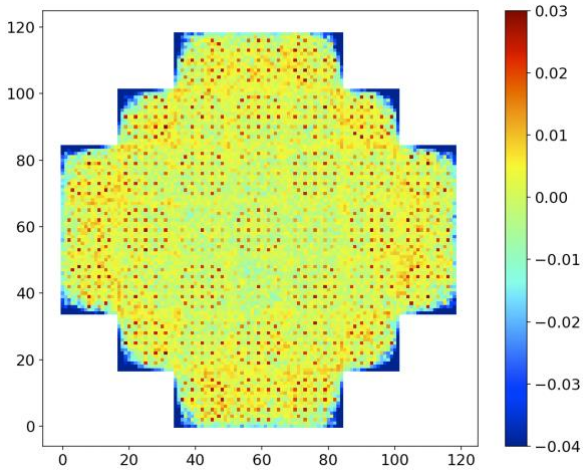


Figure 6-53 7x7 SMR: Gamma Heat Distribution by GDM with 23x23 Subdomain, 17x17 Primary Domain and Leakage-based Energy Preservation vs Reference Relative Errors with Narrower Colorbar Range

Finally, to evaluate the computational performance of the GDM method, CPU times for the fixed source GDM generation runs as well as the matrix-vector multiplication scheme, $\vec{D} = F \cdot \vec{Q}$, in MPACT were estimated and compared with measured CPU times for the explicit gamma transport solver in MPACT. The results are shown in Table 6-2. Note that the "one gamma transport sweep on the whole problem domain" corresponds to one step of the explicit gamma transport solver, or equivalently the 3rd block in Figure 2-2. Also, the CPU time for a fixed source matrix generation run is estimated by creating a 23x23 vacuum boundary problem, manually placing a fixed gamma source in the central pin cell and counting the time to solve this fixed source problem and calculate the gamma heating. For the matrix-vector multiplication time estimation, there are 10693 (37*17*17) pin cells in this SMR case, and the dimensions of the matrix and the vector are set according to the core size to reproduce the realistic $\vec{D} = F \cdot \vec{Q}$ calculation. The vector is of size 10693, representing the pin-wise gamma source distribution. The matrix is a 10693*10693 sparse matrix with only 529 (23*23) non-zero entries in each row because, with the subdomain approach, heat deposition in cell *i* is at most due to 529 different source regions.

Table 6-2 CPU Time for MPACT GDM versus MPACT Gamma Transport

| Computational Step | Estimated CPU Time | Estimated # of Executions | Total CPU Time |
|---|---|---|---|
| **One gamma transport sweep on the whole problem domain** | 23.6 s | 500[1] | 3.28 h |
| **One fixed source matrix generation run on 23x23 subdomain** | 2.50 s | 1388[2] | 0.96 h |
| **The matrix-vector multiplication** | 0.0068 s | 500[1] | 3.4 s |

1. 25 statepoints x 20 iterations/statepoint
2. Number of pin cells in 1/8 of the SMR core.

As shown in Table 6-2, one can see that the matrix-vector multiplication is essentially free compared to any other step. The only issue is the CPU time to generate the GDM generations vs explicit gamma transport sweeps. Assuming that there are 25 statepoints and each statepoint requires 20 iterations, the 500 explicit gamma transport sweeps would

consume 3.4x the time to execute the 1388 matrix generation runs on 23x23 subdomains, which affirms the efficiency of the GDM method.

In conclusion, the gamma deposition distribution calculated by GDM method with 23x23 subdomains, 17x17 primary domains and leakage-based energy preservation correction mode is very consistent with the reference, with relative errors are <0.5% in most pins. The non-fuel pin correction factor cannot account for the gamma deposition in guide tubes very accurately and thus leads to 2-3% relative errors in some guide tube pins, but 2-3% error is still acceptable and can be improved if a more accurate correction factor is available. There are some pins with high relative errors, but these pins have very low deposition values and the total number of such pins is very small. As a result, the overall gamma power in the SMR core will not be noticeably affected by these errors. As for the speed performance, MPACT tests showed that the GDM method with 23x23 subdomain approach is 2.4x faster than the explicit transport solver on this problem and can be even faster with further optimizations of the GDM method.

# Chapter 7
# Conclusions

## 7.1. Summary of Work

The thesis started with the introduction of how gamma heat deposition in nuclear reactors is calculated conventionally. Unlike charged particles whose kinetic energy is usually assumed to be deposited at fission sites, gamma energy deposition is more complicated due to the relatively long mean free path of gammas compared to charged particles. Although assuming local deposition or applying some simplified gamma smearing models can be reasonably accurate for LWRs because gamma heating only counts for about 10% of the total energy release, explicit gamma transport capabilities have attracted more attention recently because of increasing and less expensive computational capability and interests in modeling advanced reactors. However, explicit gamma transport calculations can be as time-consuming as neutron transport calculations per energy group. Since gammas only accounts for 10% of the total energy released in LWRs, it is desirable to come up with a simpler way to evaluate gamma heat deposition, which is the objective of the gamma deposition matrix (GDM) method.

In Chapter 2 the gamma transport equation and implementation of the explicit gamma transport solver in MPACT are described. Given the fact that the gamma transport equation is similar to the neutron transport equation, many of the procedures developed for neutron calculation, such as the 2D MOC sweeper and 2D/1D solver, can be leveraged to solve gamma transport equations. The source term for the gamma transport equation is the $(n,\gamma)$ source, which is calculated by a standalone procedure. For coupled n-gamma iterations in MPACT, gamma sweeps and neutron sweeps are performed iteratively so that thermal feedback from gamma heating can be integrated into the neutronics calculation. Within

each iteration, the gamma flux is solved after neutron flux is used to compute the $(\mathrm{n},\gamma)$ source. Although the gamma transport calculation capability in MPACT is not used for GDM generation yet, this gamma transport capability was still used for source distribution calculation and verifications for the invariance of gamma source spectra over burnup iterations, which are crucial parts for GDM calculation and memory storage reduction. Chapter 2 also verified that gamma interactions with background media are insensitive to depletion and temperature changes because gamma rays mainly interact with electrons. These conclusions are crucial for GDM simplifications.

Chapter 3 introduced the mechanism of the GDM method. The method is based on defining a gamma deposition matrix *F* that allows the gamma deposition distribution $\vec{D}$ to be computed given the gamma source $\vec{Q}$, or $\vec{D} = F \cdot \vec{Q}$. The source vector $\vec{Q}$ is calculated in MPACT using the $(\mathrm{n},\gamma)$ source procedure and the matrix F is generated using MCNP. The original matrix *F* is of size *N*N*G*G* where *N* is number of pin cells and *G* is number of gamma groups. Although generating the matrix *F* is significantly more expensive than just performing a gamma transport sweep directly, the GDM can be pre-calculated and used over thermal feedback or burnup iterations without recalculation given the insensitivity of gamma energy deposition to depletion and temperature changes. In other words, the *N*G* fixed source runs are only needed to be executed once at the beginning of cycle and can be used for each $(\mathrm{n},\gamma)$ iteration.

Chapter 4 presented the rationale to reduce the GDM size by removing the energy dependence of the GDM. On the deposition side, only the total heat deposition in target cell *i* is necessary. As for the source side, a verification using MPACT showed that the source spectra are relatively invariant over coupled $(\mathrm{n},\gamma)$ iterations even if fuel burnup calculation is turned on. The invariance of source spectra indicates that the matrix does not need to keep an extra dimension of energy bins to accommodate different gamma source spectra. As a result, the matrix can be summed over both source groups and deposition groups and the final form is a N x N matrix F, the total heat deposition in target cell *i* induced by total source intensity in cell *j*. F should be generated using a typical spectrum of gamma source $\vec{\mathrm{Q}}$.

Chapter 5 discussed further simplifications of the gamma deposition matrix. First, deposition in a cell far away from the source would be very small and negligible because of gamma attenuation over a long path. Therefore, each matrix generation run can be done on a "subdomain" surrounding the source cell, instead of the whole problem domain. Vacuum boundary conditions can be used for these subdomains because the probability of gamma returning to the subdomain is small. Next, each subdomain is split into primary domain and secondary domain. The secondary domain consists of pins on the outermost few rings of the subdomain and the primary domain is the inner region. The matrix generation fixed source runs are still performed on the whole subdomain and deposition in each pin in the primary domain is explicitly tallied, while approximations are applied to secondary domain tallies because deposition in pins in this region is relatively low and very high accuracy is not required. Two different approximations were proposed and one of them was selected for its flexibility and ease of development: total deposition in pins on the same side in the same secondary ring are tallied together and evenly redistributed to these pins with Z number-based non-fuel pin correction factors. This approximation can reduce matrix generation time in code systems whose performances are tally dependent like MCNP. Finally, two energy preservation approaches are presented. The first is to put all energy leaking out of the subdomain but still supposed to be inside the core evenly back to all pins outside the subdomain, and the second is to tally the energy leaking out of the subdomain but not an external boundary and put it back into the secondary domain by scaling up the secondary domain deposition. The latter approach has been found to be the preferred method for conserving gamma energy.

The first half of Chapter 6 presented the numerical results of MPACT's explicit gamma transport solver. MPACT's accurate results for the flux spectrum for a pin cell case, the spatial flux distributions for 2D assembly cases, and the axial flux for a mini 3D assembly confirmed that the existing 2D MOC solver and 2D/1D solver were properly implemented. Performance on large cases and the parallelism compatibility of the gamma 2D MOC solver were also qualitatively verified on a 2D quarter core case. MPACT's heat deposition results also showed good agreements with MCNP references, except in low heat pins such

as empty guide tube pins and high gradient axial meshes such as the lower end of a control rod. Note that, as the HELIOS library used by MPACT does not account for photon fluorescence effect, MCNP reference calculations for comparison with MPACT results were generated with photon fluorescence off.

The second half of Chapter 6 presented the numerical results using the GDM method. The verification started with a 29x29 vacuum boundary assembly. The full sized GDM method provided excellent accuracy with negligible, randomly distributed uncertainties. It was found that the GDM method with the subdomain + secondary domain simplification worked very well, but needed to have a model to preserve energy that escaped the subdomain and would have been deposited in the core. A leakage-based energy preservation, combined with the subdomain with secondary domain model, was proven to be reliable because it successfully balanced accuracy and simplicity. The maximum errors not only met the accuracy goal, but only appeared in a few low power corner pins. The full sized GDM method was shown to be highly accurate for 3D mini assembly calculations as well. Finally, the GDM method with subdomain + secondary domain + leakage-based energy preservation model was used to calculate heat deposition in a small modular reactor core. Overall, the relative errors are <0.5% in most pins, which are well below the error acceptance standard. Errors in guide tube pins are slightly higher but the errors are considered reasonable. Compared to the full sized GDM, using the subdomain approach reduced the GDM size by a factor of ~20 for this SMR case. As for the speed performance, the GDM method with the subdomain approach is most beneficial for large cases and cases where a lot of iterations are required. According to speed tests in MPACT, for the SMR case with 25 statepoints and 20 iterations per statepoint, the GDM method with 23x23 subdomain would be 2.4x faster than the explicit gamma transport solver.

## 7.2. Suggested Future Work

A key task for future work would be to implement the GDM method into MPACT. Currently the source intensity vector is calculated using MPACT, the GDM matrix is generated by MCNP and the $\vec{D} = F \cdot \vec{Q}$ calculation is performed using a standalone script.

Although the feasibility of the GDM method is proved, the method is far from being a production capability. If it can be implemented into MPACT as an option to solve for gamma heating, the usability would be significantly improved. Furthermore, the GDM matrix multiplication step (negligible CPU time) can be integrated into the coupled $(n,\gamma)$ iterations, thus accounting for TH feedback and meeting the original purpose of this research project to take advantage of the insensitivity of gamma energy deposition to thermal feedback and burnup effects.

The GDM method has only been applied to vacuum boundary problems so far. Although theoretically a reflective boundary could be unfolded and then modeled just like the inner region of the problem, such approach would be very inefficient. In practice, reflective boundaries are not uncommon such as reflective boundary assemblies and quarterly symmetric problems, so built-in boundary capabilities should be developed for the GDM method.

Finally, inspired by how the treecode method treats Green's functions [32], it may be possible to use this method with GDM. To avoid calculating each point-to-point Green's function explicitly, the treecode method combines points on the source side first and then calculates one single cluster-to-point Green's function. Since the Green's function for gamma deposition involves a multipath gamma transport calculation for each source point, it isn't clear how this would be implemented, but the potential savings in computational time is incentive to investigate this approach.

# Bibliography


[1] American Nuclear Society, "ANSI/ANS-19.3.4-2002, the determination of thermal energy deposition rates in nuclear reactors," American Nuclear Society, La Grange Park, Illinois.

[2] A. Godfrey, "VERA Core Physics Benchmark Progression Problem Specifications," 2014.

[3] X. Wang, Y. Liu and W. Martin, "Energy Deposition Analysis for VERA Progression Problems by MCNP," in *PHYSOR*, Cancun, Mexico, 2018.

[4] E. Larsen, B. Collins, B. Kochunas and S. Stimpson, "MPACT Theory Manual".

[5] K.-S. Kim, S. G. Hong, J. Y. Cho and J. S. Song, "Transport Lattice Code KARMA 1.1," in *Korean Nuclear Society Autumn Meeting*, Gyeongju, Korea, 2009.

[6] K. S. Kim, K. T. Clarno, B. S. Collins, Y. Liu, X. Wang and W. Martin, "Neutron Capture Energies for Flux Normalization and Approximate Model for Gamma-Smeared Power, CASL-U-2017-1377-000, ORNL/SPR-2017/471," Oak Ridge National Laboratory, Oak Ridge, TN, 2017.

[7] Y. Liu, R. Salko, K. Kim, X. Wang, B. Kochunas, B. Collins and W. Martin, Improved MPACT Energy Deposition Model and Explicit Heat Generation Coupling with CTF, Annals of Nuclear Energy, 2020.

[8] K.-S. Kim and S. G. Hong, "Gamma transport and diffusion calculation capability coupled with neutron transport simulation in KARMA 1.2," *Annals of Nuclear Energy*, vol. 57, pp. 59-67, 2013.

[9] Studsvik Scandpower, Inc. (SSP), "CASMO5 Methods and Validation Report".

[10] Y. S. Jung, C. B. Shim, C. H. Lim and H. G. Joo, "Practical numerical reactor employing direct whole core neutron transport and subchannel thermal/hydraulic solvers," *Annals of Nuclear Energy*, vol. 62, pp. 357-374, 2013.

[11] N. Choi, H. Park, H. G. Lee, S. Jae, S. Jeon and H. G. Joo, "Recent Capability and Performance Enhancements of the Whole-core Transport Code nTRACER," in *PHYSOR*, Cambridge, UK, 2020.

[12] Y. S. Jung, C. Lee and M. Smith, "PROTEUS-MOC User Manual".

[13] Nuclear Science and Engineering Division, Argonne National Laboratory, "Updates and Verifications of the PROTEUS Suite in FY19," 2019.

[14] J. Leppänen, T. Kaltiaisenaho, V. Valtavirta and M. Metsälä, "Development of a Coupled Neutron / Photon Transport Mode in the Serpent 2 Monte Carlo Code," in *M&C*, Jeju, Korea, 2017.

[15] R. Tuominen, V. Valtavirta and J. Leppänen, "New energy deposition treatment in the Serpent 2 Monte Carlo transportcode," *Annals of Nuclear Energy,* vol. 129, pp. 224-232, 2019.

[16] R. Forster and T. Godfrey, "MCNP - a general Monte Carlo code for neutron and photon transport," in *Monte-Carlo Methods and Applications in Neutronics, Photonics and Statistical Physics*, 1985, pp. 33-55.

[17] Monte Carlo Methods, Codes, & Applications Group, "A General Monte Carlo N-Particle (MCNP) Transport Code," Los Alamos National Laboratory, [Online]. Available: https://mcnp.lanl.gov/.

[18] S. Stimpson, T. Downar, B. Collins, E. Larsen, W. Martin and D. Viswanath, "An Azimuthal, Fourier Moment-Based Axial SN Solver for the 2D/1D Scheme, Chapter 2".

[19] X. Wang, Y. Liu, W. Martin and S. Stimpson, "Implementation of Gamma Transport Capability in MPACT," in *M&C*, Portland, Oregon, 2019.

[20] X. Wang, Y. Liu, W. Martin and S. Stimpson, "Implementation of 2D/1D Gamma Transport and Gamma Heating Capability in MPACT," in *(Conference cancelled)PHYSOR*, Cambridge, UK, 2020.

[21] Studsvik Scandpower, "HELIOS: THE LIBRARY," 2008.

[22] B. Kochunas, T. Downar, E. Larsen, W. Martin, S. Palmtag and Q. Stout, "A Hybrid Parallel Algorithm for the 3-D Method of Characteristics Solution of the Boltzmann Transport Equation on High Performance Compute Clusters," 2013.

[23] B. Collins, S. Stimpson, B. Kelley, M. Young, B. Kochunas, A. Graham, E. Larsen, T. Downar and A. Godfrey, "Stability and accuracy of 3D neutron transport simulations using the 2D/1D method in MPACT," *Journal of Computational Physics,* vol. 326, pp. 612-628, 2016.

[24] A. LUTHI, "Development and Validation of Gamma-heating Calculational Methods for Plutonium-burning Fast Reactors," ECOLE POLYTECHNIQUE FEDERALE DE LAU- SANNE, 1998.

[25] G. Knoll, Radiation Detection and Measurement, New York City, USA: John Wiley & Sons. Inc., 2000.

[26] X-5 Monte Carlo Team, "MCNP — A General Monte Carlo N-Particle Transport Code, Version 5, Volume I: Overview and Theory," 2003.

[27] Y. Liu, W. Martin and T. Downar, "Delayed Fission Energy Effect on LWR Normal Operation and Transients," *Annals of Nuclear Energy,* vol. 128, pp. 84-93, 2018.

[28] P. T. So, "Two-photon Fluorescence Light Microscopy," Cambridge, Massachusetts, 2001.

[29] Lawrence Berkeley National Laboratory, "X-RAY DATA BOOKLET, Section 1.1," 2009.

[30] K. S. Kim, K. Clarno, C. Gentry, D. Wiarda, M. Williams, B. Kochunas, Y. Liu and S. Palmtag, "Development of the V4.2m5 and V5.0m0 Multigroup Cross Section Libraries for MPACT for PWR and BWR, CASL-U-2017-1280-000".

[31] A. dos Santos, G. S. Andrade e Silva, L. F. Mura, R. Fuga, R. Jerez and A. G. Mendonça.

[32] P. Li, H. Johnston and R. Krasny, "A Cartesian treecode for screened coulomb interactions," *Journal of Computational Physics*, 2009.